Gathering and Handling of Granular Materials under Microgravity Conditions
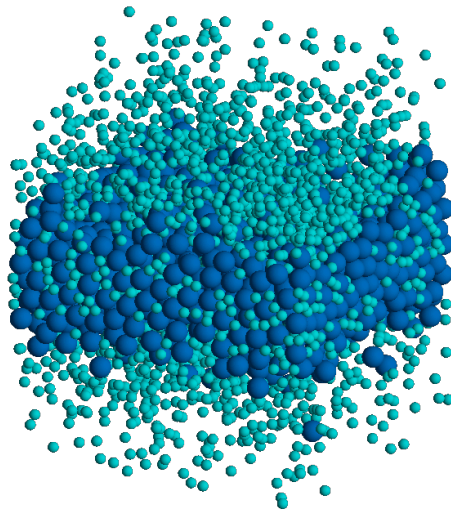
Dissertation présentée par
Eric Opsomer
en vue de l'obtention du grade de Docteur en Sciences.
Année académique 2014-2015.

Abstract

When a granular material is driven in microgravity environment, one can assist to the formation of dense and slow regions in the system. Indeed, given the dissipative character of the collisions in the media, energy is lost at each particle interaction and the grains begin to clump locally. The phenomenon has been observed for the first time in the late nineties during sounding rocket experimentation by Falcon and his coworkers and has attracted the interest of many scientists since then. However, precise laws describing the formation and the dynamics of such clusters are still lacking. In order to allow an intensive study of the phenomenon, the European Space Agency set up the SpaceGrains project. Small bronze spheres are enclosed in a rectangular cell and vertically driven by to pistons oscillating in phase opposition. Our work consists in the preparation of the SpaceGrains experiment via molecular dynamics simulations and the elaboration of models predicting the behaviour of the system.

Before we started our study concerning SpaceGrains, we reproduced and extended Falcon's sounding rocket experiments. We showed that, in addition to the granular gas and the cluster, another dynamical regime can be observed in the system. Indeed, for higher filling fractions, the entire granular media behaves like one single completely dissipative particle called the bouncing aggregate. Bouncing modes are observed and can be explained considering the bouncing ball paradigm. Moreover, we highlighted the role of the packing fraction ϕ as well as the size of the particles R on the different observed dynamics.

Within the frame of the SpaceGrains device, we studied the impact of all tunable parameters of the experiment on the dynamics of the system. Thanks to an appropriate scaling all transition points that we obtained by varying the driving amplitude A, the packing fraction and the dimensions of the cell L fall along a same theoretical curve. The latter is explained regarding the energy transfer from the piston towards the center of the cell.

Once the clustering was controlled, we investigated the handling of the agglomerate. By compartmentalizing the container, local trapping can be achieved and a granular pendant of Maxwell's demon can be observed in microgravity. Based on the measured particle flux between the compartments, we realized a theoretical model predicting the asymptotic steady state of the system depending on the total number N of particles.

In a clustered system, we investigated the impact of asymmetrical driving on the system's dynamics. We showed that the mean position of the cluster can be fully controlled via the amplitude ratio a. Moreover, the natural fluctuations of the agglomerate around its equilibrium position are dictated by the driving frequency f and the mass of the cluster.

Finally, we realized simulations of driven bi-disperse gases and investigated the segregation phenomena in the system. We showed that clustering and segregation are strongly linked and that the size and the mass of the particles impact the segregation dynamics in different ways.

5

Preamble

The following manuscript consists in a collection of scientific articles realized during the period of my PhD thesis. A general introduction to the physics of granular materials and a description of my personal contribution to the gathering and handling of granular materials in microgravity are given in the first part of the document. The state of the art is then completed by an overview of the numerical tools used to simulate granular media. In the two main parts of the manuscript, we present five articles capturing the work of these last four years. In the corresponding chapters, the motivations for each study and their main results are briefly discussed. Moreover, a copy of the original paper is added at the end of the chapter. Finally, the conclusion and perspectives of our work can be found at the end of the manuscript.

List of publications

- *Phase Transitions in Vibrated Granular Systems in Microgravity*: E. Opsomer, F. Ludewig and N. Vandewalle, Phys. Rev. E. **84**, 051306 (2011).

- *Dynamical Regimes of a Granular Gas in Microgravity: a Molecular Dynamics Study*: E. Opsomer, F. Ludewig and N. Vandewalle, Journal of Phys: Conf. Ser. **327**, 012035 (2011).

- *Dynamical clustering in Driven Granular Gas*: E. Opsomer, F. Ludewig and N. Vandewalle, Eur. Phys. Lett. **99**, 40001 (2012).

- *How Dynamical Clustering Triggers Maxwell's Demon in Microgravity*: E. Opsomer, M. Noirhomme, N. Vandewalle and F. Ludewig, Phys. Rev. E. **88**, 012202 (2013).

- *Clustering and Segregation in Driven Granular Fluids*: E. Opsomer, N. Vandewalle, M. Noirhomme and F. Ludewig, Eur. Phys. J. E., accepted (2014).

- *Granular Transport in Driven Granular Gas*: M. Noirhomme, E. Opsomer, N. Vandewalle and F. Ludewig, Eur. Phys. J. E., submitted (2014).

- *Two Dimensional Circularly Rotating Drum*: F. Ludewig, E. Opsomer, J De La Cruz Damas, G. Lumay, H. Caps and N. Vandewalle, Gran. Matt., submitted (2014).

- *Compaction Dynamics in a Pile of Prolate Particles*: F. Ludewig, E. Opsomer and N. Vandewalle, in preparation.

- *Compaction Like Dynamics and Maxwell's Demon*: E. Opsomer, F. Ludewig, N. Ndorere and N. Vandewalle, in preparation.

Contents

Part I

Introduction

Chapter 1

State of the art

From the sugar that we pour in our coffee to the gravel placed along our railroads, granular materials are present everywhere. Accordingly, it is not astonishing that, nowadays, over eighty percent of the materials used in industrial processes are granulates. Numerous sectors of activity are concerned (construction, agri-food, mining, pharmaceutics...) but despite an intensive use, most of the atypical behaviours presented by granular materials could still not be rationalized. A better comprehension of the media would have a great impact from an industrial perspective as well as from a scientific point of view. Before we start to investigate the interactions that lead to the gathering and the handling of driven granular media in microgravity, it seems essential to give a general introduction to the granular materials and their rich variety of properties.

1.1 Granular materials

Granular materials can be defined as complex materials composed by solid grains within a surrounding fluid. This definition covers a large amount of very different materials and products that we encounter everyday [1,2]. Medication and other drugs, which are nothing else than compressed powders, crops and corn that are stored in silos and even icebergs in our oceans are only a few examples. All those materials differ not only in size but also in the interactions between their composing grains and the following distinction can be made: large particles with a typical size above 50 μm are only affected by gravitational and contact forces. Smaller particles are also influenced by electrical charges in the media, the relative humidity and Van der Waals forces. This second category is qualified as cohesive granular materials. However, Vandewalle *et al.* showed recently that the relative humidity can also influence milimetric particles [3]. Figure 1.1 describes different granular materials. The size of the composing particles grows from left to right: regolith on the Moon's surface, colored powders on an indian market, a mixture of crops and icebergs at cape York, Greenland.

Figure 1.1: Different granular materials classed by growing grain sizes. (From left to right) regolith on the Moon's surface, colored powders on an indian market, a mixture of crops and icebergs at cape York, Greenland.

In the rest of this work we will focus only on large particles so that cohesive forces will not play any role in the observed phenomena. Nevertheless, the behaviors of granular materials are as various as astonishing [4, 5] and their macroscopic dynamics vary strongly with the external stresses that are applied to them. Indeed, by controlling the energy that is injected into a granular media several dynamical regimes can be observed. They are described thereafter.

1.2   Solid regime

Depending on the external stresses that are applied to them, granular materials can be found in different dynamical regimes. For example, when a truck pours a large amount of gravels on a construction site, a heap is obtained. During the unloading, one can notice that while some gravels are at rest on the bottom of the pile, others slide down along its edges. Once all the particles are at rest, the heap has a specific angle θ_r, called the angle of repose [6]. This angle depends on the nature and the shape of the particles and can be seen on the left side of figure 1.2. This static pile of gravel could naively be compared to a solid. Indeed, contacts between the composing grains are permanent and there are no relative displacements within the media. However, despite this resemblances, a counter example is easily found: when pressure is exerted on a real solid its volume decreases, while the volume of a dense granular solid increases. This phenomenon is called Reynold's dilatancy [7, 8] and can be encountered while walking on wet sand along the sea. When your foot steps on the sand, the volume of the pores between the grains increases and the surrounding water is absorbed which results in a dry zone around your foot.

Figure 1.2: (Left) A heap of gravel can naively be compared to a granular solid. While pouring, a particular angle of respose is obtained. (Right) The pressure of the foot on the sand creates a dry zone by absorbing the water into the pores between the grains.

Another feature of granular solids is the repartition of external forces that are applied to them. If one places a scales at the bottom of a vertical cylinder and starts pouring granular material onto it, the displayed weight will not increase linearly. Rapidly, some saturation occurs and eventually the measured weight of the pile remains constant even though the poured mass increases. This effect was discovered in 1895 by Janssen [9] and can be explained by the formation of microstructures within the pile. Multiple granular arches deviate the applied vertical stresses towards the side wall of the cylinder. The formation of such arches can be linked to the friction between the particles themselves and between the particles and the boundaries of the system. Based on hydrostatic criteria and on the hypothesis that each vertical constraint p_v generates a proportional and smaller horizontal constraint $p_h = Kp_v$, Janssen proposed the following model. He considered a slice of width dh at a given depth h in a cylinder of section A and perimeter P. A schematic view is given in figure 1.3. In order to maintain its vertical position several forces act on the slice. One of them is its weight $Adh\rho g$, where ρ is the density of the medium. Moreover, since the pressure in the system increases with the depth, a force Adp_v is vertically exerted on the slice. Finally, a friction force exists on the lateral surface Pdh of the cylinder and is given by $\mu_s p_h Pdh$, where μ_s is the static friction coefficient. Given Janssen's hypothesis, the equilibrium condition can now be written, *i.e.*
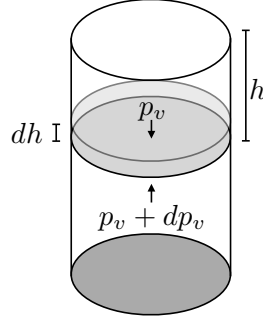
Figure 1.3: Vertical constraints that are applied to a slice of width dh of granular material in the cylinder at depth h.

$$Adp_v + K\mu_s p_v P dh = \rho g A dh, \qquad (1.1)$$

with $K < 1$ being a constant. Dividing through by dh yields in the following differential equation

$$\frac{dp_v}{dh} + \left(K\mu_s \frac{P}{A}\right) p_v = \rho g. \qquad (1.2)$$

Considering as initial condition that for $h = 0$ the pressure $p_v = 0$, the solution of the latter equation is given by

$$p_v = \rho g \frac{A}{PK\mu_s} \left[1 - \exp\left(-K\mu_s \frac{P}{A} h\right)\right]. \qquad (1.3)$$

For small values of h, one notes that $p_v \approx \rho g h$, reminding the hydrostatic pressure in a liquid. Once h becomes larger than $\lambda = A/(PK\mu_s)$, the vertical pressure saturates towards its maximum value of $\rho g \lambda$ which is in total agreement with the saturation of the weighted mass in the initial experiment.

An important industrial implication of this effect can be found on our railroads as shown in the right part of figure 1.4. Indeed, a granular material called ballast is placed under the rails in order to prevent their sinking into the ground.

Figure 1.4: (Left) Picture obtained by exerting pressure on stress birefringent particles. The highlighted zone correspond to the force network through the granular media. (Right) Ballast used to prevent rails from sinking into the ground.

The arch formation and the spatial inhomogeneous stress distributions are major characteristics of granular media. The force network that spreads across the system can be visualized using stress birefringent particles [10–15] as shown in the left part of figure 1.4 but a quantitative measurement of the forces inside the three dimensional stack is difficult to obtain with this method. It is however possible to measure the forces exerted on the boundaries of the container. Liu *et al.* showed in their

experiments [16] that the spatial probability distribution for finding a normal force of intensity F against a wall decays exponentially for forces larger than the mean $\bar{F}$. Mueth *et al.* extended this result [17] and proposed a nearly uniform distribution for the forces below the mean value. The measures were made thanks to a carbon paper method [18, 19]. The side wall of the cylinder and the surface of the pistons are covered with a thin layer of carbon paper above which classical copier paper is placed. The pressure that each particle exerts on the boundaries creates more or less dark spots on the copier sheet. These imprints are then digitalized, in order to treat more efficiently the data and to obtain the distribution of the forces. Figure 1.5 presents a photography of one of the imprinted sheets of paper from Mueth's experience as well as the obtained distributions. Recently, these grain-wall contact forces could be measured more precisely by using wavelength
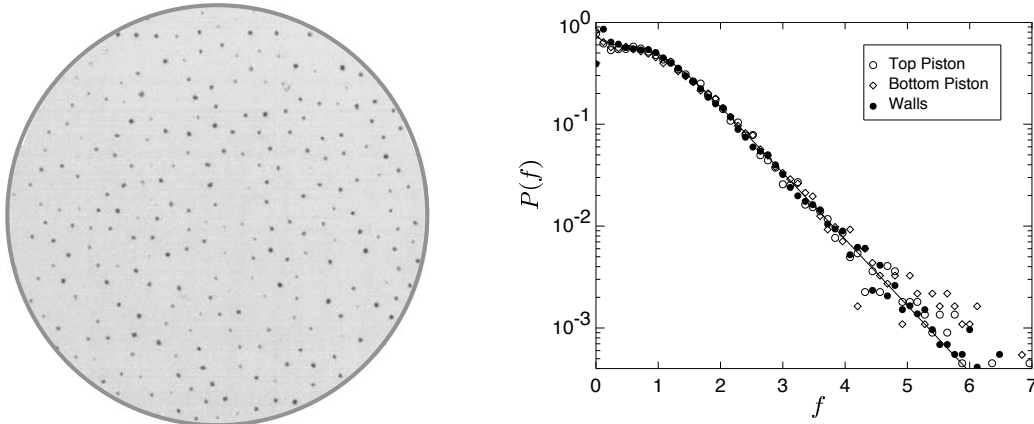
Figure 1.5: (Left) Carbon imprints on a the bottom piston: the side wall of the cylinder as well as the surface of the pistons are covered with a thin layer of carbon paper above witch classical copier paper is placed. The stronger the pressure exerted by the grains against the walls, the darker the obtained dots. (Right) Graphic describing the distribution of the normalized forces $f = F/\bar{F}$. Photography and plot taken from [17].

scanning interferometry [20] and similar distribution are obtained.

1.3   Liquid regime

Let us now go back to our heap of gravel and imagine that we take away particles from the bottom of the pile until the static equilibrium becomes unstable. The pile crumbles and an avalanche occurs. On the surface, the gravels flow towards the ground, as a liquid would do. On the contrary, the gravels on the bottom, remain in a solid state. In this case we have a coexistence of a granular liquid and a granular solid. However, various phenomena show once again that the analogy with a classical fluid is not appropriate and one should rather qualify them as complex fluids [21–23].

Understanding the rheology of these kind of materials is of great industrial interest. In various processes, grains have to be pumped from one step of fabrication to the next and problems like the arch blocking of the flow or the thickening of the fluid have to be avoided. Moreover, granular pastes as concrete are still in the center of applied studies that aim higher resistance and performance for our constructions.

In order to maintain the granular material in its liquid form, external constraints are required. One simple way to observe a continuous flow is to enclose the material in a drum and to rotate it at a certain rotation speed Ω. For small speeds ($\Omega < 0.1$ rpm), an intermittent flow is observed. Initially, the free surface of the granular media forms an angle θ with the horizontal. This angle increases slowly up to an angle θ_m called the angle of movement. At this point the grains slide down and the angle of repose θ_r is obtained. This cycle goes on and the system oscillates between

Figure 1.6: Understanding the rheology of these complex fluids is of great industrial interest. In various processes grains have to be pumped from one step of fabrication to the next. Granular liquids are also observable in nature and may have dramatic consequences as landslides and avalanches.

both angles. For higher speeds ($\Omega \approx 5$ rpm), the flow becomes continuous and the free surface bends to take an S-shape as one expects for a liquid [24]. Figure 1.7 presents both behaviors encountered in rotating drums. If one tries to find the limit speed between both regimes, an

$\Omega < 0.1$ rpm $\qquad\qquad \Omega \approx 5$ rpm
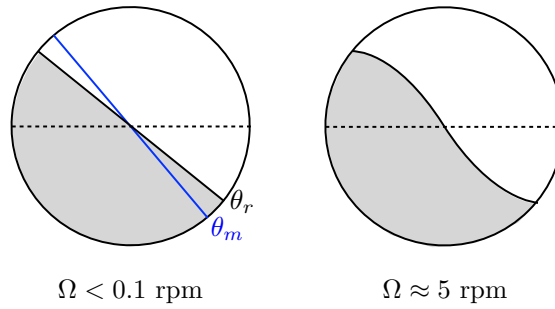
Figure 1.7: Behavior of rotated granular material for different rotation speed. For small Ω (left), an intermitend flow is observed, for higher speeds (right), the flow is continuous and the free surface takes the appearance of an S-shaped curve.

interesting phenomenon appears. Indeed, starting from the intermittent state, we increase Ω until a certain value $\Omega_\uparrow$ for which the flow becomes continuous. If we now decrease the speed, a transition occurs for a value $\Omega_\downarrow < \Omega_\uparrow$. This hysteresis is a particular feature of granular materials and is not encountered for classical Newtonian liquids.

Another way to keep a granular material in the liquid regime is to oscillate it. Indeed, if a system with a large number of particles is vertically oscillated wave structures can appear at its surface. Moreover, due to the interaction with the energy injecting boundaries and the friction at the walls of the system, convective motion can be observed [25]. For a classical liquid, convection occurs when the heated particles rise up in the system while the cold ones sink, creating a rotational motion of the fluid in the tank. In a granular system, it is the vertical shaking that creates an upward movement of the particles. During the upward phase, the entire pile takes off but the external grains, that are in contact with the side walls, are slowed down due to friction forces. In addition, once the container moves downwards, a vertical shear stress forces this outer layer of grains down to the ground much faster than the rest of the pile. Consequently, a convective motion takes place in the system. For large systems, several convection cells can appear and interact with each other [26]. Recent experiments [27] in slowly rotated Hele-Shaw cells present similar behaviours. Figure 1.8 confronts the usual convection of liquids with the granular convention rolls described by Eshuis *et al.*

Heat   Shaking
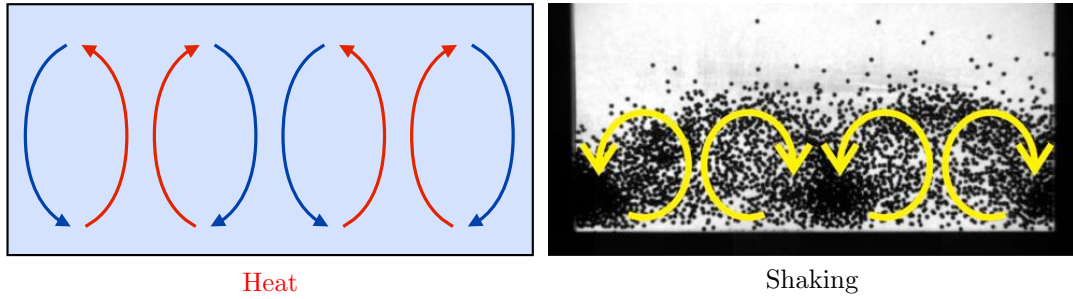
Figure 1.8: (Taken from [26]) Analogy between the convective motion of a classical liquid under heating constraints (left) and a driven layer of granular materials (right).

Liquid like behaviors can also be encountered in 2d systems. For instance, shaking a granular monolayer along a vertical axis z reveals a rich variety of behaviors [28, 29]. The small defects of the cell's walls and the interaction with neighboring particles transform the purely vertical velocities into a Brownian motion in the xy plane. Depending on the filling fraction of the system and the intensity of the shaking divers dynamical regimes are encountered. Fluid like motion, formation of wave patterns and crystallization are only a few examples. In a recent article [30], Merminod et $al.$ showed that when additional repulsive forces are added to the particle interaction, the typical properties of dissipative granular fluids are lost and tend to those expected for a classical fluid (quasi-Gaussian velocity distributions and nearly flat pair correlation functions). In their experiment, a vertical magnetic field B_0 is applied to the system creating a dipole-dipole interaction between the grains. Figure 1.9 describes the observed dynamics for an increasing field amplitude. Note that a hexagonal crystal is obtained for high B_0.

increasing B_0
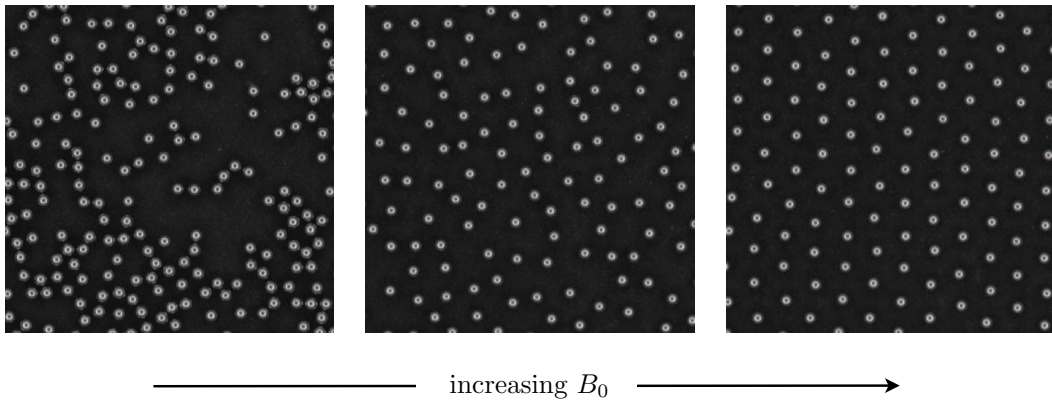
Figure 1.9: Snapshots of Merminod's et $al.$ experience [30]. The magnetic field B_0 increases from left to right. For low field values, one observes a granular fluid. At high values of B_0, the system orders into a hexagonal crystal. In the intermediate range, the system approaches the dynamics of a classical molecular fluid.

1.4   Gaseous regime

When a large amount of energy is injected continuously into a confined and dilute granular medium, the particles stir up and behave like a gas [31–34]. In nature, this phenomenon can be encountered when a tornado crosses a desert region and forms a Dust Devil or, at a larger scale, in Saturn's rings (see figure 1.10). In the laboratory, a granular gas can be obtained by an intense driving of the system. For instance, Falcon et $al.$ enclosed several stainless steel beads in a cylinder and vibrated

them vertically [35]. Their simple experimental setup, generates a model of the dynamics of a granular gas. It is important to note that the formation of a granular gas does not only depend on the injected energy but also on the packing fraction of the system. Indeed, increasing the number of particles N in the system can lead to a transition from an erratic motion to a collective behavior where all the particles bounce like a nearly solid body. Snapshots of the experiment for respectively 480 and 1920 grains for constant driving conditions are given in figure 1.11.

Figure 1.10: Granular gases in nature, a dust devil in the ethiopian desert (left) and the rings of Saturn (right, photography by the National Aeronautics and Space Administration).

In order to push a bit further our analogy and to grant a homogenous, gas like, distribution of the particles, a granular gas has to be created in microgravity. This can be achieved by various means. Parabolic flights (see right part of figure 1.11) or drop tower experiments might be the most affordable ways but don't assure a stable level of microgravity. Indeed, gravitational fluctuations known as g-jitter are unavoidable. Moreover, the period of microgravity is relatively short. At higher cost, sounding rockets (Mini-Texus, Texus, Maxus, ...) or even the International Space Station (ISS) provide a much more stable g-level and a longer duration of the microgravity conditions. However, given the complexity and the costs of these experiments, granular gases are often studied via numerical simulations.
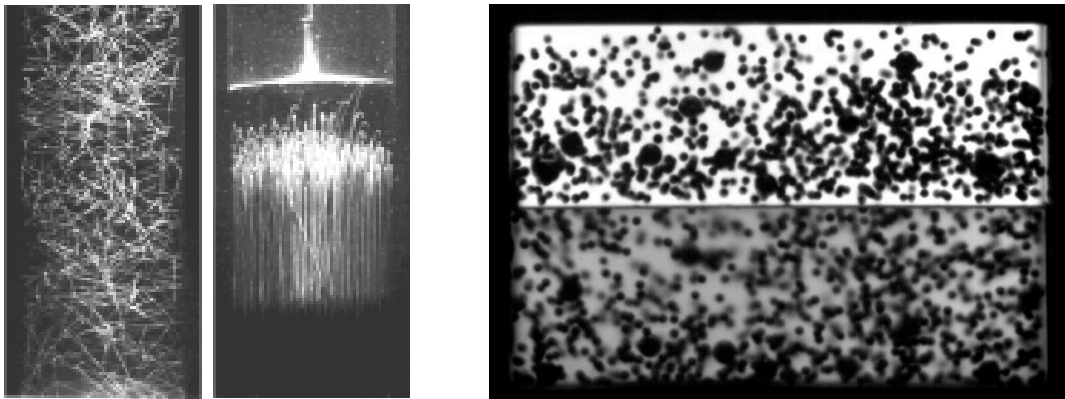
Figure 1.11: (Left, taken from [35]) Driven granular gas under gravity, depending on the filling, a transition to a solid like regime is noted. (Right, photography by F. Palencia) Granular gas during a parabolic flight experiment.

Unlike a molecular fluid, our system is athermal which implies that the average kinematic energy of a granular gas is not determined by the surrounding temperature. However, in order to approach these materials from a thermodynamical point of view different granular temperatures

T have been proposed. One simple method to define this temperature in a mono disperse system is to use the kinetic energy of a particle of mass m moving with the average speed $\langle v \rangle$,

$$T = \frac{1}{2} m \langle v \rangle^2 \tag{1.4}$$

Accordingly, the speed distribution of the particles in a granular gas doesn't follow a Maxwell-Boltzmann (MB) law. In the nineties, theoretical works and simulations [36–38] proposed divers distributions as Gaussians, exponentials and power laws. Experimentally, Olafsen and Urbach [39] found velocity distributions that varied between exponential and Gaussian for an increasing acceleration. Kudrolli and Henry [40] found an even larger spectrum of distributions. However, an universal law recovering all the described dynamics is proposed by Rouyer and Menon [41]. Far away from the boundary conditions, the distributions of all three components of the velocity are similar and follow

$$P(v_i) = C \exp \left[-\beta (|v_i|/\sigma)^\alpha \right], \quad i \in \{x, y, z\}; \tag{1.5}$$

where $\alpha \sim 3/2$ and $\sigma = \sqrt{\langle v_i^2 \rangle}$. The constants C and β are free parameters. This non-Gaussian behavior has been reported in all kind of experimental setups. Neither the cell's geometry nor the shape of the particles seem to have en impact on the measured velocities. A recent example is given by Harth *et al.* who observe the same kind of distribution in a drop tower experiment [42] with driven cylindrical rods.
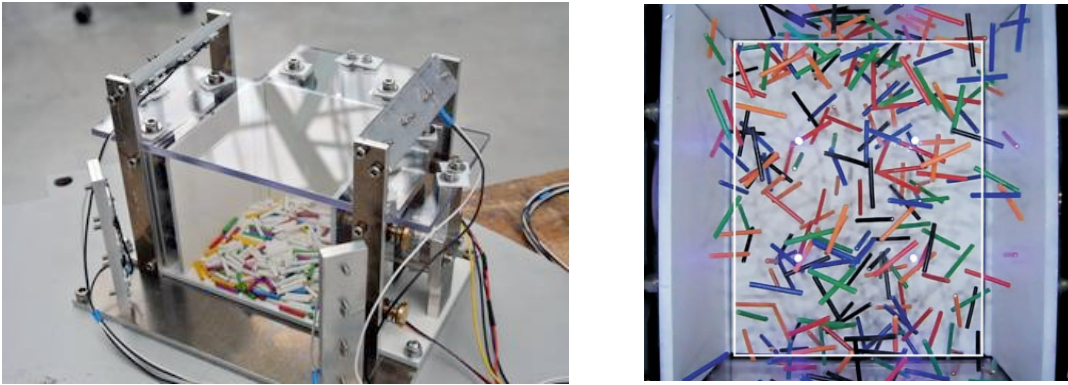
Figure 1.12: (Left) Photo of the cell used for the GaGa drop tower experiment by Harth *et al.* [42]. (Right) Snapshot taken while the rods are driven in microgravity. Non-Gaussian velocity distributions are observed as well for the translations as for the rotations of the particles.

It is important to note that a part of the energy that is injected into a granular gas is dissipated through the great number of collisions between the grains that compose the material. The received kinematic energy is transformed into sound, heat and leads to small deformations of the grains. This dissipative character is an essential feature of a granular material which can be captured by the coefficient of restitution ε. This value corresponds to the ratio of a particle's speed before and after collision and depends mainly on the nature of the material but also on the impact velocity.

1.5   Pattern formation

The dissipative character of the collisions between the particles of a granular gas has an important consequence: a steady state can only be obtained when the injected energy counterbalances exactly the dissipated one. Moreover, this implies a constant and perpetual energy injection into the system. If one stops the energy supply, a cooling mechanism begins and at each collision the velocities of the grains decrease. Rapidly, dense and slow regions appear [43–46] and the time between two successive collisions drops dramatically until the contacts between the grains become permanent. In this case we speak about the inelastic collapse. Figure 1.13 describes the evolution

of such a free cooling granular gas. Maaß *et al.* used diamagnetic granular material that could be levitated in order to reproduce microgravity conditions. After being stirred up mechanically, the evolution of the system is tracked and three snapshots are presented.
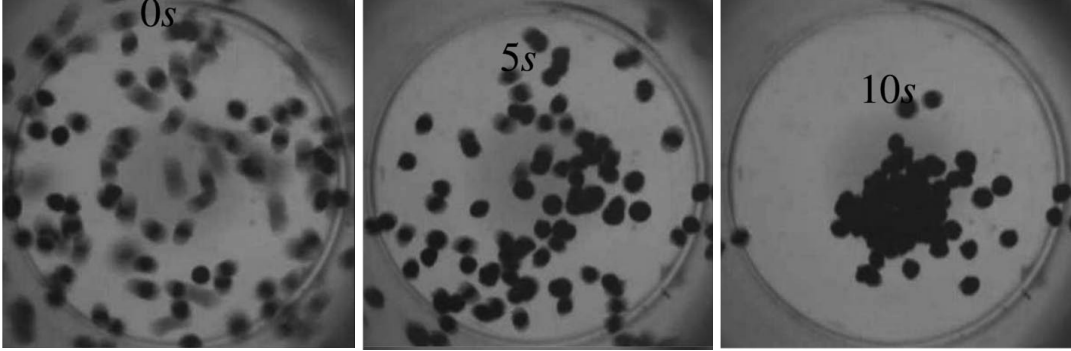
Figure 1.13: Experimental cooling of a three dimensional granular gas by Maaß *et al.* [46]. Particles are levitated magnetically and cool down during 10 seconds. Snapshots are taken at 5 seconds intervals and present pattern formation.

The free cooling mechanism of granular materials and the temporal evolution of the granular temperature T in this kind of systems have been studied intensively by Haff [47]. The model considers N spherical particles of cross section σ, moving with an initial mean velocity v_0, in a closed system of volume V. During the cooling process, the inelastic collisions lead to a continuous energy decay that is captured by the following law,

$$\frac{d}{dt}T = -\frac{(1-\varepsilon^2)}{\tau}T. \tag{1.6}$$

The time τ between two successive collisions is given by $\ell/\langle v \rangle$ where $\langle v \rangle$ is the mean speed in the system and ℓ the mean free path between two impacts. In the dilute limit, the latter can be estimated via the relation $\ell = 1/(\eta\sigma)$, where $\eta = N/V$ is the number density of the system. Since $T \propto \langle v \rangle^2$, equation (1.6) can be reformulated into

$$\frac{d\langle v \rangle}{dt} = -\frac{(1-\varepsilon^2)\eta\sigma}{2}\langle v \rangle^2 \tag{1.7}$$

Solving this differential equation, with the initial condition $\langle v(0) \rangle = v_0$, yields in Haff's law in its original form,

$$\langle v(t) \rangle = \frac{v_0}{1 + t/\tau_H}; \quad \tau_H = \frac{2}{v_0(1-\varepsilon^2)\eta\sigma}, \tag{1.8}$$

where the typical time scale τ_H characterizes the cooling intensity. This hyperbolical evolution of the mean speed has been verified several time as well experimentally [48] as numerically [49]. However, for long cooling times, the uniformity of the spatial distribution of the particles does not hold on. Accordingly, a constant η can no longer be used. Considering a time-dependent number density $\eta(t) = \eta f(t)$, Haff's law can be adapted,

$$\langle v(t) \rangle = \frac{v_0}{1 + 1/\tau_H \int_0^t f(t)dt}. \tag{1.9}$$

Finally, once the quasi totality of the grains contribute to the central agglomerate, the system presents again a classical Haff cooling. Indeed, the cluster can be seen as one big particle with a mean free path of the order of the container size. In this case, energy is only lost during collisions with the walls. By combining the three models, the complete evolution of the mean speed can be captured. Figure 1.14, taken from [46], describes this evolution for two different types of driving.
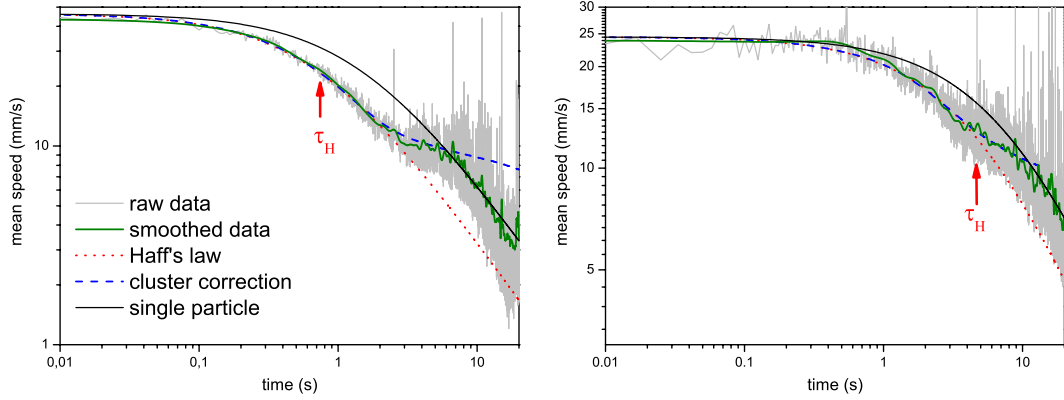
Figure 1.14: (Taken from [46]) Evolution of the mean speed $\langle v(t) \rangle$ for mechanical (left) and magnetical driving (right). Thanks to the three models, the entire evolution can be captured. The red arrow indicates the Haff time τ_H at which $\langle v(t) \rangle$ reaches the half of its initial value.

Cooling phenomena appear in granular media as soon as there is no more external energy supply. However, even when a granular material is continuously driven, a significant fraction of its composing particles might be unaffected by the energy injection, especially if the latter occurs only near the borders. This means that patterns might also form within a hot granular gas [50, 51]. Pioneer works concerning the apparition of such a dynamical cluster of grains have been realized by Falcon *et al.* in the late nineties [52, 53]. Their experiment consisted in three cubic cells filled with different amounts of bronze spheres. The whole setup was then oscillated under microgravity condition in a Mini-Texus sounding rocket. Depending on the filling fraction of the system, clustering could be observed. For the two highest fillings, a dense aggregate of grains was located in the center of the cell. This cold region of low energy is however surrounded by a hot granular gas that transmits the incoming impulse from the borders of the system. The dynamical aspect of this kind of pattern is important. Indeed, the formation of observed cluster is the result of a complex equilibrium between the injected and the dissipated energy. Accordingly, the continuous oscillation of the system is needed in order to maintain the system in its bi-phasic state. If the driving is suddenly stopped the cluster evaporates into the gaseous phase and a cooling process begins. One assists to a transition from a *dynamical* cluster to a *cooled* cluster.

1.6   Segregation

In a system presenting a dynamical cluster, the particles that compose the granular material seem to be ordered according to their velocities. Indeed, the central part of the cell contains mostly slow grains while the surrounding region is composed by fast gas grains. In general, segregation phenomena are not only observed in dilute granular systems but are commonly encountered in each dynamical regime of granular materials.

Every year the industry processes large amounts of granular materials. Unfortunately, most operations induce a segregation of the composing particles of the treated material. The vibrations due to transport or the granular flows trough divers machines can be enough to separate the components of a mixture that was meant to be homogeneous. A similar phenomenon, known as Brazil Nut Effect (BNE) [54–57], occurs when you pour a poly-disperse mixture of particles into a bowl. The more the bowl is manipulated, the more large particles can be found at the surface. For instance, the parts a and b of figure 1.15 show respectively the state of a bi-disperse mixture of spheres before and after vertical shaking of the system. The large metallic beads traveled all the way up to the top of the pile.

Binary granular mixtures do not only segregate because of size variations between the composing particles, various parameters such as the mass or the rugosity of the grains can lead to a
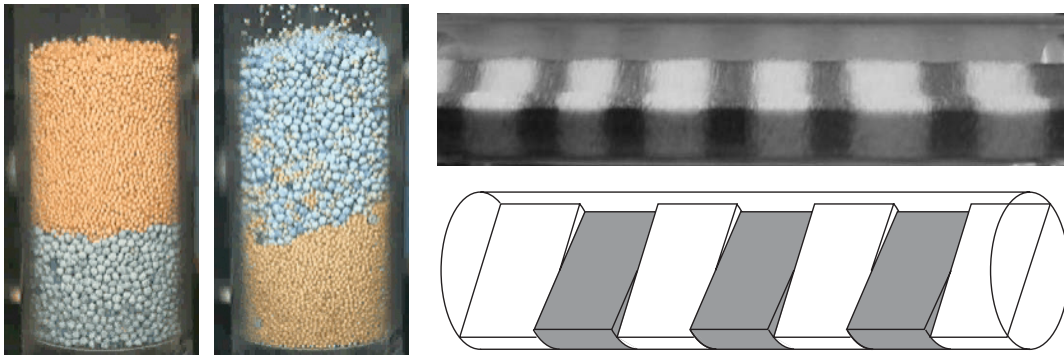
Figure 1.15: (Left, photos by C. Vandu) Initial pile of bi-disperse spheres, large particles are placed on the bottom. After vertical oscillations, the large particles traveled all the way up to the surface. (Right, photo by H. Caps) Rotating cylindre filled with binary granular mixtures. Both granular species have different angles of repose and axial segregation is observed.

separation. In the case of a rotating drum experiment [58–61] as presented in figure 1.15, it is the difference between the angle of repose of both granular species that triggers the segregation. Initially, a homogeneous mixture is placed in a cylindrical container that rotates around its axis of symmetry. Avalanches occur and after a few minutes bands corresponding to the different particle species emerge. Moreover, Magnetic Resonance Imaging (MRI) experiments have shown that a radial segregation is also present in the center of the tube [62].

Segregation can also lead to a localization of granular materials and can be used to sort out its composing grains. As shown in figure 1.16, by dividing the bottom of an oscillating cell containing a granular gas into several subcells, it is possible to locally trap particles. For an initial strong driving, particles move around the system and are not influenced by the subcells. When the driving is sufficiently decreased, grains start to gather in one of the small compartments. This phenomenon is the granular pendant of Maxwell's demon [63,64] and was considered as a paradox for a long time. Indeed, it seems that despite a constant energy injection, the system's entropy decreases since the particles gather. An explanation of the phenomenon is simply given by the dissipative character of the collisions. In order to jump out of its subcell, a particle needs a certain amount of energy that is always granted for strong driving. For lower excitation, it is not that easy for a grain to leave its compartment and rapidly multiple grains can be found in the same subcell. The interactions between those grains lead to a loss of energy so that escaping becomes even more difficult. The consequence of this vicious circle is the gathering of all the particles. Maxwell's granular demon has been studied intensively [65–67]. Different cell geometries and granular mixtures have been tested and even more complex systems as granular fountains [68] and ratchets [69] could be rationalized. Regarding the next section, it is interesting to note that recent studies [70] stress the importance of gravity on the phenomenon.
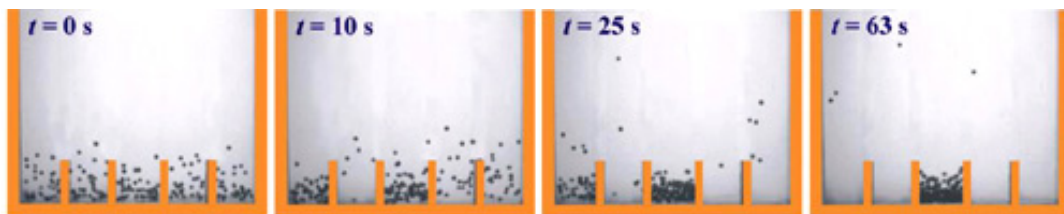
Figure 1.16: (Phys. Rev. Lett cover page april 2002) Granular version of Maxwell's demon. For an initial strong driving, particles move around the system and are not influenced by the subcells. When the driving is sufficiently decreased, grains start to gather in one of the small compartments.

1.7   SpaceGrains project

SpaceGrains (SG) is an international project of the European Space Agency (ESA) whose goal is to study the dynamics and the statistical mechanics of granular materials in microgravity environment. A series of experiments taking place in the ISS are programmed for 2019 and are nowadays prepared by collaborating scientific teams. The experiments focus on various thematics as clustering, thermal fluctuations, convection, segregation and physical phenomena related to excited granular systems. In order to organize the research, four different working packages (WP) were established: WP1 (Granular gases and pattern formation), WP2 (Dense granular systems), WP3 (Convection) and WP4 (Segregation and phase separation). In the instrument, each WP
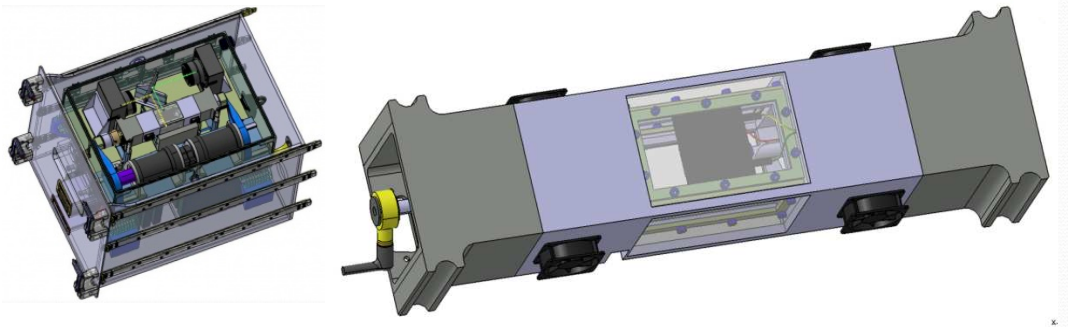
Figure 1.17: Schematic view of the experimental instrument of the SpaceGrains project as presented in september 2011 by COMAT at an ESA Topical Team Meeting in Paris. (Left) Complete payload. (Right) Exchangeable experimental cell.

has a specific cell. Their general design consists of a 3D cell filled with particles where two opposite container walls act as vibrating pistons and inject energy. The containers can be split into several sub-compartments and can be exchanged on the instrument. The number of particles N, the driving amplitude A and the frequency f are tunable parameters of the system. Moreover, the distance L between both pistons at rest can also be modified in order to vary the accessible volume of the cell. Impact force sensors are used to resolve collisions of particles on cell walls and to estimate the velocity distributions of the particles. Accelerometers screwed in the shaft of each vibrating piston allow to infer mean injected power and the temporal fluctuation of injected power. Two high speed cameras film the system, and perform quantitative measurements from particle tracking in dilute regime and correlations between particle displacements. Figure 1.17 shows a schematic view of the instrument and its design.

1.8   Personal contribution

The main goal of this work is to make predictive simulations in order to prepare the working packages WP1 and WP4 of ESA's SpaceGrains project. However, granular materials, being a paradigm of dissipative systems, our research is also of fundamental interest from a scientific and an industrial point of view. The present work is divided into two main parts. The first concerns the gathering of particles in microgravity and the conditions that lead to phase transitions. The second part concerns the manipulation of granular agglomerations and their dynamics in the stationary state.

The main actor in these phenomena is the dynamical clustering process that can be encountered in granular gases. The first step, in this purely numerical work, was the adaptation of our home made software, initially dedicated to granular compaction, to the simulation of granular gases. For this purpose, we proceeded to the reproduction of the Mini-Texus experiment by Falcon *et al.* [52]. A numerical counterpart of the original setup was designed and the same experimental protocol

was applied. All observed dynamical regimes could be reproduced and new ones were discovered. The results concerning this research were published in Physical Review E and are joined to the manuscript.

Once our model validated, we proceeded to first predictive simulations concerning the clustering phenomenon in SpaceGrains. The experimental cell of WP1 was reproduced and the necessary conditions for dynamical clustering were explored. This work is of great importance. One the one hand, it helps to fix the range of the parameters for future experiments, on the other hand it allows a better understanding of the different encountered phenomena et has provided a model predicting the formation of a cluster. Further details are given in our joined article that was published in Europhysics Letters.

Once the clustering mechanism was rationalized, we turned towards the manipulation and the handling of granular materials. Inspired by the work of Dorbolo *et al.* [65], we designed a particular cell geometry which may allow the apparition of Maxwell's demon within the SpaceGrains instrument. We tested numerically a compartmentalized version of the experimental cell in order to trigger locally a dynamical cluster. Our research is exposed in Physical Review E. and is in good agreement with previous works [66, 67].

In parallel to the work concerning Maxwell's demon, we investigated the behavior of a cluster which is exposed to an asymmetrical driving. Indeed, in the SpaceGrains cell, the motion of both pistons is independent and can easily be modified. By tuning the amplitude ratio, in order to obtain a hot and a cold boundary, the cluster's equilibrium position can be moved along the axis of vibration. By connecting several cells via small apertures, this process can be used to create ratchet effects in the system and may provide a way to transport granular materials in microgravity. The global dynamics of the cluster and its fluctuation around the position of equilibrium are described by a theoretical model. Concerning works were submitted to European Physical Journal E.

Finally, the clustering behavior of a bi-disperse granular gas was studied. Dynamical clustering is observed and goes hand in hand with a segregation of the granular material. Deeper investigations concerning the particles of the SpaceGrains experiment were performed and the theoretical model predicting the clustering for a mono-disperse system could be adapted. Taking into account the latest interest of the scientists and companies in the industrial exploitation of asteroids and other near-Earth objects, clustering and segregation phenomena are of great interest since they could help to sort out valuable materials in microgravity. Our results were submitted to European Physical Journal E.

Chapter 2

Molecular Dynamics

In order to study properly a granular gas, long and stable microgravity conditions are required. However, the costs and the preparation time for experiments in parabolic flights, sounding rockets or on the ISS are important. Moreover, strict security requirements have to be respected which often complicates the development of the instruments and may even cause the abortion of some risky experiments. An interesting and powerful answer to this problematic is given by numerical simulations.

2.1 History and origins

Molecular Dynamic (MD) simulations are a computational method developed in the late seventies in order to model the behaviour of atoms and molecules in liquid or gaseous environment. Nowadays, the MD algorithm is still used in biological research for the calculation of the time dependent behaviour of molecular systems. Cundall and Strack [71] were the firsts to transpose MD to granular materials in order to solve problems related to rock mechanics. The method considers soft and deformable particles which interact through multiple collisions that are described by adequate contact and friction laws. Moreover, it allows to calculate the instantaneous positions and velocities of each simulated particle at any moment of time. This remarkable feature grants the access to data that would remain unachievable experimentally. Given the recent technological progress in terms of calculations speed and data storage, MD became more and more efficient and is now one of the most reliable and widespread method for the simulation of granular materials. Further details can be found in [72–74].

2.2 Principle

The basic principle of molecular dynamic simulations relies on a simple algorithm: each particle i is given an initial position $\vec{r}_i(t_0)$ and an initial velocity $\vec{v}_i(t_0)$. During a time step dt, the particles move according to their velocities and new positions are obtained. Overlaps with other grains or with the boundaries of the system may be observed and have to be treated in order to model the corresponding contact. A repulsive force is derived from the depth of the overlap and applied to the concerned particles. Finally, the forces are integrated and new velocities are obtained. Figure 2.1 gives a schematic overview describing the algorithm used for the simulation of soft granular matter.

2.3 Force computation

Whenever two particles i and j collide, a series of forces appear at their point of contact. By defining an appropriate orthonormal basis $\mathcal{B}$, these forces can be decomposed into a normal force
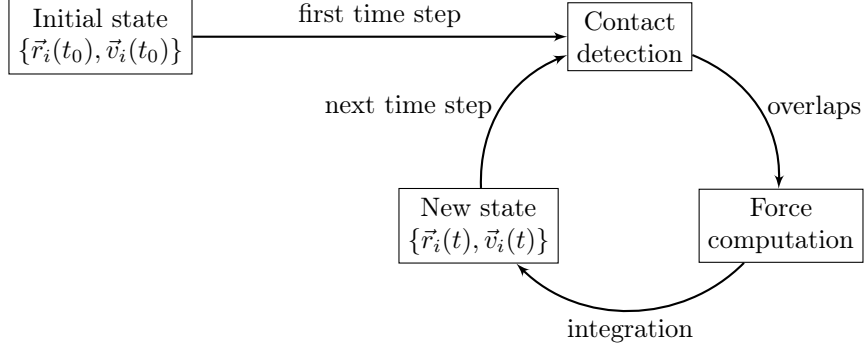
Figure 2.1: Schematic overview describing the principle of the molecular dynamics algorithm used for the simulation of soft granular matter.

$\vec{F}_{ij}^n$ and a tangential force $\vec{F}_{ij}^t$. If one denotes $\vec{r}_i$ and $\vec{r}_j$ the respective positions of both particles the normal vector $\vec{n}_{ij}$, along which the normal force is orientated, is given by

$$\vec{n}_{ij} = \frac{\vec{r}_i - \vec{r}_j}{|\vec{r}_i - \vec{r}_j|}. \tag{2.1}$$

In other words, $\vec{n}_{ij}$ is the unitary vector pointing from particle j towards i. The tangential vector $\vec{t}_{ij}$ is obtained via the sliding velocity $\vec{v}_{ij}^s$ of the contact point. This velocity depends on the translational velocities $\vec{v}_i$ and $\vec{v}_j$ as well as on the rotational velocities $\vec{\omega}_i$ and $\vec{\omega}_j$ of the grains,

$$\vec{v}_{ij}^s = (\vec{v}_i - \vec{v}_j) - \vec{n}_{ij}[(\vec{v}_i - \vec{v}_j) \cdot \vec{n}_{ij}] - (R_i\vec{\omega}_i - R_j\vec{\omega}_j) \times \vec{n}_{ij}. \tag{2.2}$$

The tangential vector can then simply be defined by the normalization of the sliding velocity,

$$\vec{t}_{ij} = \frac{\vec{v}_{ij}^s}{|\vec{v}_{ij}^s|}. \tag{2.3}$$

In order to complete $\mathcal{B}$, the third basis vector $\vec{s}_{ij}$ is defined by $\vec{s}_{ij} = \vec{n}_{ij} \times \vec{t}_{ij}$ and the origin of the axes is the point of contact. Figure 2.2 presents a schematic view of the contact between the particles and the corresponding normal and tangential vectors.
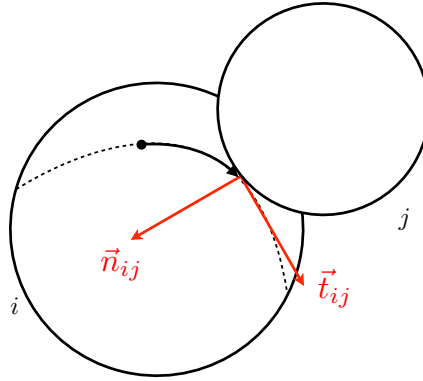
Figure 2.2: Schematic view of contact between two spherical particles i and j. The normal vector $\vec{n}_{ij}$ and the tangential vector $\vec{n}_{ij}$ are represented by red arrows. The bended black arrow corresponds to the displacement of the contact point.

2.3.1 Normal component

When a soft body collides in nature, an elastic deformation is encountered. For instance, when a tennis ball impacts the ground, it flattens since its kinematic energy is partially converted into a potential energy of deformation. Eventually, the stored energy is released and the ball bounces off the court.

In 1882, Hertz proposed a law giving the force that is exerted on such a spherical particle impacting a flat surface [75]. However, in order to model entirely a granular system, this law has to be adapted to the collision between two spherical particles i and j. The resulting contact force depends on the radii R_i and R_j of the grains and on the nature of the used material,

$$F_{ij}^{Hertz} = \frac{2Y}{3(1-P^2)} \sqrt{R_{ij}} |\delta_{ij}|^{3/2} \quad \text{where} \quad R_{ij} = \frac{R_i R_j}{R_i + R_j}. \tag{2.4}$$

The parameters Y and P are respectively the Young and the Poisson moduli. The penetration depth δ_{ij}, which numerically corresponds to an overlap, is defined by $\delta_{ij} = |\vec{r}_i - \vec{r}_j| - (R_i + R_j)$. Despite the great reliability of this model, a simpler law is frequently used to estimate the normal forces at impact. Indeed, Hooke's law describing the force needed to extend or to compress a linear spring can also be used to describe a contact. One has,

$$F_{ij}^{Hooke} = -k_n \delta_{ij}. \tag{2.5}$$

The stiffness parameter k_n is a function of the grain's radii and the Young modulus. Using Hooke's law has the advantage that the duration Δt_c of the contacts does not depend on the impact velocity of the particles. Since multiple collisions, as expected for clustered systems, require a time step dt much smaller then Δt_c, the control of the latter is of great importance. For this reason, we decided to use Hooke's law for our simulations.

Figure 2.3: Modeling of the contact between two spherical particles i and j by a linear spring-dashpot model of stiffness k_n and viscosity ν.

Given the dissipative character of granular materials, a part of the mechanical energy is lost at the impact. This inelasticity can be modeled in different ways. A first very simple approach is to exchange springs during the collision. A first spring of stiffness k_n is used while the spring is compressed and a second one of stiffness $k_e < k_n$ is used at relaxation. The value of k_e is linked k_n via the coefficient of restitution ε according to following relation,

$$k_e = \varepsilon^2 k_n. \tag{2.6}$$

Even though this model grants a good reproduction of the energy loss during a collision, it is not very realistic and another method was used to introduce the dissipation in our simulations. The

loss of energy can also be modeled by adding a viscous friction force to the system. This force depends on a viscosity parameter ν and on the velocity of the deformation,

$$F_{ij}^\nu = -\nu \frac{d\delta_{ij}}{dt}. \tag{2.7}$$

The coupling of this viscous force with Hooke's law, given in equation (2.5), results in a linear differential equation that can be solved analytically. Naming the masses of both particles m_i and m_j, the following relation is obtained

$$m_{ij} \frac{d^2\delta_{ij}}{dt^2} + \nu \frac{d\delta_{ij}}{dt} + k_n \delta_{ij} = 0 \quad \text{where} \quad m_{ij} = \frac{m_i m_j}{m_i + m_j}. \tag{2.8}$$

Accordingly, the contact duration Δt_c and the restitution coefficient ε can be reformulated as,

$$\Delta t_c = \pi \sqrt{\frac{m_{ij}}{k_n}} \left(1 - \frac{\nu^2}{4m_{ij}k_n}\right)^{-1/2}, \tag{2.9}$$

$$\varepsilon = \exp\left(-\frac{\nu}{2m_{ij}}\Delta t_c\right). \tag{2.10}$$

These relationships create a link between the physical parameters, Δt_c and ε, and the numerical parameters, k_n and ν. Practically, k_n can be estimated by balancing the typical kinematic energy of a grain in the system with the potential energy produced by an overlap $\delta_{ij} = R_{ij}/100$. Since ε is fixed by the nature of the material, ν and Δt_c can be easily deduced.

Despite the fact that there are no physical arguments to justify a viscous dissipation, the coupling of a linear spring with a viscous damper, commonly known as linear spring-dashpot, is the most frequently encountered model.

2.3.2   Tangential component

Unless the impact velocities of two colliding grains are perfectly aligned, tangential friction forces appear at contact. These forces can be described by Coulomb's law [76, 77] stating that the tangential force F_{ij}^t is proportional to the normal force F_{ij}^n, in particular,

$$|F_{ij}^t| \leq \mu F_{ij}^n. \tag{2.11}$$

The parameter μ is the dynamic friction coefficient. As one can see in the left part of figure 2.4, the signature of the tangential force is linked to the sliding velocity v_{ij}^s of the contact point and the value of F_{ij}^t is undetermined for $v_{ij}^s = 0$. Since this behavior has to be avoided numerically, a
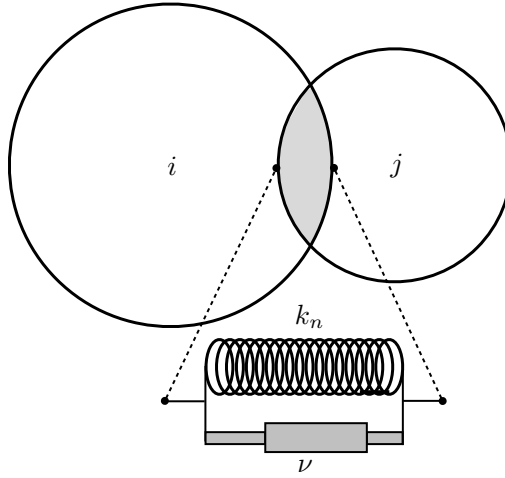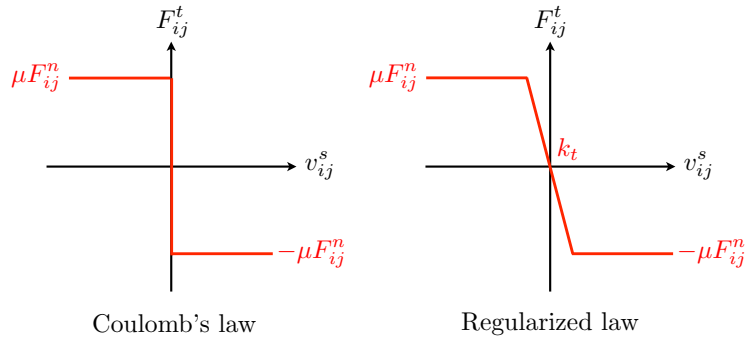

Figure 2.4: Modeling of the contact between two spherical particles i and j by a linear spring-dashpot model of stiffness k_n and viscosity ν.

regularized version of Coulomb's law is used in our simulations. For this purpose, both possible values are connected by a steep segment of slope $k_t \gg k_n$ and the tangential force is given by,

$$F_{ij}^t = -\min(k_t|v_{ij}^s|, \mu F_{ij}^n). \tag{2.12}$$

However, a problem remains, for $v_{ij}^s = 0$ the generated tangential force is nil. This implies that the stabilization of a static pile of grains becomes impossible. Since we will only study dilute dynamic systems, the regularized form of Coulomb's law is sufficient for our simulations.

2.4 Integrating the forces

The next step of the algorithm is to integrate the forces and to move the particles of the system according to Newton's equations of motion. Given the presented decomposition along a normal and a tangential vector, the total force that is exerted by a particle j on a particle i can be written as the following

$$\vec{F}_{ij} = F_{ij}^n \vec{n}_{ij} + F_{ij}^t \vec{t}_{ij}. \tag{2.13}$$

The corresponding torque $\vec{M}_{ij}$ is given by

$$\vec{M}_{ij} = R_i \vec{F}_{ij} \times \vec{n}_{ij}. \tag{2.14}$$

At each time step, the following system of equations has to be solved for all particles in order to deduce the all new positions and velocities based on their old values. One has,

$$\begin{cases} m_i \dfrac{d\vec{v}_i}{dt} = \sum_{j \neq i} \vec{F}_{ij} + \vec{F}_{i,ext} \\[2em] I_i \dfrac{d\vec{\omega}_i}{dt} = \sum_{j \neq i} \vec{M}_{ij} \end{cases} \tag{2.15}$$

where $\vec{F}_{i,ext}$ is the sum of all external forces acting on the particle i. The parameter I_i corresponds to the inertia of a filled spherical particle of mass m_i and radius R_i rotating around its axis of symmetry. Applying a second order theta-method, with $dt = \Delta t_c/100$ for the numerical integrations, leads to the new position,

$$\vec{r}_i(t + dt) \;=\; \vec{r}_i(t) + \vec{v}_i(t)\frac{dt}{2} + \vec{v}_i(t + dt)\frac{dt}{2}, \tag{2.16}$$

$$\vec{v}_i(t + dt) \;=\; \vec{v}_i(t) + \frac{1}{m_i}\sum_{j \neq i} \vec{F}_{ij} dt + \vec{F}_{i,ext} dt. \tag{2.17}$$

The rotation of a vector $\vec{a}$ through an angle θ around a unit vector $\vec{u} = (u_x, u_y, u_z)$ can be realized via the well known three dimensional rotation matrix $\mathcal{R}(\vec{u}, \theta)$ given in (2.18). Accordingly, the components of $\vec{a}$, after the rotation, are given by $\mathcal{R}(\vec{u}, \theta)\vec{a}$. The matrix is given by

$$\begin{pmatrix} \cos\theta + u_x^2(1 - \cos\theta) & u_x u_y(1 - \cos\theta) - u_z \sin\theta & u_x u_z(1 - \cos\theta) + u_y \sin\theta \\ u_y u_x(1 - \cos\theta) + u_z \sin\theta & \cos\theta + u_y^2(1 - \cos\theta) & u_y u_z(1 - \cos\theta) - u_x \sin\theta \\ u_z u_x(1 - \cos\theta) - u_y \sin\theta & u_z u_y(1 - \cos\theta) + u_x \sin\theta & \cos\theta + u_z^2(1 - \cos\theta) \end{pmatrix}. \tag{2.18}$$

However, this method requires an important number of operations and leads to an accumulation of numerical imprecisions. A more stable method consists in the application of quaternion calculation. The set of quaternions $\mathbb{H}$ is a four dimensional vector space over the real numbers. It is provided with three intern operations: addition, scalar multiplication and a more particular one called the Hamiltonian product ($*$). This definition requires the choice of a basis which is

generally denoted as $(\mathbf{1}, \mathbf{i}, \mathbf{j}, \mathbf{k})$ where $\mathbf{1}$ is the identity quaternion. Accordingly, every $\mathbf{q} \in \mathbb{H}$ can be written as

$$\mathbf{q} = q_0 \mathbf{1} + q_1 \mathbf{i} + q_2 \mathbf{j} + q_3 \mathbf{k} = (q_0, q_1, q_2, q_3). \tag{2.19}$$

Let $\mathbf{p}$ and $\mathbf{q}$ be two quaternions and r a scalar. One has,

$$\mathbf{q} + \mathbf{p} = (q_0 + p_0, q_1 + p_1, q_2 + p_2, q_3 + p_3), \tag{2.20}$$
$$r\mathbf{q} = (rq_0, rq_1, rq_2, rq_3). \tag{2.21}$$

The Hamiltonian product is given by

$$\mathbf{q} * \mathbf{p} = \begin{pmatrix} q_0 p_0 - q_1 p_1 - q_2 p_2 - q_3 p_3 \\ q_0 p_1 + q_1 p_0 + q_2 p_3 - q_3 p_2 \\ q_0 p_2 + q_2 p_0 - q_1 p_3 + q_3 p_1 \\ q_0 p_3 + q_3 p_0 + q_1 p_2 - q_2 p_1 \end{pmatrix}. \tag{2.22}$$

It is now possible to make a link between the classical rotation matrix and the set of quaternions. For any quaternion $\mathbf{q} \in \mathbb{H}$, one can define following matrix

$$\mathcal{R}(\mathbf{q}) = \begin{pmatrix} 1 - 2q_2^2 - q_3^2 & 2q_1 q_2 - 2q_3 q_0 & 2q_1 q_3 + 2q_2 q_0 \\ 2q_1 q_2 + 2q_3 q_0 & 1 - 2q_1^2 - 2q_3^2 & 2q_2 q_3 - 2q_1 q_0 \\ 2q_1 q_3 - 2q_2 q_0 & 2q_2 q_3 + 2q_1 q_0 & 1 - 2q_1^2 - 2q_2^2 \end{pmatrix}. \tag{2.23}$$

Using simple trigonometric relations, one can show that $\mathcal{R}(\mathbf{p}) = \mathcal{R}(\vec{u}, \theta)$ if one chooses the quaternion $\mathbf{p}$ as the following

$$\mathbf{p} = \left(\cos\frac{\theta}{2}, u_x \sin\frac{\theta}{2}, u_y \sin\frac{\theta}{2}, u_z \sin\frac{\theta}{2} \right) = \left(\cos\frac{\theta}{2}, \vec{u} \sin\frac{\theta}{2} \right). \tag{2.24}$$

Finally, using the definition of the Hamiltonian product, one can easily prove that several rotations can be composed so that one has

$$\mathcal{R}(\mathbf{q})\mathcal{R}(\mathbf{p}) = \mathcal{R}(\mathbf{q} * \mathbf{p}). \tag{2.25}$$

In our simulations each particle i is orientated via its own local basis $\mathcal{E}_i(t)$ that can be represented by a three dimensional matrix. The latter is initialized by the vectors $\vec{e}_x = (1, 0, 0), \vec{e}_y = (0, 1, 0)$ and $\vec{e}_z = (0, 0, 1)$ meaning that $\mathcal{E}_i(0) = \mathcal{I}, \forall i$. This particular choice yields in an instantaneous evaluation of the new basis after the first rotation. Thanks to relation (2.25), this method can be used recursively so that the numerical effort for the next rotations is reduced to the calculus of a Hamiltonian product (28 operations) instead of a matrix product (45 operations). All we have left to do is to make the link between the angular velocities of the grains and the quaternions. From relation (2.15) it is possible to deduce the new angular velocity,

$$\vec{\omega}_i(t + dt) = \vec{\omega}_i(t) + \frac{1}{I_i} \sum_{j \neq i} \vec{M}_{ij} dt. \tag{2.26}$$

As for the linear position $\vec{r}_i(t + dt)$, the angular position $\theta_i(t + dt)$ is obtained via a second order theta-method for which each particle i rotates at angular velocity $\vec{\omega}_i(t)$ during the first half time step and at $\vec{\omega}_i(t + dt)$ during the second. If one defines the quaternions $\mathbf{p}_i(t + dt)$ and $\mathbf{q}_i(t + dt)$ as the following,

$$\mathbf{p}_i(t + dt) = \left(\cos\frac{||\vec{\omega}_i(t)||dt}{4}, \frac{\vec{\omega}_i(t)}{||\vec{\omega}_i(t)||} \sin\frac{||\vec{\omega}_i(t)||dt}{4} \right), \tag{2.27}$$

$$\mathbf{q}_i(t + dt) = \left(\cos\frac{||\vec{\omega}_i(t + dt)||dt}{4}, \frac{\vec{\omega}_i(t + dt)}{||\vec{\omega}_i(t + dt)||} \sin\frac{||\vec{\omega}_i(t + dt)||dt}{4} \right). \tag{2.28}$$

the new angular position is obtained by multiplying $\mathbf{q}_i(t + dt) * \mathbf{p}_i(t + dt)$ with the product of all previous rotation quaternions noted $\mathbf{P}_i(t)$. Given relation (2.25), the corresponding rotation matrix gives automatically the new local basis of the particle i. Indeed, one has

$$\mathcal{E}_i(t + dt) = \mathcal{R}(\mathbf{q}_i(t + dt))\mathcal{R}(\mathbf{p}_i(t + dt))\mathcal{E}_i(t) = \mathcal{R}(\mathbf{q}_i(t + dt) * \mathbf{p}_i(t + dt) * \mathbf{P}_i(t))\mathcal{I}. \tag{2.29}$$

2.5 Applications

In the following section, some applications of our algorithm are proposed in order to demonstrate the polyvalence of MD and to highlight the importance of several numerical parameters as friction and restitution. Segregation phenomena and particular behaviors of granular flows are reproduced and the velocity distributions of driven rod-shaped particles are captured.

2.5.1 2D billiard

The example of a two dimensional billiard demonstrates the importance of the friction in the system. The simulations start with five discs at rest (gray points) in the system and another disc (black point) with an initial velocity $\vec{v}_0$. The further evolution of the system depends strongly on the friction coefficient. Figure 2.5 describes the trajectories of all particles (for $\mu = 0.4$ on the left and $\mu = 0$ on the right side) during three seconds. One can easily see that the system's dynamics are modified since the first collision. Moreover, it is to note that the presence of friction leads to partial transformation of the kinematic energy of translation into and kinematic energy of rotation which might explain why the frictional system is less explored.

$\mu = 0.4$ $\qquad\qquad\qquad$ $\mu = 0.0$
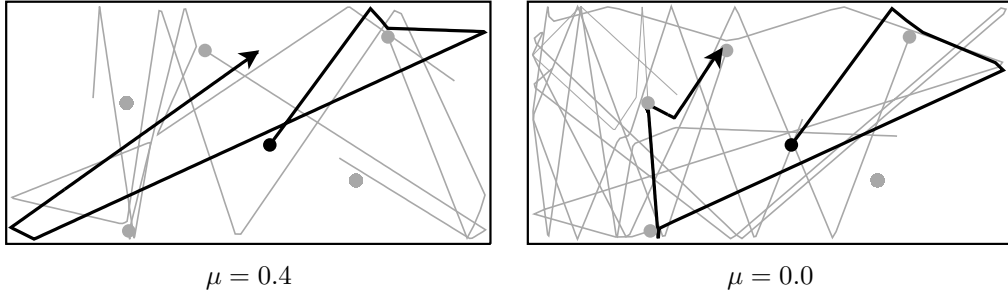
Figure 2.5: Importance of the friction μ in a two dimensional billiard. Both simulations starts with five discs at rest (gray points) in the system and another disc (black point) with an initial velocity $\vec{v}_0$. The system's dynamics are modified since the first collision.

2.5.2 Rotating drum

As presented in the introduction, a granular material can be fluidized using a rotating drum. Since the presented tangential model doesn't allow us to reproduce static phenomena, we focused on a system with high rotation speed. We realized a two dimensional simulation (in analogy to a Hele-Shaw cell) in which 1200 grains of radius R are rotated at high frequency ω in a drum of radius $R_d \gg R$. As expected a steady granular flow is obtained and the surface presents the typical S-shape as explained in section 1.3. Figure 2.6 presents a photography of the central region in a rotating drum (left) and snapshots from the simulation (right). The linear color gradient describes the speed of the particles normalized by the linear speed $R_d\omega$ of the drum's wall. This particular study shows that, thanks to a simple modeling of the contact forces at the scale of the particles, a macroscopic phenomenon can be reproduced efficiently. The following section is dedicated to another of these phenomena.

2.5.3 Brazil nut effect

In this simulation we placed a large (gray) grain in the lower part of a mono disperse pile of small particles. The system is then agitated continuously according to a sinusoidal signal. During the driving the large particle rises upwards until it reaches the surface after about 10 seconds (see figure 2.7). The color gradient applied on the small particles corresponds to the vertical component of the velocity. The latter suggests the presence of convection in the system which
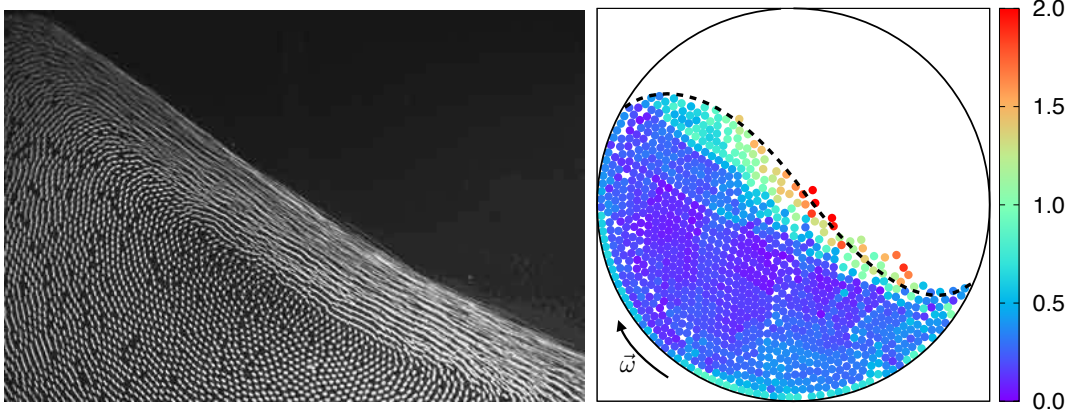
Figure 2.6: (Left, Photography by Hubert Raguet) Experimental view of the central region in a rotating drum. Surface flow and a slight S-shape are visible. (Right) Snapshot taken from our rotating drum simulation. Steady granular flow and surface curvature is obtained. Color gradient describes the speed of the particles normalized by the linear speed of the drum's wall.

helps our intruder to realize its upwards movement. Once again our model gives excellent results. Let us now consider more dilute systems such as the granular gases as studied by Harth and coworkers [42] and analyze the distribution of the internal speeds.

| 0s | 1s | 3s | 6s | 9s |
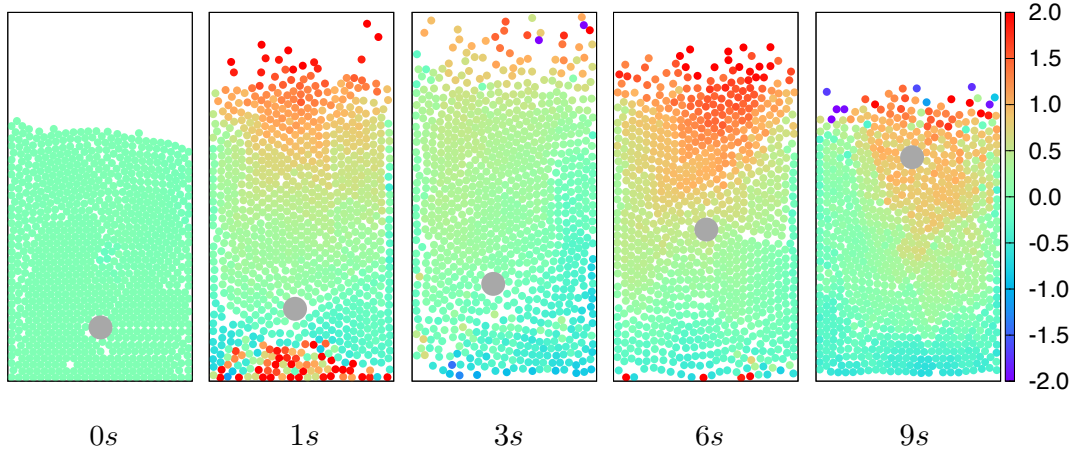
Figure 2.7: Simulation of the Brazil nut effect. The large intruder particle rises up in a driven media composed by smaller grains. Convection may play a role in the process as suggested by the distribution of the vertical velocities in the system.

2.5.4 Granular gases

An interesting feature of our simulations is the possibility to create our own particles by agglomerating spheres. For each particle a corresponding center mass $\vec{c}_m$ and an inertia matrix can be computed. The contacts between two particles are detected by testing the contacts between their composing spheres. The particle is moved by integrating all the forces, as they were acting on $\vec{c}_m$, and all the torques, by taking into account the distance of the contact point to the center of mass.

In our simulations, we realized rod shaped particles by aligning five spheres of radius R. The latter overlap and form a spherocylinder of length $l = 6R$. In order to reproduce gas like dynamics, 150 rods are enclosed in a rectangular container. The whole system is then driven during 5 seconds

with an amplitude A at frequency f. During the last second of simulation we recorded the linear as well as the angular velocities of the particles in the system. Based on this data we established the Probability Density Functions (PDF) of the normalized velocities:

$$u_i = \frac{v_i}{2A\pi f}, \quad \Omega_i = \frac{w_i}{2\pi f}; \tag{2.30}$$

where $i \in \{x, y, z\}$. All six distributions could be fitted by the universal law (1.5), presented in the introduction. Since the excitation is uniaxial, the distributions along x and y are quasi identical and can be plotted on the same graph. The distributions of the linear and the angular velocities are presented in figure 2.8. The normalized velocities along the x, y and the z axes are represented by crosses, circles and triangles respectively.
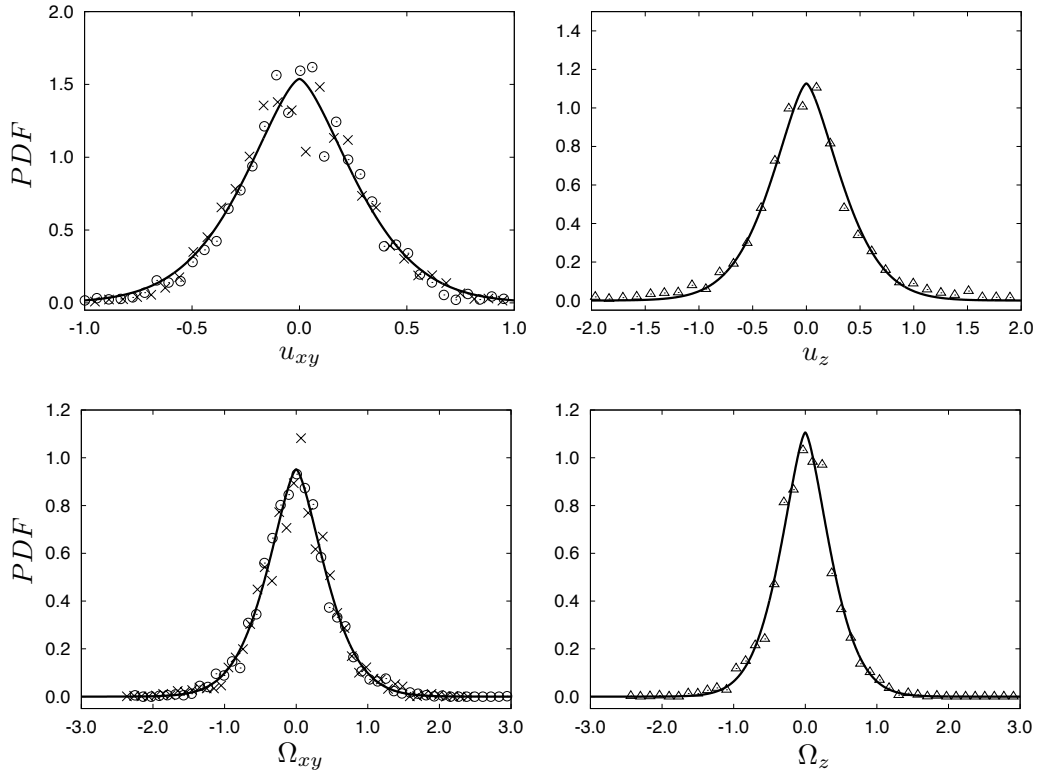
Figure 2.8: Distributions of the normalized velocities along the x, y (left column) and the z axes (right column) represented by crosses, circles and triangles respectively. The solid black line, corresponding to the universal law presented in the introduction, is in excellent agreement with our numerical data.

2.6 Other methods

Molecular dynamics do not represent the only way to simulate granular materials. In the following two sections, a brief overview of two other popular algorithms that are used in the field of granular physics will be given.

2.6.1 Event Driven Simulations (ED)

As the name suggests it, this algorithm is based on a series of events that occur one after each other. An event can be a collision, the addition of a new external force or any modification of

the system that could have an impact on its dynamics. Since the system is not modified between two events, there is no reason to model it during this period. Accordingly, the simulation jumps from one event to the next which implies a dynamic time step. At each event, the positions and velocities of the relevant bodies are computed and a new time step (allowing to jump to the next event) is evaluated. For dilute systems this method is very efficient. However, high densities imply multiple collisions or even permanent contacts between particles. In such situations, the resulting time step is nil and the simulation has to be aborted. In order to avoid the problem, a hybrid algorithm, mixing ED and MD can be used. Indeed, once the time step becomes too small to assure a efficient modeling of the system via event driven simulations, the algorithm switches towards molecular dynamics until the critical situation is resolved.

2.6.2   Non Smooth Contact Dynamics (NSCD)

The non smooth contact dynamics algorithm has been developed in order to simulate frictional hard spheres [78]. Unlike MD, the repulsive normal component in NSCD is derived from the relative velocity at the impact. Moreover, Coulomb's law is used in its exact form, without any regularization. In order to avoid any indetermination, additional equations (a discretized form of Newton's third equation) are added into the system which leads to a coupling of all the contact forces along the network of contacts. This model is particularly interesting for quasi static systems for which large time steps can be used.

Part II

Gathering of granular materials in microgravity

Chapter 3

Phase transitions in granular gases

The dissipative character of a granular gas leads to a series of intriguing phenomena. The granular temperature of the system drops continuously and dense agglomerates begin to form. The system transits from a gaseous state towards a clustered state. The latter can be seen as a cold granular liquid surrounded by a hot granular gas. In the late nineties, the first dynamical cluster is observed in microgravity environment [52]. Realizing a series of experiments in a Mini-Texus sounding rocket, Falcon *et al.* studied the dynamics of driven granular material. Three filling fractions were tested and led to different behaviors. Moreover pressure measurements were performed using piezoelectric sensors.

3.1 Motivations

In this chapter, I will present our work concerning granular phase transitions. In a first paper, we reproduced Falcon's experiment [52] in order to validate our numerical model. This step is very important since the rest of our work relies on the efficiency of our numerical model. Moreover a deeper investigation of the original system was performed and additional dynamical regimes were detected. In a second publication, we investigated the impact of the driving parameters on the cluster formation and linked the different dynamics to the mean kinematic energy in the system.

3.2 Original setup

The experiment is composed of three cubic cells of 1 cm^3 in inner volume. The cell's walls are made of clear sapphire in order to allow a good vision while resisting to the constraints of the experiment. Each cell is respectively filled with about 1420, 2840 and 4510 bronze spheres of diameter 0.3-0.4 mm. An electrical motor drives the system sinusoidally at a frequency f with an

N = 1240   N = 2480   N = 4510
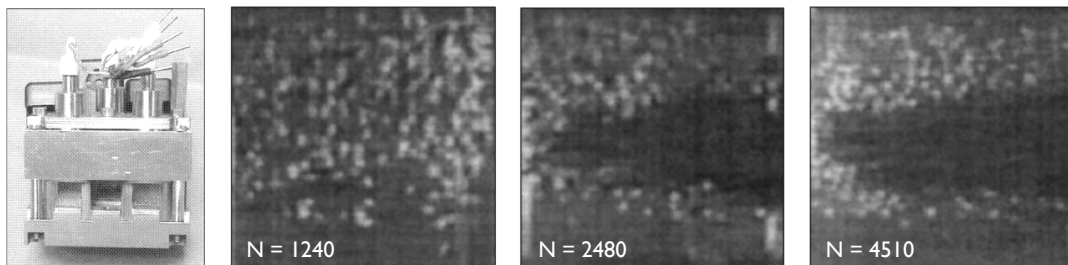
Figure 3.1: (Left) Experimental cells used by Falcon *et al* during sounding rocket experiments [52]. (Right) First observations of three dimensional dynamical clusters. The filling number N increases from left to right. For large values of N, a dense and slow region forms in the center of the cell.

amplitude A. The latter parameters are varied during the experiment in the ranges 1 to 60 Hz and 0.1 to 2.5 mm respectively. The dynamics of the experiment are recorded via a CCD camera fixed in the frame of the space probe. In order to realize pressure measurements, a piezoelectric sensor is fixed at the top of each cell. A photography of the experimental setup is shown in the left part of figure 3.1. The right part is a snapshot of the three cells taken at maximum downward velocity for $f = 30$ Hz and $A = 2.5$ mm.

3.3   Experimental results

Falcon *et al* noted that, for increasing density, the particles in the cell interacted via inelastic collisions which led to the formation of a dense and motionless cluster surrounded by a loose granular gas. The latter behavior can be seen on the snapshot of the densest cell. For an intermediate filling, a smaller cluster is reported. Indeed, the agglomerate doesn't seem to spread out in the entire horizontal plane.

3.4   Reproducing the experiment

In order to compare qualitatively the visual output of our simulations we choose to reproduce the experiment corresponding to figure 3.1 ($f = 30$ Hz and $A = 2.5$ mm). We simulated spherical particles with a density $\rho = 8000$ kg/m^3 and a radius $R = 0.175$ mm which roughly corresponds to the mean radius of the grains in the experiment. The coefficients of friction and restitution are respectively fixed to 0.2 and 0.9. Particles are placed randomly and at rest in the three cubic cells and are driven during 10 seconds (*i.e.* 300 cylces). In a second run, we realized a large number of simulations in which we varied the number as well as the size of the particles in order to explore more deeply the system's behaviors.

3.5   Main results

The first important result of this study was the validation of our numerical model. As shown in figure 3.2, all experimentally observed dynamics could be reproduced in our simulations. One can note the excellent qualitative agreement with the experimental data presented in figure 3.1.
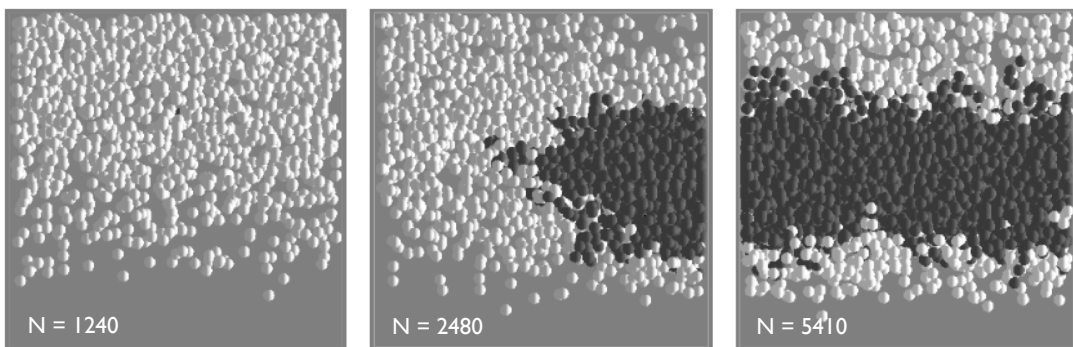
Figure 3.2: (Taken from [79]) Snapshots of the simulations corresponding to Falcon's Mini-Texus experiments. All observed dynamics are recovered and an excellent qualitative agreement with the pictures of figure 3.1 is obtained. Dark shading corresponds to dense zones in the system.

A second result was the observation of new dynamics in the system. Indeed, we realized simulations with even higher fillings than in Falcon's experiment. Above a certain threshold, a collective and coherent motion of the particles appears. The entire granular media behaves as one single completely dissipative particle called the bouncing aggregate. Bouncing modes are observed

and can be explained regarding the bouncing ball paradigm [80]. This specific behavior has been observed experimentally by Bannerman, Kollmer and Sack [81–83] (see section 3.8). The final result of our work was the realization of a phase diagram classifying the different encountered dynamics (I granular gas, II partial cluster, III complete cluster and IV bouncing aggregate) according to the packing fraction[1] ϕ of the system and the normalized particle size r. In order to treat efficiently the great amount of collected data, we developed an automated and reliable cluster detection method based on a Kolmogorov-Smirnov (KS) test [84] that we continue to use throughout all of our studies. The transition points detected by this method are represented by circles, diamonds and squares on the below figure.
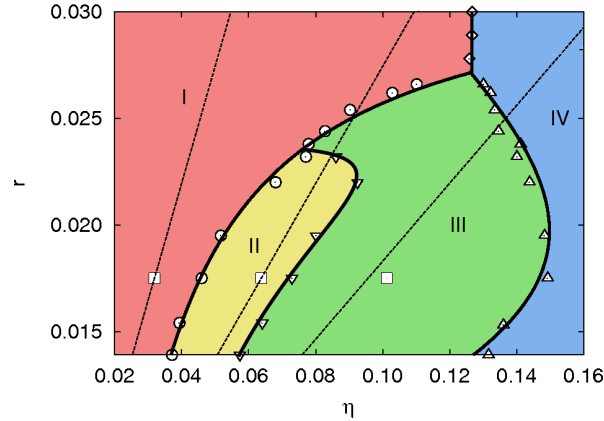
Figure 3.3: (Taken from [79]) Phase diagram describing the four encountered dynamical regimes. I granular gas, II partial cluster, III complete cluster and IV bouncing aggregate. Squares correspond to Falcon's experiment, circles, diamonds and triangles correspond to the transition points that were detected by our statistical method. Solid curves are only visual guidelines.

3.6 Conclusion

The results of this first study allow us to validate our numerical model. Moreover, the reliability of our algorithm has been reinforced by the experimental observation of the bouncing aggregate [81–83]. Finally, our work has shown that the dynamics in driven systems are much richer than expected and that the encountered transitions can't be explained by simple arguments as a limit density or a critical number of granular layers [85] (represented by dashed lines on figure 3.3).

---

[1]In the articles [79, 86] the symbol η was used instead of ϕ for the denomination of the packing fraction.

Phase transitions in vibrated granular systems in microgravity

E. Opsomer, F. Ludewig, and N. Vandewalle

GRASP, Physics Department B5a, University of Liège, B-4000-Liège, Belgium

We numerically investigated various dynamical behaviors of a vibrated granular gas in microgravity. Using the parameters of an earlier Mini-Texus 5 experiment, three-dimensional simulations, based on molecular dynamics, efficiently reproduce experimental results. Using Kolmogorov-Smirnov tests, four dynamical regimes have been distinguished: gaseous state, partial clustering, complete clustering, and bouncing aggregates. Different grain radii and densities have been considered in order to describe a complete (r,η)-phase diagram. The latter exhibits rich features such as phase transitions and triple points. Our work emphasizes the complexity of diluted granular systems and opens fundamental perspectives.

I. INTRODUCTION

Granular materials exhibit a great number of intriguing behaviors. Unlike continuous states, the dissipative character of the interactions between the constituents of a granular system triggers phenomena such as inelastic collapse [1] and clustering [2,3]. Nevertheless, granular materials can be found in different dynamical regimes similar to classical thermodynamical states. Solid and liquid regimes have been thoroughly investigated during the past few decades (rotating drums [4], granular compaction [5,6], granular flow [7–9]). Several models were established but could not give answers to all fundamental questions [10]. The gas regime is far more complex. Because of the numerous dissipative collisions, the gaseous state needs a constant external energy supply to subsist. Experimentation with vertically driven granular material revealed the presence of resonance phenomena [11] convecting rolls and granular Leidenfrost effects [12]. Gravitational forces are an important factor for the dynamics that the system displays [11,13]. In microgravity, pioneer work has been done by Falcon *et al.* during Mini-Texus 5 experimentation [3]. The presence of clustering has been reported. Different theoretical mechanisms have been proposed to explain its formation [1] but, experimentally, the criterion for the appearance of the phenomenon is related to the number of layers in the box [3]. The transition between the gas and the denser regime has motivated several studies and phase diagrams depending on the vibration parameters A and ω and the restitution coefficient ε have been established [14,15].

This work aims to perform numerical simulations in order to emphasize the relevant parameters that trigger clustering in a driven granular gas. We will show that clusters are dynamic structures and that their formation is more complex than expected.

II. MODEL

We are using a 3D model based on molecular dynamics [16,17] where friction and angular momentum are taken into account. Our approach differs from earlier simulations of hard sphere granular gases based on event-driven algorithms [1,18] where inelastic collapse was avoided by using a time cutoff model [19]. The system is made of N spherical particles gathered in a cubic container of size L^3 following a sinusoidal motion of amplitude A and angular velocity $\omega = 2\pi f$ along the z axis. Identical particles have a mass m and a radius R. At initialization, each one is given a different random position (that allows no contact between the particle and the rest of the system). Moreover, their initial linear and angular velocities are null. Contact forces are computed following two simple models.

Normal forces F_{ij}^n are composed by a repulsive (F_{ij}^{rep}) and a dissipative (F_{ij}^{dis}) component. The repulsive component follows a simple Hooke's Law,

$$F_{ij}^{\mathrm{rep}} = -k_n \delta_{ij}, \tag{1}$$

where $\delta_{ij} = d_{ij} - 2R$ with d_{ij} the distance between the centers of the solids i and j. The constant k_n is the normal stiffness which is a purely numerical parameter. Indeed, this stiffness is not linked to specific physical properties of the simulated material. It's value is calculated in order to keep the static deformation of the particles lower than $10^{-4}R$. (In our simulations k_n ranges typically between 100 and 1000 kg/s^2). The dissipative component is taken into account by viscous forces according to the following law:

$$F_{ij}^{\mathrm{dis}} = -\gamma_n(k_n, \varepsilon) \frac{\partial \delta_{ij}}{\partial t}, \tag{2}$$

where the viscous constant γ_n is a nontrivial function of the normal stiffness k_n and the restitution coefficient ε. This restitution coefficient is used for both grain-grain and grain-wall collisions. In contrast to other models (like Hertz's model) using a Hooke's Law and viscous dissipation allows us to work with a constant contact duration Δt, independent of the impact velocities. In order to assure the integration of the forces, each contact should be resolved in about 100 time steps τ (i.e., $\tau \approx \Delta t / 100$).

Tangent forces F_{ij}^t are bounded and depend on the relative tangent velocities v_{ij}^t between the colliding solids i and j. One has

$$F_{ij}^t = -k_t v_{ij}^t \quad \text{and} \quad \left\| F_{ij}^t \right\| \leqslant \mu F_{ij}^n, \tag{3}$$

where μ is a friction coefficient and k_t a purely numerical constant. The friction coefficient μ as well as the restitution coefficient ε can be adapted to fit the intrinsic properties of the system. A complete description of MD simulations is given by Taberlet [20].
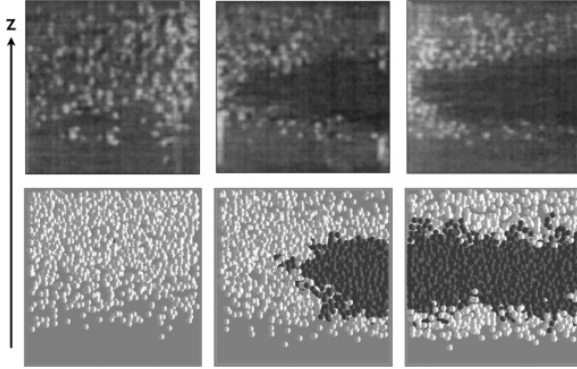
FIG. 1. (Top row) The experimental results for respectively $N = 1420$, 2840, and 4510 particles at the box maximum downward velocity [3]. Falcon's experiments are represented by a square in Fig. 5. (Bottom row) Numerical results in the same conditions. Dark gray shading of the cluster is realized by a proximity rule described in the text.

III. RESULTS

In a first step, we reproduced the results of Falcon *et al.* [3]. Bronze spheres of radius R are confined in a box of size L considering the ratio $r = R/L = 0.0175$. The system is oscillating with an amplitude of $A/L = 0.25$ and a frequency of $f = 30$ Hz along the z axis. We set the friction coefficient to $\mu = 0.2$, the restitution coefficient to $\varepsilon = 0.9$, and the volume density to $\rho = 8 \times 10^3$ kg/m^3. Figure 1 presents, from left to right, the system with $N = 1420$, 2840, and 4510 particles at its maximum downward velocity, $-A\omega$. Dense regimes can be observed thanks to shading effects [3]. The lower three pictures of Fig. 1 correspond to our simulations where the dark gray particles belong to the central cluster according to a simple proximity rule: (i) two particles are neighbors if the distance between them is less than $2.5r$; (ii) particles that are close enough to the system's center of mass form a seed; (iii) step by step, the seed is extended by its neighbors; and (iv) when no other neighbors are found, the obtained cluster is colored gray (see Fig. 1). Our simulations are in qualitative agreement to the real experiment presented in the upper row. Indeed, the most diluted system ($N = 1420$) of Fig. 1 remains in a gaseous state and presents a density gradient decreasing toward the center of the box. The densest case ($N = 4510$) presents clustering around the center of the box and the distribution is homogeneous over the xy plane (i.e., the plane that is perpendicular to the direction of oscillations). However, the intermediate case ($N = 2840$) presents partial clustering: the cluster does not occupy the entire xy plane. The latter behavior was not addressed in Falcon's experiment but can be seen in their pictures.

Based on these results, we realized a larger series of simulations in the same conditions as Falcon *et al.* but modifying the dimensionless radius r of the particles and the volume fraction or density $\eta = 4N\pi r^3/3$ of the system. Since we work with different grain sizes this last parameter seems more appropriate than N. We choose 16 different values of r ranging from 0.0139 to 0.032 and about 60 fixed density values η ranging from 0.02 to 0.16. Unlike to the restitution ε, these
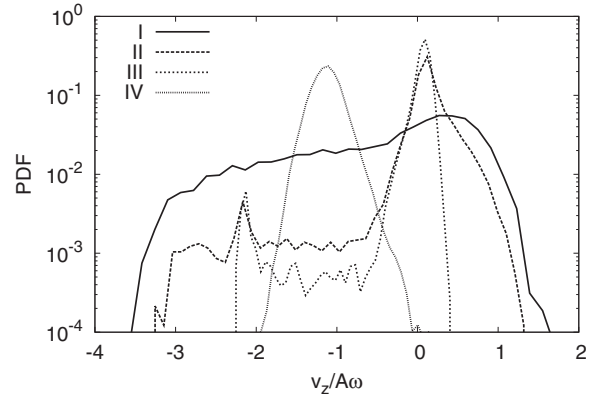
FIG. 2. Semilog plot of the probability density function (PDF) of the particle velocity along the z axis. Data is collected at the boxes maximum downward velocity $(-A\omega)$ for the four different dynamical regimes.

geometrical parameters can be easily tuned in experiments. In our simulations, we distinguished four different dynamical regimes as follows:

(i) Gaseous state: Encountered in dilute systems, the grains exhibit a broad and asymmetric distribution of vertical velocities v_z as shown in Fig. 2. This asymmetry evolves according to the phase oscillation of the box. Particles can be found everywhere in the system, but their density is decreasing from one wall toward the center of the box, as shown in Fig. 3.
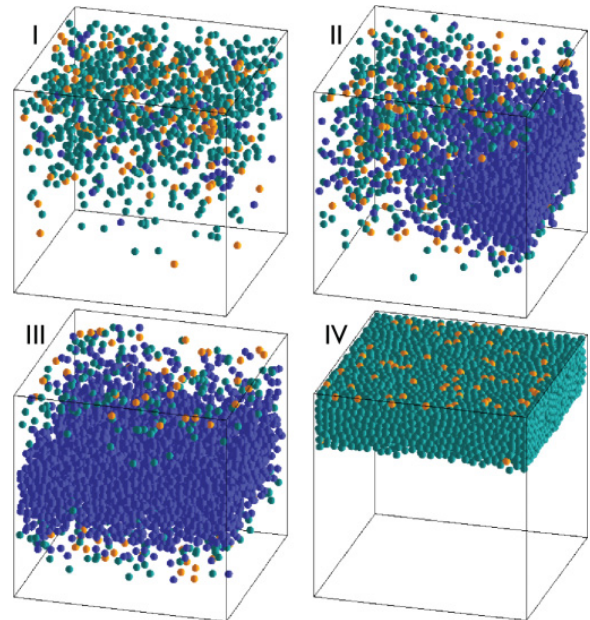
FIG. 3. (Color online) Snapshots of the four dynamic regimes when the box is at its maximum downward velocity $-A\omega$. Different colors correspond to selected ranges of the vertical velocity: dark gray (blue) if $|v_z| < A\omega$, gray (green) if $A\omega \leqslant |v_z| < 2A\omega$, and light gray (orange) if $2A\omega \leqslant |v_z|$.

According to earlier experimentations [21,22], we found v_x and v_y distributions of the form $\exp(-|v/v_0|^\gamma)$ with $\gamma \in \{1,2\}$ and v_0 as fitting parameter.

(ii) Partial clustering: For some values of the parameters, the system presents a partial clustering. Particles are more or less stabilized around the origin of the z axis but then start to gather along a wall of the box. It could be assumed that the system needs a typical cluster width to be energetically stable. In the distribution of velocities along z (Fig. 2), a sharp peak appears around zero which is a signature for clustering. However, the distribution remains broad since a gaseous regime coexists in the system. Multiple simulations have shown that cluster can appear on a particular lateral wall with a probability 1/4. Moreover, simulations in a cylinder with identical volume and base section revealed that the lateral clustering is not related to corner effects. Note that the partial cluster is a subphase of the following total cluster.

(iii) Complete clustering: When the density increases, we observe that the cluster spreads over the entire xy plane. A peaked velocity distribution around zero can be observed in Fig. 2. One can note the presence of a second peak at $v_z = \pm 2A\omega$ (also seen for partial clustering) due to the granular gas trapped in between the cluster and the vibrating walls. A steady state due to the balance of condensation and evaporation of the cluster is observed. By tracking particles and analyzing the dynamics of clusterization during several periods, we can conclude that the cluster is a dynamic state with a constant renewal. Indeed, high-speed particles arriving from the walls crush into the cluster, dissipate their energy, and eventually become part of the cluster. The energy partially transmitted across the cluster provokes internal rearrangements and eventually ejects particles. It should be noted that the packing fraction measured inside the cluster is about $\eta = 0.30$ which is far below the jamming limit. A deeper analysis of the collision frequency is also needed and will be published elsewhere.

(iv) Bouncing aggregate: For denser systems a new phenomenon is observed, the large amount of granular material confined in the system leads to higher kinetic energy than in other regimes. This energy cannot be dissipated only through successive collisions like in a cluster. Indeed, the local density in the system's center is high enough to assure permanent contacts between many particles, when the gaseous phase encounters this denser region all the grains are pushed toward the wall. The bouncing state is characterized by a coherent motion of all particles and peaked velocity distribution around $\pm A\omega$. Particles stay gathered in a dense arrangement that describes a movement similar to a totally dissipative bouncing ball [23]. Moreover, density distribution along the z axis reveals crystal-like structures inside the packing. In particular, layers along the xy plane are observed.

In order to discriminate these four dynamic regimes, the elaboration of an automated and reliable cluster detection algorithm is of a capital interest. We choose a statistical test based on the spatial distribution of the particles. Unlike in the velocity distribution, the spatial distribution follows a well-known theoretical law. Indeed, at very low densities, when the system is assumed to be in a gaseous state, collecting data every half-period during the last 5 s of simulations demonstrated that the particle distribution along the three axes were almost uniform. Moreover, with the exception of the steep transition between the cluster and the bouncing aggregate, the evolution of the velocity PDF is continuous when density increases.

The detection of regime III is done by a two-sample Kolmogorov-Smirnov (KS) test [24] with a significance level $\alpha = 0.01$. The KS test compares the cumulative distribution function (CDF) of a uniform distribution with the CDF of the particles distribution along the z axis. The null hypothesis (H_0) of the test is the assumption that the observed distribution is uniform, hence, that the system is gaseous. The alternative hypothesis is noted (H_1). We define the parameter D as the following:

$$D = \sup_{|z| \leqslant L/2} \|F(z) - U(z)\|, \qquad (4)$$

where $F(z)$ is the observed CDF of the particle distribution along z axis and $U(z)$ the theoretical uniform distribution. The KS test value is defined by $T_z = D\sqrt{n/2}$, where n is the number of classes. H_0 is rejected at level α if $T_z > K_\alpha$. The statistical threshold K_α can be found in tables. Regime II displays a strong heterogeneity in the xy plane; therefore, its detection relies on a two-sample KS test between the particle distribution along the x and y axes with a significance level $\alpha = 0.01$. The test is denoted by T_{xy}. Finally, regime IV is detected by analyzing frequency fluctuations in the center of the box. If the central part of the box has a density at least 2 times lower than the one corresponding to a uniform distribution, the system is evolving like an inelastic body bouncing between two oscillating plates. Figure 4 describes the cluster detection in the studied system for a fixed dimensionless radius $r = 0.0175$ and for increasing density η. The first four graphics represent the PDF of the positions along the x, y, and z axes at specific (r, η) values illustrating the four regimes. The lower graph describes the evolution of T_z and T_{xy} compared to the statistical threshold K_α and the evolution of the central class frequency as a function of η. Density zones corresponding to the different regimes are separated by red vertical lines. One can see that both PDF and evolution of the KS test are in good agreement with the behavior of the system described in Fig. 3: four dynamical regimes are found when η increases.

Using the above statistical method for detecting the cluster, different transition points could be numerically obtained by selecting a ratio r and by scanning the granular behavior for various η values. The (r, η)-phase diagram, illustrated in Fig. 5, shows the dynamical regimes from I to IV. Transition curves are drawn and described below. It should be emphasized that those curves meet on triple points. Earlier studies [3] considered that the cluster may be expected once there is initially more than a single layer of particles in the system. In this configuration particle-particle collisions become frequent events that encourage dissipation and, thus, cluster formation. In our phase diagram, isolayer curves correspond to straight lines with the equation

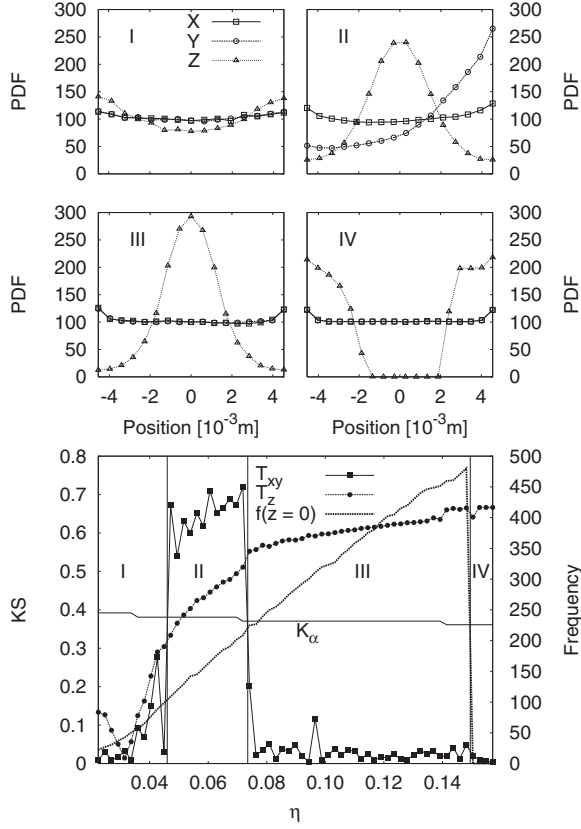$$r = \frac{\eta}{2\eta_e N_\ell}, \qquad (5)$$

FIG. 4. Detection of different dynamic regimes with a two-sample Kolmogorov-Smirnov test of level 0.01. (Top four graphs) PDF of the positions of the particles where the square, circle, and triangle denote, respectively, the distribution along the x, y, and z axes. (Bottom graph) The KS tests T_z and T_{xy} as well as $f(z=0)$, the frequency of the central class along the z axis as a function of the density η when $r = 0.0175$.

where η_e is determinate by using Falcon's data and N_ℓ is the number of granular layers. The gas-cluster frontier ($\bigcirc$) is better described by the empirical law

$$r_{\max} - r = \beta \left(\frac{1 - \eta}{\eta} \right), \tag{6}$$

where $\beta \approx 6.88 \times 10^{-4}$ is a constant. Equation (6) supports two arguments: (i) There is a critical dimensionless radius $r_{\max} \approx 0.032$ above which no cluster appears and (ii) the ratio between free volume and occupied volume is a relevant parameter. It should be noted that this ratio is also relevant for describing the mean free path in our system. One can say that, globally, two physical ingredients are necessary to describe the gas-cluster transition: confinement (since a maximum radius exists) and inelastic collisions (since the mean free path is relevant).

The transition curve between partial and complete clustering is rather complex. One should note that partial clustering is present only for small particles.
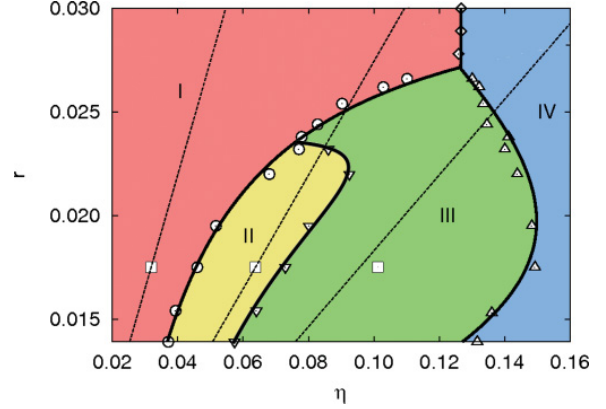
FIG. 5. (Color online) Phase diagram (r, η) distinguishing four different dynamical regimes described in the text. Symbols $(\bigcirc, \nabla, \triangle, \diamond)$ represent the transition points detected in our simulations. The squares correspond to the parameters of Falcon's *et al.* Mini-Texus 5 experiments [3]. Dashed lines correspond to conditions with a constant numbers of layers.

The bouncing aggregate regime (IV) appears for large packing fractions. Large particles condense without clustering. The frontier between gaseous and condensed states ($\diamond$) is a vertical line of equation $\eta = 0.127$. Considering the whole granular assembly as a single inelastic body, this critical value can be established theoretically by adapting the latest results concerning the Fermi-Box problem [25]. A point mass is confined in a box of height h which follows a sinusoidal motion of amplitude A. For a restitution coefficient $\varepsilon = 0$, it is shown that the dynamics switch from a monoperiodical motion (similar to the diluted gaseous state) to a regime presenting sticking phenomena (similar to the condensed state) once the critical height $h/A = \pi$ is reached. In our case, the size of the particles cannot be neglected; therefore, the Fermi-Box condition becomes

$$\frac{L - \left(\frac{L\eta^*}{\eta_{rlp}} \right)}{A} = \pi, \tag{7}$$

where the random loose packing fraction $\eta_{rlp} = 0.59$ can be used [26,27]. The value $\eta^* \approx 0.127$ is obtained and is in excellent agreement with our numerical simulations.

For smaller particles, the transition between cluster and bouncing aggregate is also triggered when η increases. We have noted that the cluster-aggregate frontier ($\triangle$) corresponds roughly to the relationship $r \sim \log N$ which consists of a Lambert-W function provided by the inversion of

$$\eta \sim \frac{4\pi}{3} r^3 \exp r. \tag{8}$$

This transition curve needs deeper investigations since different bouncing modes (like period doubling) can be observed in some cases. This is left for future studies.

IV. CONCLUSION AND PERSPECTIVES

In summary, the phase diagram is richer than expected since we have found four different dynamic regimes instead of

gas/cluster regimes. Moreover, the transition curves cannot be described by simple rules or arguments, except for the behavior of large grains. Small variations of A and ω parameters will slightly modify the diagram but the phases and the transitions will be qualitatively recovered. Our results raise fundamental questions and open new perspectives in particular for future experiments in microgravity planned for the International Space Station.

[1] S. McNamara and W. R. Young, Phys. Rev. E **50**, 1 (1994).
[2] A. Kudrolli, M. Wolpert, and J. P. Gollub, Phys. Rev. Lett. **78**, 1383 (1997).
[3] E. Falcon, R. Wunenburger, P. Evesque, S. Fauve, C. Chabot, Y. Garrabos, and D. Beysens, Phys. Rev. Lett. **83**, 440 (1999).
[4] H. M. Jaeger, C. Liu, and S. R. Nagel, Phys. Rev. Lett. **62**, 40 (1989).
[5] G. Lumay and N. Vandewalle, Phys. Rev. Lett. **95**, 028002 (2005).
[6] F. Ludewig, S. Dorbolo, T. Gilet, and N. Vandewalle, Eur. Phys. Lett. **84**, 44001 (2008).
[7] P. A. Thomson and G. S. Grest, Phys. Rev. Lett. **67**, 1751 (1991).
[8] I. Goldhirsch, Annu. Rev. Fluid Mech. **35**, 267 (2003).
[9] G. D. R. Midi, Eur. Phys. J. E. **14**, 341 (2004).
[10] P. deGennes, Rev. Mod. Phys. **71**, 374 (1999).
[11] E. Falcon, S. Fauve, and C. Laroche, in *Granular Gases*, Lecture Notes in Physics, Vol. 564, edited by S. Luding and T. Poschel (Springer-Verlag, Berlin, 2000), pp. 182–191.
[12] P. Eshuis, K. van der Weele, D. van der Meer, and D. Lohse, Phys. Rev. Lett. **95**, 258001 (2005).
[13] E. Falcon, S. Fauve, and C. Laroche, Eur. Phys. J. B **9**, 183 (1999).

[14] S. E. Episov and T. Poeschel, J. Stat. Phys. **86**, 1385 (1997).
[15] P. Eshuis, K. van der Weele, D. van der Meer, R. Bos, and D. Lohse, Phys. Fluids **19**, 123301 (2007).
[16] F. Ludewig, Ph.D. thesis, University of Liège, 2007.
[17] P. A. Cundall and O. D. L. Stark, Geotechnique **29**, 47 (1979).
[18] S. McNamara and E. Falcon, Phys. Rev. E **71**, 031302 (2005).
[19] S. Miller and S. Luding, Phys. Rev. E **69**, 031305 (2004).
[20] N. Taberlet, Ph.D. thesis, Université de Rennes I, 2005.
[21] M. Hou, R. Liu, G. Zhai, Z. Sun, K. Lu, Y. Garrabos, and P. Evesque, Microgravity Sci. Technol. **20**, 73 (2008).
[22] J. J. Brey and M. J. Ruiz-Montero, Phys. Rev. E **67**, 021307 (2003).
[23] T. Gilet, N. Vandewalle, and S. Dorbolo, Phys. Rev. E **79**, 055201 (2009).
[24] W. T. Eadie, D. Drijard, F. E. James, M. Roos, and B. Sadoulet, in *Statistical Methods in Experimental Physics* (North-Holland, Amsterdam, 1971), pp. 269–271.
[25] N. Vandewalle, T. Gillet, and S. Dorbolo (in press).
[26] G. Lumay and N. Vandewalle, New J. Phys. **9**, 406 (2007).
[27] K. J. Dong, R. Y. Yang, R. P. Zou, and A. B. Yu, Phys. Rev. Lett. **96**, 145505 (2006).

3.7 Complementary measures

The following study is an extension of our work concerning the reproduction of Falcon's experiments. In addition to our first simulations, we investigated the influence of the driving parameters on the system's dynamics and on the transitions from one regime to another. Both the amplitude A and the frequency f were modified so that three new phase diagrams could be obtained. We showed that the varying f does not change the aspect of the phase diagram. Indeed, f only fixes the time scale for which the phenomenon takes place. On the other hand modifying A has a large impact on the dynamics. Our simulations with a smaller amplitude present only two of the initial four regimes for identical filling fractions. However, the appearance of a dynamical cluster for such small amplitudes is not trivial and can't be explained only by a geometrical confinement.

A last measure consisted in the realization of an energy mapping of the system as a function of the packing fraction[2] ϕ and the normalized particle size r. Indeed, for a system with amplitude $A = 2.5$ mm and frequency $f = 30$ Hz, we measured the mean kinematic energy K in the system for all simulated couples (r, ϕ). As presented in figure 3.4, three particular energetic signatures can be observed: low energy for small r and intermediate fillings, medium energy for dilute systems of large particles and high energy for dense systems. If one places the transitions from figure 3.3 (here in purple) onto the same graphic, it is obvious that each observed dynamical regime (gas,cluster,bouncing aggregate) corresponds to a particular level of energy. Note that the high energy level of the bouncing aggregate is corroborated by Sack *et al.* who identified it as the regime of most efficient damping in their study [83] .
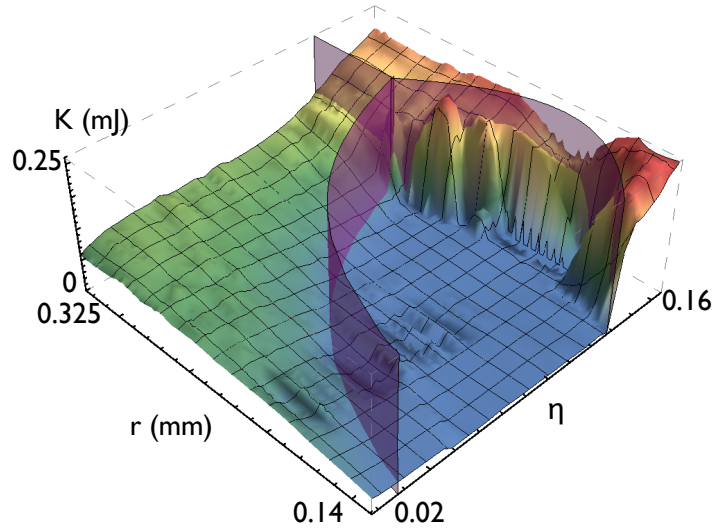
Figure 3.4: (Taken from [86]) Energy mapping of the system as a function of the filling fraction and the particle size. For a system with amplitude $A = 2.5$ mm and frequency $f = 30$ Hz, we measured the mean kinematic energy K in the system for all simulated couples (r, ϕ). One can note that the different dynamical regimes present particular energy levels. Transition lines corresponding to figure 3.3 are given in purple.

---

[2]In the articles [79, 86] the symbol η was used instead of ϕ for the denomination of the packing fraction.

Dynamical Regimes of a Granular Gas in Microgravity : a Molecular Dynamics Study

E. Opsomer, F. Ludewig and N. Vandewalle

GRASP Université de Liège, Allée du 6 Aôut, B-4000 Liège

E-mail: `eric.oposmer@doct.ulg.ac.be`

Abstract. We propose a numerical model, based on molecular dynamics, which is able to reproduce the behavior of a dissipative granular gas in microgravity. Granular material is confined in a cubic box of side length L following a sinusoidal motion of amplitude A and angular velocity $\omega = 2\pi f$ along the z-axis. The simulations are performed using the parameters of earlier Texus experiments [15]. Our results are in excellent agreement with experimental data. Moreover, we discovered various dynamical regimes and the physical conditions for their appearance : a gaseous state, the formation of either small or large clusters, the collective motion of grains. Phase diagrams are drawn where transitions between these different granular states are emphasized. Transitions are discussed by considering Statistical Physics models.

1. Introduction

The intriguing behaviors of grains and powders fascinate scientists since the nineteenth century. Properties like Reynolds dilatancy [1], Brazil Nut effect [2, 3], heterogenous force networks [4, 5] and clustering [6, 15] have been discovered. Nowadays, granular material like coal, sand and even powders are part of all economic activity such as agriculture, construction, cosmetics and aerospace research.

Different granular states could be encountered. Solid and liquid states have been deeply investigated during the last decades by studying granular compaction [7, 8, 9] and granular flows [10, 11]. A great number of models were suggested but could not give complete answers to all fundamental questions [12]. Among all phases, gaseous are the most complex. The dissipative character of the collisions implies a constant external energy supply and microgravity to subsist. Indeed, experimentation with granular material requires parabolic flights, sounding rockets, drop tower experiments or ISS missions that are bound to high costs and long preparation times. Nevertheless, these micro-gravity studies are of an capital interest in order to prepare longtime space missions, to study the impact of asteroids [13] or to understand the dynamics of planetary rings [14].

Pioneer work has been done by Falcon *et al.* during Mini-Texus 5 experimentation [15, 16]. Clustering has been reported and refers to particles mostly remaining in the center of the box, forming a denser region in the system. Incoming particles are trapped in the cluster, while other particles leave the dense region. Different mechanisms like inelastic collapse [17] have been proposed to explain the clustering phenomenon. A criterion for the appearance of the cluster has been proposed, based on experimental observation. It is related to the number of grain layers inside the box. Low densitiy granular gases have been investigated by Evesque [18].

Local measures of granular pressure and granular temperature as well as exponential velocity distributions were reported. Numerical simulations have been realized and sustain experimental results.

However, the behavior of granular gases, especially for extreme densities, is still not well understood. Given the great number of parameters, too few experiments have been realized and nowadays no model is able to describe completely the behavior of this material. A lot of fundamental research will be needed to illuminate the remaining questions.

2. Model

In opposition to classical Event Driven algorithm (ED) [17, 19] for which inelastic collapse is avoided by a time cutoff model [20], we are using a three-dimensional model based on Molecular Dynamics (MD) [21, 22]. A cubic container of side length L, following a sinusoidal motion of amplitude A and angular velocity $\omega = 2\pi f$ along the z-axis, is filled with N spherical particles of mass m and a radius r. At initialization, each one is given a different random position (that allows no contact between the particle and the rest of the system). Moreover, their initial linear and angular velocities are null. Contact forces are computed following two simple models.

Normal forces F_{ij}^n are composed by a repulsive (F_{ij}^{rep}) and a dissipative (F_{ij}^{dis}) component. The repulsive component follows a simple Hooke's Law

$$F_{ij}^{rep} = -k_n \delta_{ij} \tag{1}$$

where $\delta_{ij} = d_{ij} - 2r$ with d_{ij} the distance between the centers of the solids i and j. The constant k_n is the normal stiffness which is a purely numerical parameter. Indeed, this stiffness is not linked to specific physical properties of the simulated material. It's value is calculated in order to keep the static deformation of the particles lower than $10^{-4}r$. (In our simulations k_n ranges typically between 100 and 1000 kg/s^2). The dissipative component is taken into account by viscous forces according to the following law

$$F_{ij}^{dis} = -\gamma_n(k_n, \varepsilon) \frac{\partial \delta_{ij}}{\partial t} \tag{2}$$

where the viscous constant γ_n is a non-trivial function of the normal stiffness k_n and the restitution coefficient ε. This restitution coefficient is used for both, grain-grain and grain-wall collisions. In opposite to other models (like Hertz' model) using a Hooke's Law and viscous dissipation allows us to work with a constant contact duration Δt, independent on the impact velocities. In order to assure the integration of the forces, each contact should be resolved in about 100 time steps τ (i.e. $\tau \approx \Delta t / 100$).

Tangent forces F_{ij}^t are bounded and depend on the relative tangent velocities v_{ij}^t between the colliding solids i and j. One has

$$F_{ij}^t = -k_t v_{ij}^t \quad \text{and} \quad \|F_{ij}^t\| \leq \mu F_{ij}^n \tag{3}$$

where μ is a friction coefficient and k_t a purely numerical constant. Friction coefficient μ as wall as restitution coefficient ε can be adapted to fit the intrinsic properties of the system. A complete description of MD simulations is given by Taberlet [23].

3. Results

In our simulations, we reproduced the results of Falcon *et al* [15]. Three cubic cells of side length $L = 10$ mm are filled with bronze spheres of radius $r = 0.175$ mm. The system is oscillating with an amplitude $A = 2.5$ mm and a frequency $f = 30$ Hz. According to the materials properties, friction coefficient is set to $\mu = 0.2$, restitution coefficient to $\varepsilon = 0.9$ and volume density to $\rho = 8 \ 10^3$ kg/m^3. Figure 1 presents simulations and experiments of the system with $N = 1420$, 2840 and 4510 particles at its maximum downward velocity $-A\omega$. Dense regions are observed thanks to shading effects [15].
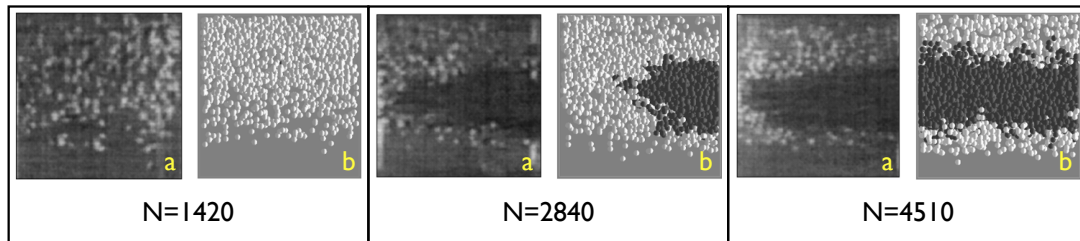
Figure 1. (a) The experimental results for respectively N=1420, 2840 and 4510 particles at the box maximum downward velocity [15]. (b) Numerical results in the same conditions. Shading of the cluster is realized by a proximity rule described in the text.

The right three pictures (b) correspond to our simulations where dense regions are blackened according to a simple proximity rule : (i) Two particles are neighbors if the distance between them is less than $2.5r$. (ii) Particles that are close enough to the system's center of mass are forming a seed. (iii) Step by step, the seed is extended by its neighbors. (iv) At saturation, the cluster is colored in black (see Figure 1). Simulations are in a qualitative agreement to Falcon's experiment presented in pictures (a). Indeed, the less dense system ($N = 1420$) of Figure 1 stays in a gaseous state and presents a density gradient decreasing towards the center of the box. For the densest case ($N = 4510$) clustering is observed around the center of the box. Moreover, the distribution is homogeneous over the xy-plane. Finally, the intermediate case ($N = 2840$) presents a new phenomenon : the cluster does not occupy the entire xy-plane. That behavior was not addressed in Falcon's experiment but can be seen on their pictures.

After the reproduction of the Texus experiments and the detection of partial clustering, the second step was to modify the different parameters. We decided to investigate the behavior of a system with a large number of grains. At this point, the densest system ($N = 4510$) had only a global density of $\eta = 0.11$. By progressively increasing the number of grains up to $N = 6800$ ($\eta \approx 0.15$) a fourth state has been found. Particles stay gathered and present a coherent motion with a velocity close to $\pm A\omega$. Figure 2 describes the different dynamical regimes of a system with respectively $N = 1420, 2840, 4510$ and 6800 grains at its maximum downwards velocity $-A\omega$. Different colors correspond to selected ranges of the vertical velocity : blue if $|v_z| < A\omega$, green if $A\omega \leq |v_z| < 2A\omega$ and orange if $2A\omega \leq |v_z|$.
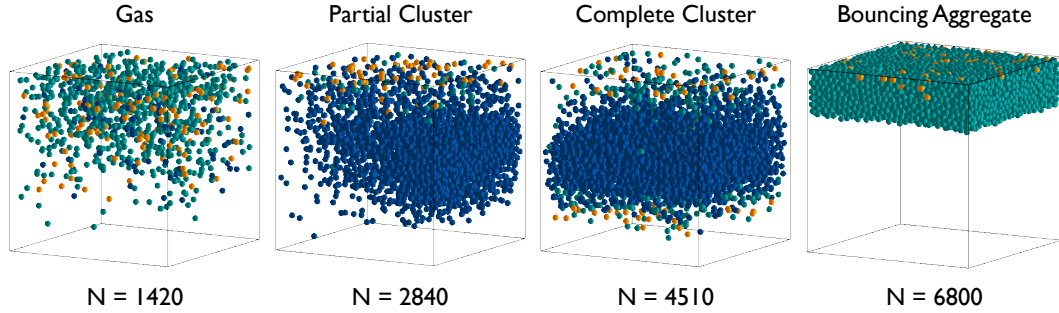
Figure 2. By increasing the grain number N, one can observe four different dynamical regimes: a gaseous phase, partial and complete clustering and an aggregate phase. Color stand for different velocity ranges: Blue for subsonic grains, green for velocities between one and two times the maximum velocity of the box and orange for even higher velocities.

Each dynamical regime is discussed in the following and introduced by two figures. On the left, the Probability Density Function (PDF) of particle positions, along the three axis, collected at the systems maximum velocities $\pm A\omega$. On the right, the PDF of U, the vertical velocities of the particles normalized by $A\omega$. Data is collected at the systems maximum downward velocity $-A\omega$.

3.1. Gas state

Figure 3. (Left) PDF of particle positions in the system collected every half period. (Right) Semi-log PDF plot of particle velocities in the gaseous state.

The gaseous state is found in dilute systems, the grains exhibit a broad and asymmetric distribution of vertical velocities v_z as shown in Figure 3. This asymmetry evolves according to the phase oscillation of the box. Particles can be found everywhere in the system, but follow a density gradient decreasing from one wall towards the center of the box, as shown in Figure 2 and 3. According to earlier experimentations [24, 25], we found v_x and v_y distributions of the form $P_\lambda^\gamma(v) = \lambda \exp\left(-|\lambda v|^\gamma\right), \gamma \in \{1, 2\}$ and λ as fitting parameter. Note that $\lambda \approx \frac{1}{v_0}$, where v_0 is the mean velocity. A γ value is preferred to another depending on the velocity range in the system.

3.2. Partial Cluster

Figure 4. (Left) PDF of particle positions in the system collected every half period. (Right) Semi-log PDF plot of particle velocities in the a partial cluster.

When the number of grains increases, the system could present a partial clustering. Particles are more or less stabilized around the origin of the z-axis but stay gathered along a wall of the box. One could assumed that the system needs a typical cluster width to be energetically stable. In the distribution of velocities along z (Figure 4), a sharp peak appears around zero which is a signature for clustering. However, the distribution exhibits a broad foot since a gaseous regime coexists in the system. Multiple simulations have shown that a cluster can appear on a particular lateral wall with a probability 1/4. Moreover, simulations in a cylinder with identical volume and base section revealed that the lateral clustering is not related to corner effects. The reason of this phenomenon is yet not well understood

3.3. Complete Cluster

Figure 5. (Left) PDF of particle positions in the system collected every half period. (Right) Semi-log PDF plot of particle velocities in the a complete cluster.

When the density further increases, we observe that the cluster spreads over the entire xy plane. A peaked velocity distribution around zero can be observed in Figure 5. The presence of two sharp peaks at $v_z = \pm 2A\omega$ (also seen for partial clustering) is due to the granular gas trapped in between the cluster and the vibrating walls. We assist to an equilibrium between condensation and evaporation of the cluster. By tracking particles and analyzing the dynamics of clusterisation during several periods, we can conclude that the cluster is in a dynamical state with a constant renewal. Indeed, high speed particles arriving from the walls crush into the cluster, dissipate their energy and eventually become part of the cluster. The energy partially

transmitted across the cluster provokes internal rearrangements and eventually ejects particles. It should be noted that the packing fraction measured inside the cluster is about $\eta = 0.30$ which is far below the jamming limit.
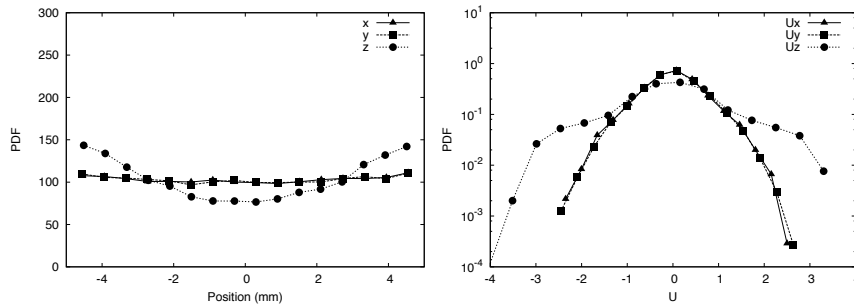
3.4. Bouncing aggregate

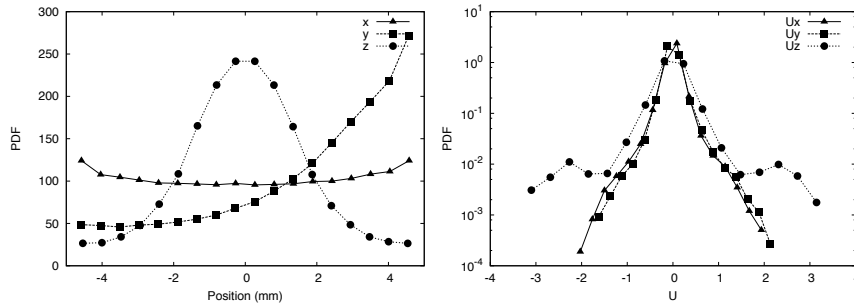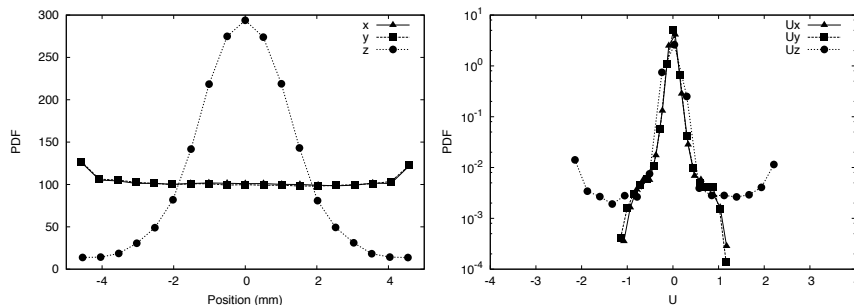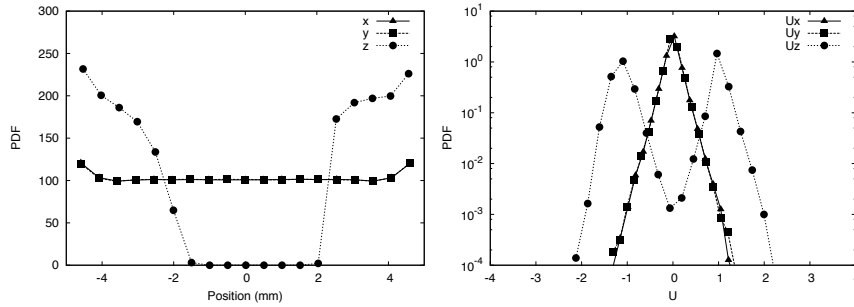**Figure 6.** (Left) PDF of particle positions in the system collected every half period. (Right) Semi-log PDF plot of particle velocities in a bouncing aggregate.

For denser systems a new phenomenon is observed. The important amount of granular material confined in the system leads to higher kinetic energy than in other regimes (see figure 9). This energy cannot only be dissipated through successive collisions like in a cluster. Indeed, the local density in the system's center is high enough to assure permanent contacts between many particles, when the gaseous phase encounters this denser region all the grains a dragged towards the wall. This bouncing state is characterized by a coherent motion of all particles and peaked velocity distribution around $\pm A\omega$. Particles stay gathered in a dense arrangement which describes a movement similar to a totally dissipative bouncing ball [26]. Moreover, density distribution along the z-axis revealed crystal-like structures inside the packing. Layers are observed along the three axes.

4. Discussion
4.1. Phase Diagrams
An automated and reliable detection of the different dynamical regimes can be done by statistical means. The complete cluster detection relies a two-sample Kolmogorov-Smirnov (KS) test [27] with a significance level $\alpha = 0.01$. The KS test compares the cumulative distribution function (CDF) of a uniform distribution with the CDF of the particles distribution along z axis. The null hypothesis (H_0) of the test is the assumption that the observed distribution is uniform, hence that the system is gaseous. The alternative hypothesis is noted (H_1). We define the parameter D as the following

$$D = \sup_{|z| \leq L/2} \|F(z) - U(z)\| \tag{4}$$

where $F(z)$ is the observed CDF of the particles distribution along z-axis and $U(z)$ the theoretical uniform distribution. The KS test value is defined by $T_z = D\sqrt{n/2}$ where n is the number of classes. H_0 is rejected at level α if $T_z > K_\alpha$. The statistical threshold K_α can be found in tables. In a partial cluster regime, the system displays a strong heterogeneity in the xy-plane, therefore its detection relies on a two-sample KS test between the particles distribution along the x and y-axes with a significance level $\alpha = 0.01$. The test is denoted by T_{xy}. Finally, bouncing regime is detected by analyzing frequency fluctuations in the center of the box. If the central part of the

box has a density at least two times lower than the one corresponding to a uniform distribution, the system is evolving like an inelastic body bouncing between two oscillating plates. A large number of MD simulations allowed us to obtain four typical (η, r) phase diagrams that are shown in figure 7.
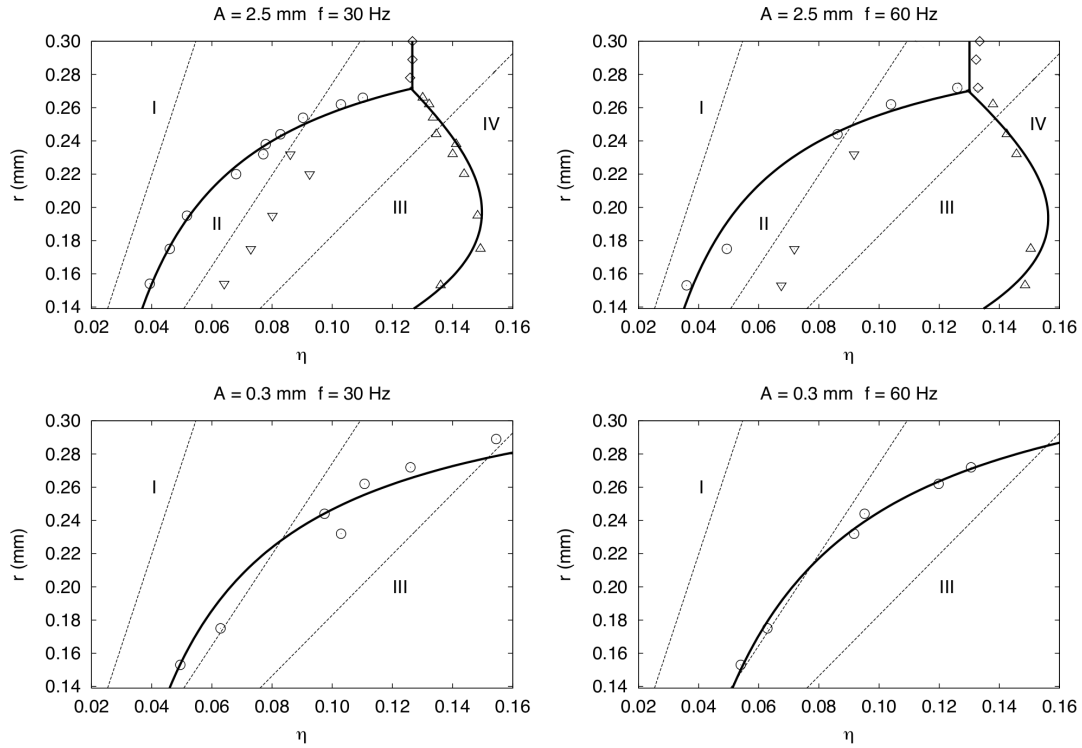
Figure 7. Simulated (r,η) phase diagrams for two different amplitudes $A = 2.5$ mm and $A = 0.3$ mm and for two different frequencies $f = 30$ Hz and $f = 60$ Hz. Curves correspond to the transitions from one dynamical regime to another. Differnt phases are denoted by numbers from I to IV.

For high amplitude ($A = 2.5$ mm), the four dynamical regimes can be observed and are denoted on figure 7 (I gas, II partial cluster, III complete cluster and IV aggregate). For low amplitude ($A = 0.3$ mm), only the gas and the complete cluster state is observed. Parameters such as η, r and A seem to have a deep impact on the systems dynamics in opposite to ω whose fluctuations have only minor effects. The emergence of a cluster for low amplitude is not trivial. While the formation of a high density zone in the case of $A = L/4 = 2.5$ mm could be triggered by geometrical reasons and confinement, the appearance of such a dynamical regime for $A = 0.3$ mm requires the presence of additional phenomena such as inelastic collapse. Moreover, measuring the standard deviation σ of the position PDF along the z-axis for 2 simulations with $N = 5000$, $r = 0.175$ mm and respectively $A = 2.5$ mm and $A = 0.3$ mm shows us that the difference of the cluster width is negligible compared to the difference of amplitude. Collecting data every period, we found in the first case $\sigma_{2.5} = 1.51$ mm and in the second $\sigma_{0.3} = 1.72$ mm. Figure 8 shows the position PDF along z-axis for both simulations. Shaded zones refer to the volume visited by the box' walls during oscillation.
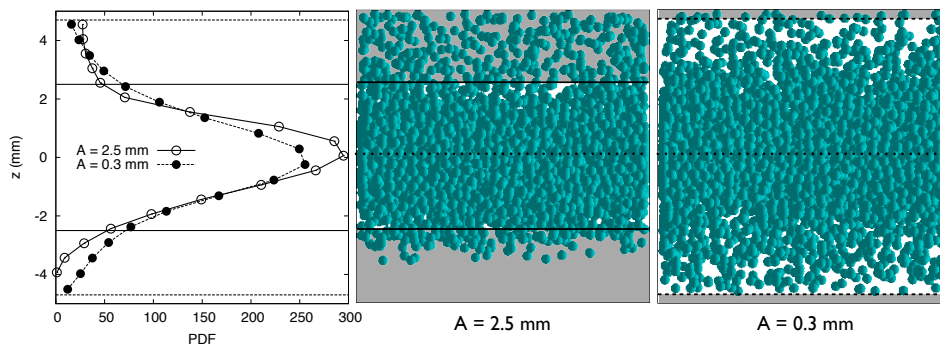
Figure 8. (Left) Distribution of the particle positions along z-axis for 2 simulations with $N = 5000$, $r = 0.175$ mm and respectively $A = 2.5$ mm and $A = 0.3$ mm. Data is collected every period. (Center) Lateral view of the system with an amplitude of $A = 2.5$ mm. (Right) Lateral view of the system with an amplitude of $A = 0.3$ mm. Shaded zones refer to the volume visited by the box' walls during oscillation.

4.2. Transition lines

For large amplitudes, the (r, η)-phase diagrams, illustrated in the first row of Figure 7, exhibit all the dynamical regimes. Different regimes are separated by transition curves that meet on triple points. Earlier studies [15] considered that cluster may be expected once there is initially more than a single layer of particles in the system. In this configuration, particle-particle collisions become frequent events which encourages dissipation and thus cluster formation. In our phase diagram, iso-layer curves correspond to dashed straight lines with an angular coefficient proportional to the inverse number of granular layers. The layer criterion clearly misses the transition from a gas to a (partial) cluster. The ($\bigcirc$)frontier is better described by the empirical law

$$r_{clust} - r = \delta_{clust} \left(\frac{1 - \eta}{\eta} \right) \qquad (5)$$

where δ_{clust} and r_{clust} are constants. Eq. (5) supports two arguments : (i) a critical size $r_{clust} \approx 0.32$ mm for the grains above which no cluster appears, and (ii) the ratio between free volume and occupied volume becomes a relevant parameter. It should be noted that this ratio is also relevant for describing mean free path in our system.

The transition between partial and complete clustering is rather complex. One should note that partial clustering is only present for small particles and large amplitudes and. Moreover, it needs a long formation time (about 100 periods).

The bouncing aggregate regime IV appears for large packing fractions. Large particles condensate without clustering. The $\Diamond$-frontier between gaseous and condensed states is a vertical line of equation $\eta = 0.127$. Considering the whole granular assembly as a single inelastic body, this critical value can be established theoretically by adapting latest results concerning the Fermi-Box problem [28]. A punctual body is confined in a box of height H which follows a sinusoidal motion of amplitude A. For a restitution coefficient $\varepsilon = 0$, it is shown that the dynamics switch from a mono-periodical motion (similar to the diluted gaseous state) to a regime presenting sticking phenomena (similar to the condensed state) once the critical height $h = (H/A) = \pi$

is reached. In our case, the size of the particles cannot be neglected, therefore the Fermi-Box condition becomes

$$\frac{L - \left(\dfrac{L\eta^*}{\eta_{rlp}}\right)}{A} = \pi \tag{6}$$

where the random loose packing fraction $\eta_{rlp} \approx 0.59$. The critical value $\eta^* \approx 0.127$ is obtained in an excellent agreement with our numerical simulations.

For smaller particles, the transition between cluster and bouncing aggregate is also triggered when η increases. We have noted that the $\triangle$-frontier corresponds roughly to the relationship $r/L \sim \log N$ which consists in a Lambert-W function [29] provided by the inversion of (7).

$$\eta = \frac{4\pi}{3} \left(\frac{r}{L}\right)^3 \exp \frac{r_{ba} - r}{\delta_{ba}} \tag{7}$$

This transition curve needs deeper investigations since different bouncing modes (like period doubling) can be observed in some cases. This is left for future works.

The different values of the free fitting parameters for the various transition curves are given in table 1. In opposite to the small impact of the frequency, we can see that the variations are important when the amplitude changes.

A (mm)	f (Hz)	δ_{clust} (mm)	r_{clust} (mm)	δ_{ba} (mm)	r_{ba} (mm)
2.5	30	$6.8817 \ 10^{-3}$	0.31908	$6.5718 \ 10^{-2}$	0.75250
2.5	60	$6.3164 \ 10^{-3}$	0.31239	$6.4548 \ 10^{-2}$	0.74515
0.3	30	$9.2490 \ 10^{-3}$	0.33101	-	-
0.3	60	$1.1143 \ 10^{-2}$	0.34529	-	-

Table 1. Values of the free fitting parameters for the various transition curves in four diagrams

4.3. 3D Phase Diagram

In order to understand the origin of the cluster phenomenon, the internal energy of the system with amplitude $A = 2.5$ mm and $f = 30$ Hz has been investigated. By collecting the translation and the rotation velocities of the particles during one period, a three dimensional graph representing the mean kinematic energy in the system as a function of the packing fraction η and the grain radius r has been obtained. As shown in figure 9, the surface is colored by a color gradient and displays different energetic levels according to the dynamical regimes we determinate by statistical means. The corresponding transition lines shown in the previous figures are denoted by purple vertical surfaces.
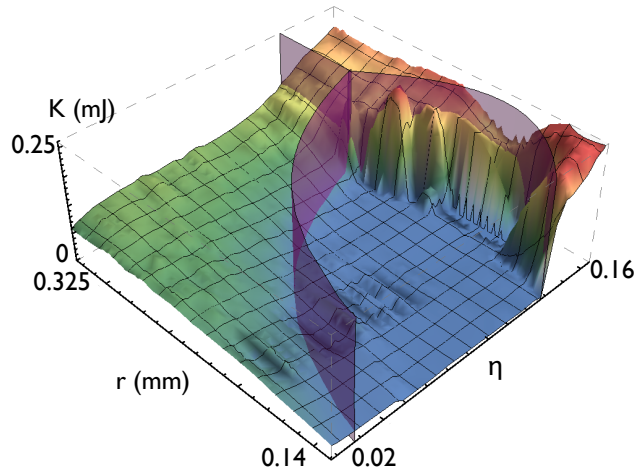
Figure 9. 3D view of the mean kinematic energy in the system with an amplitude $A = 2.5$ mm and frequency $f = 30$ Hz as a function of grain size r and packing fraction η. The corresponding transition lines shown in the previous figures are denoted by purple vertical surfaces.

5. Conclusion and Perspectives

In summary, the phase diagram is richer than expected since we have found four different dynamical regimes instead of gas/cluster regimes. Moreover, the transition curves cannot be described by simple rules or arguments, except for the behavior of large grains. Small variation of A and ω parameters will quantitatively modify the diagram but the phases and the transitions will be qualitatively recovered. We can assure that the diagram is locally stable. Our results raise fundamental questions and opens new perspectives in particular for future experiments in microgravity planned on the International Space Station.

In order to collect new relevant data, ESA is setting up "VIP-Gran", a series of experimentation expected to join the ISS in a closer future. In the experiment a certain amount of granular material is trapped in a cell volume of 30x30x70 mm between two independent oscillating walls. The main diagnostic tool is a CCD camera. Effects of the global packing fraction on the systems dynamics will be studied with a special interest in very dense systems and systems in a Knudsen regime. Different grain sizes as well as different shapes for the box will be tested. Moreover, experimentation with granular mixtures are planned. The following work has been realized in order to accomplish a first step for the calibration of VIP-Gran. Effects of parameters as grain size and packing fraction have been investigated and a granular phase diagram has been obtained.

6. Acknowledgments

References

[1] O. Reynolds, Phil. Mag. Ser. **50**, 20 (1885)

[2] A. Kudrolli, Rep. Prog. Phys. **67**, 209 (2004)

[3] F. Ludewig and N. Vandewalle, Eur. Phys. J. E **18**, 367 (2005)

[4] D. Howell and R.P. Behringer, Phys. Rev. Lett. **82**, 5241 (1999)

[5] T.S. Majmudar and R.P. Behringer, Nature **435**, 1079 (2005)

[6] A. Kudrolli, M. Wollpert, J.P. Gollub, Phys. Rev. Lett. **78**, 1383 (1997)

[7] G. Lumay and N. Vandewalle, Phys. Rev. Lett. **95**, 028002 (2005)

[8] G. Lumay and N. Vandewalle, Phys. Rev. E. **74**, 021301 (2006)

[9] F. Ludewig, S. Dorbolo, T. Gilet and N. Vandewalle, Eur. Phys. Lett. **84**, 44001 (2008)

[10] P. A. Thomson and G. S. Grest, Phys. Rev. Lett. **67**, 13 (1991)

[11] G. D. R. Midi, Eur. Phys. J. E. **14**, 341(2004)

[12] P. deGennes, Rev. Mod. Phys. **71**, 374 (1999)

[13] A. M. Walsh, K. E. Holloway, P. Habdas and J. R. de Bruyn, Phys. Rev. Lett. **91**, 10 (2003)

[14] F. Spahn, J. Schmidt and M. Sremcevic, Lect. Notes in Phys. **557**, pp 507(2000)

[15] E. Falcon, R. Wunenburger, P. Evesque, S. Fauve, C. Chabot, Y. Garrabos and D. Beysens, Phys. Rev. Lett. **83**, 2, 440 (1999)

[16] E. Falcon, S. Fauve and C. Laroche, Eur. Phys. J. B **9**, 183 (1999)

[17] S. McNamara and W.R. Young, Phys. Rev. E. **50**, 1 (1994)

[18] P. Evesque, Y. Garrabos, C. Lecoutre, F. Palencia, and D. Beysens, Powders and Grains 2005 **1** (2005)

[19] S. McNamara and E. Falcon, Phys. Rev. E. **71**, 031302 (2005)

[20] S. Miller and S. Luding, Phys. Rev. E. **69**, 031305 (2004)

[21] P. A. Cundall and O. D. L. Stark, Geotechnique **29**, 47 (1979)

[22] F. Ludewig, PhD Thesis, University of Liege (2007)
       (URL http://orbi.ulg.ac.be/handle/2268/70899)

[23] N. Taberlet, PhD Thesis, Université de Rennes I (2005)

[24] M. Hou, R. Liu, G. Zhai, Z. Sun, K. Lu, Y. Garrabos and P. Evesque, Microgravity Sci. Technol. **20**, 73 (2008)

[25] J. J. Brey and M. J. Ruiz-Montero, Phys. Rev. E. **67**, 021307 (2003)

[26] T. Gilet, N. Vandewalle and S. Dorbolo, Phys. Rev. E. **79**, 055201 (2009)

[27] W. T. Eadie, D. Drijard, F. E. James, M. Roos and B. Sadoulet, Statistical Methods in Experimental Physics, 2nd Edition (World Scientific, Amsterdam, 2006)

[28] N. Vandewalle, T. Gilet and S. Dorbolo (preprint 2010)

[29] S. R Valluri, D. J. Jeffrey and R. M. Corless, Canadian Journal of Physics **78**, 823 (2000)

3.8 A bouncing aggregate as a granular damper

In parallel to our simulations predicting the bouncing aggregate (a solid like behavior in driven granular systems), a scientific group from the Friedrich-Alexander University in Erlangen realized a series of experiments concerning the damping capacity of granular media.

In a first study [81,82], they attached a rectangular polycarbonate cell containing 37 steel balls on a flat spring. The initial position of the system was deflected by an amplitude A_0 and released so that a damped oscillation could be observed. The experiment was performed during a parabolic flight and the data collected via a high speed camera. An overview of the experimental setup is given in figure 3.5.
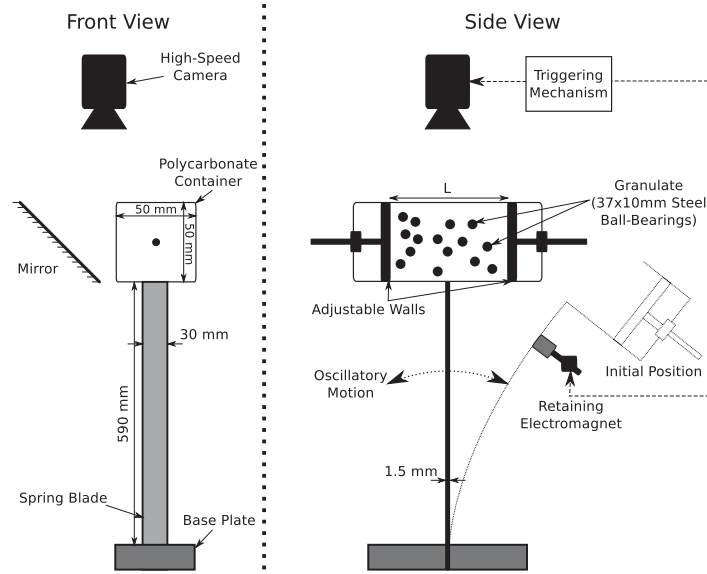
Figure 3.5: (Taken from [81]) Schematic view of the experimental setup of the granular damper used in the parabolic flights.

During the first seconds of the experiment, the amplitude of oscillation decays linearly until a critical value A_c is reached. From that moment, a much weaker decay is found. The reason for this change is the transition from a bouncing aggregate regime (called *collect-and-collide* regime in the experiment) to a gaseous regime. The upper row of figure 3.6 shows snapshots of the system for several amplitudes of oscillations. In the lower row the complete dynamics can be followed over a period of 5 seconds. The transition occurs after about 4 seconds.

In addition to the experimental observation of the bouncing regime, the theoretical developments concerning the transition from a granular gas to a *collect-and-collide* regime, presented in [82], is in perfect agreement with our predictions. Indeed, in our first article [79], comparing the aggregate to a complete inelastic particle led us to define the following vertical frontier between both regimes by

$$\phi^* = \phi_{rlp} \left(1 - \pi \frac{A}{L} \right). \tag{3.1}$$

where $\phi_{rlp} = 0.59$ is the packing fraction of a random loose packing. Rearranging the terms shows that this equation is equivalent to the relation found by Kollmer and his coworkers:

$$A_0 = L_g/\pi, \tag{3.2}$$

where A_0 is the threshold amplitude and L_g the difference between the box length and the thickness of the packed layer of particles in box.
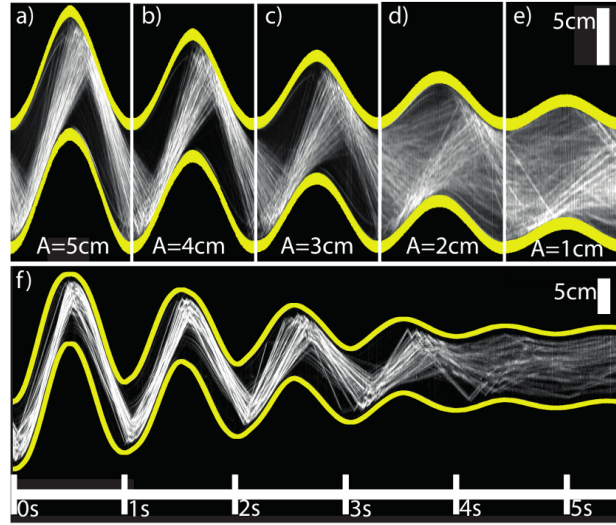
Figure 3.6: (Taken from [82]) Trajectories of the particles inside the oscillating cell. Below a critical amplitude A_c, the collective motion of the granular material vanishes and gaseous dynamics are observed. The transition leads to a modified damping of the system.

In another study [83], the energy dissipation rate in a driven granular gas was investigated in detail. It appears that both dynamical regimes (gas and bouncing aggregate) correspond to different dissipation mechanisms leading to different scaling with amplitude and frequency of the oscillation and with the mass of the grains. This time the cell is no longer fixed on a flat spring but mounted on a strain gauge that is attached to a carrier moving on a linear bearing. The system is driven by a computer controlled stepper motor according to a sinusoidal motion of amplitude A and frequency ω. Figure 3.7 gives a sketch of the experimental setup.
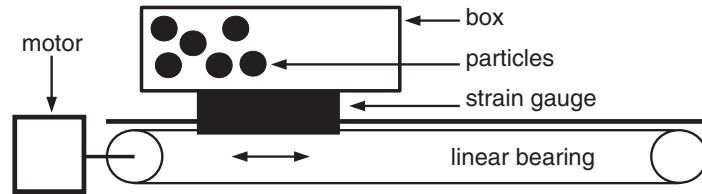
Figure 3.7: (Taken from [83]) Schematic view of the driving device. The cell's position is controlled via a computer controlled stepper motor according to a sinusoidal motion. A strain gauge allows the measurement of forces acting on the cell.

The energy that is dissipated by the granular media during one period of oscillation T can be obtained by integration. Indeed, one has

$$E_{diss} = \int_T \dot{x}(t)F(t)dt, \tag{3.3}$$

where $x(t) = A\sin(\omega t)$ is the position of the box and $F(t)$ is the force measured by the strain gauge. The maximum energy that can be dissipated in the system is given by

$$E_{max} = 4mA^2\omega^2, \tag{3.4}$$

with m being the total mass of the particles. Sack and his coworkers measured the ratio E_{diss}/E_{max} in four different samples. The latter were obtained by changing the number of grains as well as the

length of the box. Both parameters were tuned so that the samples 1 and 4 (respectively 2 and 3) presented approximatively the same clearance L_g. As shown in figure 3.8, different scaling is obtained on either side of the threshold amplitude A_0 presented in equation (3.2). The energetic jump at A_0 corresponds to the transition between the gas and the bouncing aggregate regime and can also be observed in our simulated energy landscape on figure 3.4.
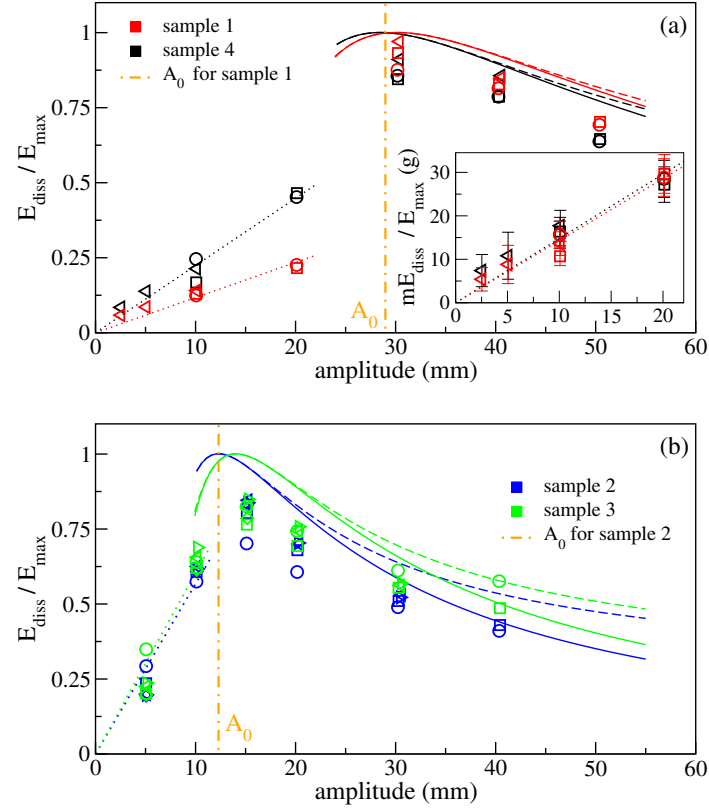
Figure 3.8: (Taken from [83]) Schematic view of the driving device. The cell's position is controlled via a computer controlled stepper motor according to a sinusoidal motion. A strain gauge allows the measurement of forces acting on the cell.

Chapter 4

Modeling the dynamical cluster

In classical thermodynamics, the simplest way to capture the behavior of a fluid is the concept of the ideal gas. This model considers a dilute system, without any particle interaction, in which the movements of the particles are dictated only by the temperature. Note that for very low pressure, most common gases can be considered as ideal gases. In general, one can qualify as ideal any gas that satisfies simultaneously the laws of Boyle-Mariotte, Avogadro, Gay-Lussac, Charles and Dalton. Accordingly, the behavior of an ideal gas can be described by the following equation of state,

$$PV = Nk_BT, \tag{4.1}$$

where N is the number of particles, T the temperature, P the pressure and V the volume of the system. The parameter k_B is the Boltzmann constant. In hard sphere models, that are closer to our system, additional parameters are considered in order to take account the interactions between particles and the excluded volumes. For instance, the Carnahan-Starling equation of state [87] is an approximate equation of state for the fluid phase of the hard sphere model in three dimensions. It is given by,

$$\frac{PV}{Nk_BT} = \frac{1 + \phi + \phi^2 - \phi^3}{(1-\phi)^3}, \quad \phi = N\frac{4}{3}\frac{\pi R^3}{V}; \tag{4.2}$$

R being the radius of the gas particles and ϕ the packing fraction of the system.

However, the case of the granular gas is even more complex since the system is dissipative. Indeed, at each collision, a small amount of energy is lost which will eventually result in an inhomogeneous distribution of the particles and in the formation of a cluster. This local condensation is not observable with a regular hard sphere model. Moreover, the system is out of equilibrium and requires a permanent energy supply in order to remain in a steady state. Finally, the granular gas is athermal, meaning that the temperature (as classically defined) has no influence on its dynamics. The following table summarizes the differences between both models.

Hard spheres	**vs.**	Granular gas
yes	**excluded volumes**	yes
yes	**equilibrium**	no
yes	**thermal system**	no
no	**dissipative system**	yes
P, V, T, ϕ	**parameters**	$\phi, \varepsilon, R, \delta$

The parameter δ is the typical length scale of the system and ε is the coefficient of restitution. During the past decades, several hydrodynamical models for (dense) granular fluids [88–91] have been proposed but none of them recovers the entire field of observable phenomena.

4.1   Motivations

Despite the lack of an equation of state for granular fluids, parameters such as the packing fraction ϕ, the dimensions of the system and the size R of the particles can provide enough information to predict roughly the dynamics of the system. In the following article (published in Europhysics Letters) we have shown that, based on simple arguments, it is possible to predict the transition from a gas like regime to a dynamical cluster in a granular fluid. Our model considers the balance between two antagonist processes in the system: on the one hand, the tendency to stir up the granular material by injecting energy and on the other hand, the tendency to cool it down via multiple dissipative collisions. In order to collect first informations for the upcoming SpaceGrains project, we realized our simulations within the frame of the experimental cell dedicated to the first working package (Granular gases and pattern formation).

4.2   Setup for SpaceGrains

In our simulations, we reproduced the experimental cell using a rectangular box of $h =$60 mm in height an $\ell =$30 mm in side length. The top and bottom plates of the cell, noted respectively π_1 and π_2, oscillate in phase opposition with an amplitude A and a frequency f. Both parameters are tunable but given the low impact of f on the observed dynamics, only the influence of A will be explored. The distance between both oscillating plates is noted L and can be modified. This allows us to change the accessible volume in the system and thus to tune the packing fraction for a constant number of particles. Figure 4.1 is a sketch of the simulated cell.
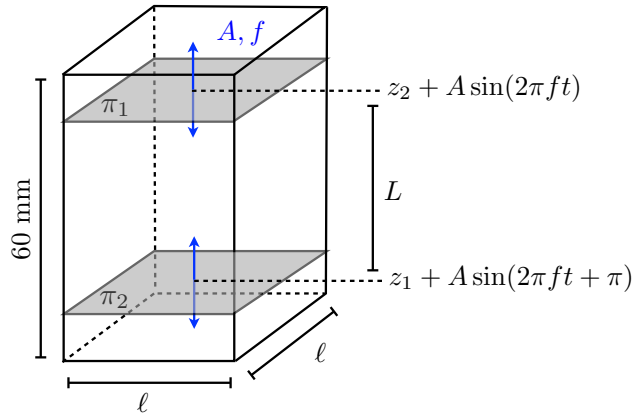
Figure 4.1: (Taken from [92]) Sketch of the cell dedicated to granular gases and pattern formation in the SpaceGrains instrument. The top an bottom plates of the container oscillate in phase opposition with an amplitude A and a frequency f. The distance L is a tunable parameter.

In order to realize a complete study of the system, we also simulated a cell of side length $\ell = 15$ mm even though no corresponding cell is planned for the SpaceGrains instrument. However, it seemed important to be able to modify the volume without additional constraints on A. We realized several simulations, varying the different geometric parameters of the cell and the radius R of the enclosed spherical particles. For each simulation, the number of particles is tuned in order to obtain a transition from a granular gas to a dynamical cluster and a phase diagram is established.

4.3   Main results

In our study [92] we highlighted the cluster's formation mechanisms at two different scales. At the scale of the grains, the presence of a cluster is related to the caging of particles within their

neighborhood. Indeed, we show that the statistical detection of a cluster coincides with a sharp increase in the number of caged grains. At the scale of the entire system, the upcoming of a cluster can be explained by the competition between the energy propagation stirring up the granular media and the energy dissipation at each collision. A characteristic time scale can be defined for each process. The typical relaxation time in the system is given by the parameter τ_H found in Haff's cooling law (1.8). The typical time for the propagation of the injected energy can be estimated as following,

$$\tau_P = \lambda \left(\sum_{i=0}^{n} \frac{1}{v_0 \varepsilon^i} \right), \tag{4.3}$$

where $v_0 = A\omega$ is the initial velocity near the pistons and ε is the coefficient of restitution. The mean free path λ and the average number of collisions during one period n can be deduced by purely geometric means. If the system cools down faster than the energy can be propagated, which corresponds to the criterion $\tau_H \leq \tau_P$, particles start to gather and a cluster appears. The equality $\tau_H = \tau_P$ leads to a theoretical law predicting the frontier between the gas and the cluster regimes. Note that our model is in excellent agreement with the transition that we measured in our simulation concerning SpaceGrains and in the reproduction of Falcon's experiments [79]. Figure 4.2 shows the obtained phase diagram in which we superposed our model with all transition points from the different setups.
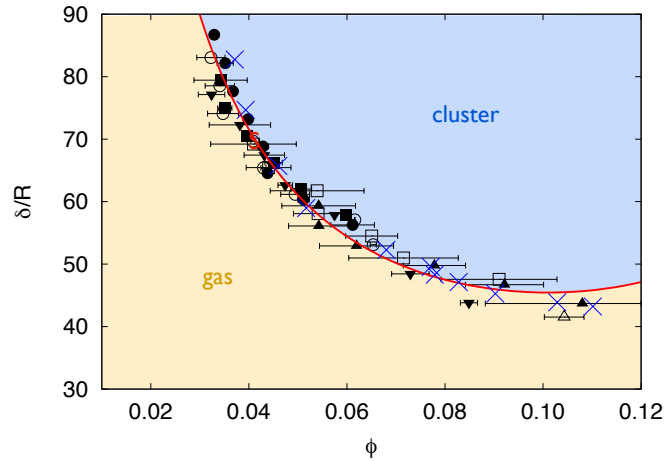
Figure 4.2: (Taken from [92]) Phase diagram of the dynamics presented by the driven granular system. Different symbols correspond to the gas-cluster transition points concerning different setups. Our theoretical model is represented by the solid red line.

4.4 Conclusion

Thanks to this work, the mechanisms behind the gathering of driven granular media could be determined. Indeed, our theoretical model allows us to describe the frontier between the gaseous and the cluster regime and is in excellent agreement with the statistical frontier from figure 3.3. Accordingly, it is now possible to predict, for various rectangular cell geometries, the apparition of a dynamical cluster. This new ability is important for the SpaceGrains project since the large field of parameters that had to be explored can be reduced dramatically regarding our model. Moreover, being able to create efficiently a clustered system allows us to begin to explore the manipulation of these gathered granular materials.

Dynamical clustering in driven granular gas

E. Opsomer[(a)], F. Ludewig and N. Vandewalle

GRASP, Physics Department B5a, University of Liège - B-4000 Liège, Belgium, EU

Abstract – Driven granular gases present rich dynamical behaviors. Due to inelastic collisions, particles may form dense and slow regions. These clusters emerge naturally during a cooling phenomenon but another dynamical clustering is observed when the system is continuously excited. In this paper, the physical processes that trigger the transition from a granular gas to a dynamical cluster are evidenced through numerical simulations. At the granular scale, the transition is evidenced by the observation of caging effects. At the scale of the system, the transition is emphasized by density fluctuations. Physical arguments, based on relaxation times, provide an analytical prediction for the edge between dynamical regimes.

Introduction. – Driven granular materials represent a paradigm of dissipative systems. Collisions provoke a loss of energy that is counterbalanced by the external excitation. In dilute systems, this equilibrium leads to a stationary regime being the granular gas [1]. This dynamical regime is fundamentally different from the classical continuous gas. Indeed, velocities do not follow Maxwell-Boltzmann [2] distributions and usual thermodynamical laws have to be readapted [3–5]. Moreover, the dynamics of a granular gas depend on the type of energy injection. Mechanical shaking with pistons modifies the accessible volume of the cell. Oppositely, magnetically shaking [6] can lead to magnetic effects and additional potentials between the particles. In addition to the shaking mechanism, the gravitational field has also a major impact on system. Under gravity, the density increases towards the bottom of the cell and resonance has been reported [7]. In order to avoid these parasite phenomena, the study of granular gases requires microgravity. Indeed, under this condition, stationary homogeneous states can be reached for a small external driving. Once the energy supply is turned off, the system starts a cooling process. Inhomogeneities are created and form dense patterns [8,9] generally called clusters. However, even for continuously driven systems, local density variations have also been observed [10,11]. This dynamical clustering needs injected energy to subsist because it endures a constant renewal of its particles [12].

Our interest goes to the transition from the granular gas to the dynamical cluster that can be triggered by the manipulation of a broad range of parameters. Since microgravity is required for sustaining a granular gas, numerical simulations using DEM-like algorithms are performed. Our work is based on the experimental features of the VIPGRAN [13] device of the European Space Agency.

In this paper, the detection of the dynamical regime in the system is achieved by a statistical adequation test already used in earlier simulations [12,14]. Space-time diagrams of the mean kinetic energy in the system are presented and open new perspectives.

Numerical model. – Our numerical model reproduces the experimental setup of VIPGRAN. Figure 1 gives a brief overview of this system geometry. Inside a cell of dimensions $30 \times 30 \times 60$ mm, two pistons π_1 and π_2 enclose N spherical particles of radius R. These pistons are oscillating sinusoidally in phase opposition around their respective equilibrium points z_1 and z_2 with an amplitude A and a frequency f. The distance $L = |z_1 - z_2|$ can be modified in order to change the mean volume for a fixed amplitude. The period of oscillation is noted T.

The simulations are based on the Molecular Dynamics (MD) [15,16] approach. This model is widely used in soft-matter physics and especially in the simulation of granular materials [12] because of its capacity to handle efficiently multiple collisions that are unavoidable in dissipative systems. Normal forces F_{ij}^n are composed by a repulsive F_{ij}^{rep} and a dissipative F_{ij}^{dis} component. The repulsive
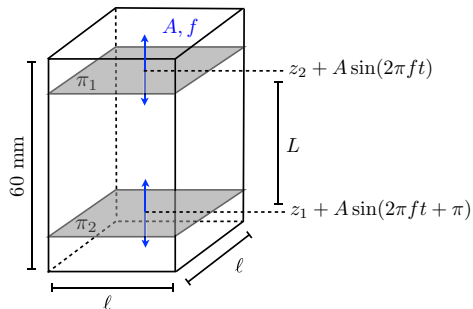

Fig. 1: (Color online) Sketch of the VIPGRAN cell. Two pistons are oscillating sinusoidally in phase opposition around their respective equilibrium points z_1 and z_2. The oscillation parameters are the amplitude A and the frequency f. The distance L separating z_1 and z_2 is tunable. Finally, the side length ℓ is fixed during each experiment.

component follows Hooke's law

$$F_{ij}^{rep} = -k_n \delta_{ij}, \tag{1}$$

where δ_{ij} is the overlap of two adjacent solids i and j. The constant k_n is the normal stiffness which is a purely numerical parameter. The stiffness is determinate by a maximum particle deformation of $R/100$ for two grains in frontal collisions with relative velocity $2A\omega$, where $\omega = 2\pi f$. The dissipative component is taken into account by viscous forces according to the following law:

$$F_{ij}^{dis} = -\gamma_n(k_n, \varepsilon) \frac{\partial \delta_{ij}}{\partial t}, \tag{2}$$

where the viscous constant γ_n [15] is a function of the normal stiffness k_n and the restitution coefficient ε. This restitution coefficient is used for both, grain-grain and grain-wall collisions. Tangent forces F_{ij}^t are bounded and depend on the relative tangent velocities v_{ij}^t between the colliding solids i and j. One has

$$F_{ij}^t = -k_t v_{ij}^t \quad \text{and} \quad \|F_{ij}^t\| \leqslant \mu F_{ij}^n, \tag{3}$$

where μ is a friction coefficient and k_t a purely numerical constant. For more realistic force models, such as viscoelastic forces, similar results are expected. Further details concerning the MD simulations are given by Taberlet [17].

Numerical results. – A large number of numerical simulations were realized in order to cover the complete set of tunable parameters. For fixed values of L, A and R, different dynamical regimes could be observed depending on the number N of grains in the system. A complete description of the investigated parameters is given in table 1. The side length ℓ cannot be changed in the VIPGRAN experiment but its influence on the system's dynamics is numerically investigated. Note that all simulations were realized for fixed values of $\varepsilon = 0.9$ and $f = 10\,\mathrm{Hz}$.

Table 1: Parameters for the different simulated systems. Symbols are given according to the results presented in figs. 5 and 7. The symbol S stands for a typical set of parameters corresponding to figs. 2, 3, 4 and 6. The symbol $\times$ corresponds to earlier simulations [12].

A (mm)	L (mm)	ℓ (mm)	R (mm)	Symbol
4.0	30.0–47.5	30	0.5	●
5.0	30.0–47.5	30	0.5	○
6.0	35.0–47.5	30	0.5	■
5.0	32.5–47.5	30	0.6	□
5.0	35.0–47.5	30	0.7	▲
5.0	47.5	30	1.0	△
5.0	30.0–47.5	15	0.5	▼
5.0	40.0	30	0.5	S
2.5	10.0	10	0.13–0.32	$\times$
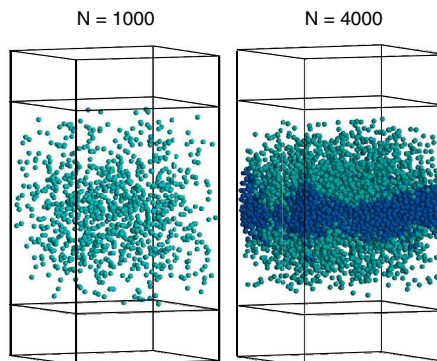
Fig. 2: (Color online) Snapshots of the main cell for, respectively, $N = 1000$ and $N = 4000$ grains. One grain layer at rest contains nearly 1000 grains. For small number of grains the system behaves like a gas. When the number of grains increases, dense and slow moving clusters are formed in the corners and grow towards center of the system. These dark gray (blue) clusters are detected by the following caging criteria.

Indeed, the latter exhibits that the frequency might not be a pertinent parameter for the emergence of the expected phenomenon. Figure 2 presents snapshots of the simulated cell for a typical set of parameters referred as S in table 1. In the dilute case of 1000 grains (nearly one grain layer at rest), particles are homogeneously distributed in the whole volume. Moreover, collisions are rare events and the particle velocities approach $A\omega$. In opposite, for 4000 grains, contacts between particles are frequent events and according to the dissipative character of these collisions, energy is dissipated. When the number of grains increases, one can assist to the formation of dense zones of low grain velocity growing from the corners towards the centre of the cell. These dark gray (blue) clusters, that can be detected by a following caging criteria, are surrounded by a loose gas-like zone. Both phases are coexisting and form a complex dynamical equilibrium. Surface grains are indeed ejected

Fig. 3: (Color online) Three typical trajectories of grains in the system along the (y, z)-plane during 20 periods. For $N = 1000$, displacements are of the size of the system and straight lined, in opposition to the short and curly trajectories observed for $N = 4000$ which are characteristics of caging effects.

Fig. 4: (Color online) Gas-cluster transition in the system depending on the number N of grains for the set of parameters S. The Kolmogorov-Smirnov test T_{KS} is plotted in black as a function of the number of grains with local packing fraction $\phi_\ell > 0.285$ in gray (blue). The light gray (red) line corresponds to the statistical threshold. The vertical dashed black line refers to the transition detected by the statistical test and corresponds with the apparition of the first significant number of caged grains.

by the cluster, but this loss of matter is recovered by new energetic particles coming from the pistons.

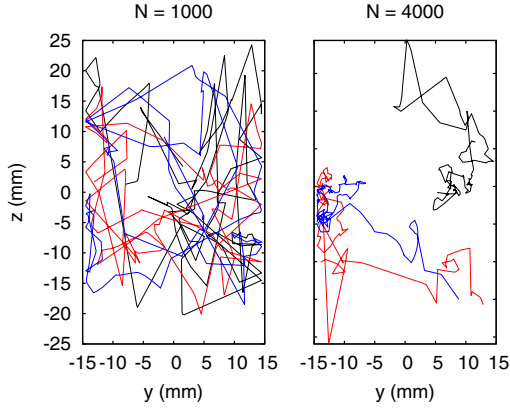At the scale of grains, the presence of clusters can be linked to some "caging effect". Indeed, high local densities imply that a grain cannot leave its neighborhood without colliding and losing kinetic energy. Evidence of such caging effect is illustrated in fig. 3 by the tracking of randomly chosen particles during 20 periods. The system is based on the set of parameters S. In order to simplify the visualization a (y, z)-projection is used. The trajectories of three particles are represented by a black, a gray (blue) and a light gray (red) line. For a gas ($N = 1000$), the trajectories are rather straight lined and of the size of the system. The entire volume is visited, which is expected for a homogenous gas. For a clustered system ($N = 4000$), trajectories are straight lined in the gas phase near the pistons, but once a grain travels into the central zone, a caging effect is observed. Indeed, the trajectories remain localized. The grains are trapped and their energy is dissipated by a succession of inelastic collisions.

The loosest local configuration corresponding to a cage is a grain surrounded by 6 neighbors in a cubic lattice of side length $\sqrt{6}R$. For this arrangement, the central grain cannot travel behind its neighborhood without collision. In terms of packing fraction $\phi = N v_g / V$, where v_g is the volume of a grain and V the maximum volume of the cell, a cage is formed above a threshold value $\phi_c = 0.285$ that was already observed in earlier work [12]. In order to count the number N_c of grains that are caged in the system, a local packing fraction ϕ_ℓ has to be measured. This can be achieved from a Voronoï tessellation. Indeed, for each particle a Voronoï cell of volume V_ℓ is obtained. Accordingly, a grain is considered as caged if $\phi_\ell = v_g / V_\ell > \phi_c$. For the set of parameters S, fig. 4 describes in gray (blue) the evolution of N_c for increasing N. The first

significant value of N_c is obtained for $N = 3525$. Important dissipative phenomena are then expected.

At the scale of the whole system, the signature of the cluster formation is given by the positions of the grains in the cell volume. Expecting that for low densities the grains will spread homogeneously, a uniform distribution corresponds to a gas-like system. A statistical test is a reliable tool in order to detect the dynamical regime of the system [12]. The two-sample Kolmogorov-Smirnov adequation test (KS test) [18] compares the cumulative distribution function $F(z)$ of the grain positions along the z-axis with the cumulative distribution function $U(z)$ of a uniform law. For a fixed number of grains N, the test value T_{KS} is given by

$$T_{KS} = \sqrt{\frac{k}{2}} \sup_{|z| \leqslant L - 2A} |F(z) - U(z)|, \qquad (4)$$

where k is the number of classes characterizing the distributions. If T_{KS} exceeds the statistical threshold K_α, depending on k and on the the level of significance α, the hypothesis of uniformity is refuted and the system is assumed to be in a cluster regime. Figure 4 describes in black, the evolution of T_{KS} as a function of N realized for the set of parameters S. The statistical threshold K_α is represented in light gray (red). Once $T_{KS} > K_\alpha$, a critical number of grains triggering the transition can be extracted. Moreover, this transition corresponds to the apparition of the first significant number of caged particles and the results of the global test are in perfect agreement with the results of the local detection method.

An automatic detection of the gas-cluster transition curve is introduced. In each simulation, the KS test is used

Fig. 5: Gas-cluster transition points, as detected by the KS test, depend on the number of grains and on the height of the constraint-free zone of the cell. The symbols correspond to different simulation parameters according to table 1.

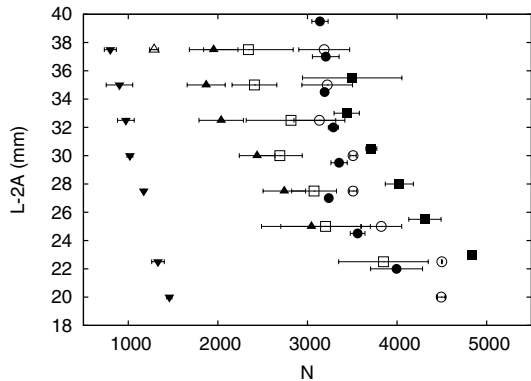to detect the dynamical regime of the system. Starting with two initial filling numbers of $N = 500$ and $N = 5000$, a gas and a cluster are respectively detected. Obviously, the transition occurs between those values and can be approached by interpolation. For the obtained number of grains a new simulation is performed and the test is applied again. This dichotomy allows to refine the edge with sufficient precision. Figure 5 presents the gas-cluster transition points depending on the number of grains and on the height $L - 2A$ of the constraint-free zone of the cell. The symbols refer to the different simulation parameters according to table 1. The error bars correspond to the precision of the detection and depend on the number of iterations in the dichotomy procedure.

All transition lines present similar behaviors but for different ranges of the parameters. For a fixed height, as more energy is dissipated, clustering appears when the number of grains increases. Moreover, a cluster appears for a constant grain number by increasing $L - 2A$. This seems counterintuitive since the number density $\eta = N/V$ gets lower. Nevertheless, if the volume increases for constant N, less particles are present next to the pistons and less energy is injected in the cell. As only few energetic particles arrive in the central part of the cell, the system cools down, which leads to the formation of a dense region. In order to investigate more deeply this energetic approach of clustering, space-time diagrams were established. Based on the set of parameters S, fig. 6 describes the evolution, at different heights z, of the mean kinetic energy E_k in the system as a function of the dimensionless time t/T. This energy is normalized by the kinetic energy of a single grain moving at speed $A\omega$ and displayed using a linear color scale. In order to improve the statistics, the diagram is averaged over 20 periods.

In the gas state (fig. 6, top) one observes that for $0.4 \leqslant t/T < 0.8$ a large amount of energy is injected into the system according to the motion of the pistons.
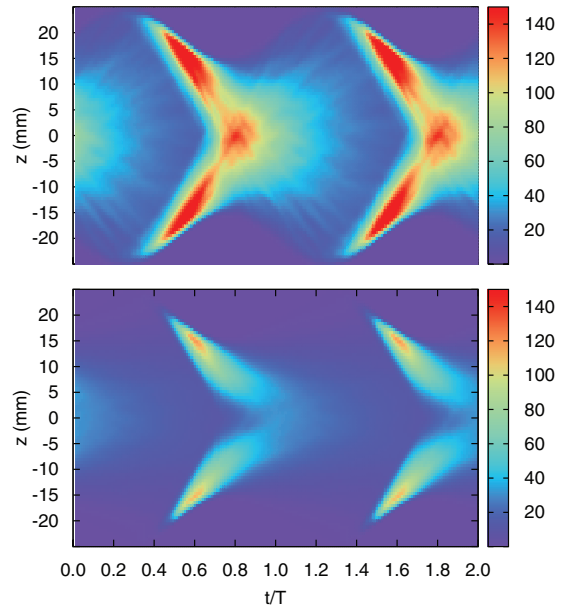
Fig. 6: (Color online) Space-time diagram of the mean kinetic energy for 1000 grains (top) and 4000 grains (bottom) in the cell. A linear color scale is used. In the gas regime, periodic patterns corresponding to high speed trajectories are observed and could correspond to different bouncing modes of the grains. In the cluster regime, a deviation of these trajectories is observed as the grains encounter a dense central region. The constant decrease of the slope of the trajectories is due to successive collisions through the media.

Evaluating the slopes of typical trajectories in this diagram leads to an approximative injection velocity v_0 that lies between $A\omega$ and $2A\omega$. Despite the average of the collected data, discrete energetic trajectories are visible for $0.8 \leqslant t/T < 1.4$. This could evidence a periodic behavior of the particles in the cell. Indeed, the energetic branches on the diagram could correspond to the different oscillation modes established in the system. In the cluster case (fig. 6, bottom) one can find a correspondent energy injection near the pistons. However, even if initially the slopes are similar, the energy level is much lower which means that for high η less grains are near the pistons. Moreover, one observes a deviation of the trajectories at about $t/T = 0.7$ corresponding to the encounter of the energetic grains with the cluster. Due to multiple collisions, the speed drops and the slope of the trajectories decreases more and more. The discrete trajectories present in the gas are no longer visible and only a few grains are leaving the central zone. At the scale of one period, the injected energy reaching the center of the system is not high enough to break up the clusters and to spread the grains through the system.

Energetic approach. – Our numerical results stress the importance of two main processes in the cluster formation mechanism: i) the amount of injected energy

and its propagation; ii) the dissipation of this energy through a series collisions. This last mechanism has been quantified for free cooling systems and follows Haff's law (5) as long as the system is dilute. One has

$$\langle v(t) \rangle = \frac{v_0}{1 + t/\tau_H},$$ (5)

where v_0 is the typical injection velocity and the operator $\langle \cdot \rangle$ denotes the average. The Haff time τ_H is the typical relaxation time [19] for granular gases and is given by

$$\tau_H = \frac{2}{v_0(1 - \varepsilon^2)\eta\sigma},$$ (6)

where σ is the cross-section $\pi(2R)^2$ of the grains. The propagation of the energy through the system is more complex and depends on the mean free path of each particle as well as on the size of the system. The typical length δ of the system is given by the mean distance that the grains achieve when they pass across the constraint-free zone. Accordingly, δ corresponds to the average distance separating two points P_1 and P_2, respectively, in the surfaces π_1 and π_2 of the pistons when they are as close as possible.

$$\delta = \langle |\overrightarrow{P_1 P_2}| \rangle.$$ (7)

The effective volume visited by a grain is then given by $\delta\sigma$ which leads to a number $n = \eta\delta\sigma$ of encountered collisions during its particle motion. At each binary collision, a certain amount of energy is dissipated. This loss can be translated in terms of velocity according to the law $v' = v\varepsilon$, where v and v' are, respectively, the grains velocities before and after the collision. If one sees the energetic transfer as a dissipative chain reaction through the system, a characteristic propagation time τ_P can be estimated. One has

$$\tau_P = \frac{\delta}{n} \left(\sum_{i=0}^{n} \frac{1}{v_0 \varepsilon^i} \right),$$ (8)

where δ/n acts as the mean free path. If the energetic impulse coming from the piston has enough time to travel across the system and to spread the particles in the whole volume as is seen in fig. 6 the system is in a gas-like regime. In the opposite, if the system has not enough time to propagate, dense central zones are generated due to cooling. The system dynamics appear as a competition between both time scales. Accordingly, a clustering condition can be given by

$$\tau_H < \tau_P.$$ (9)

By simplifying and using the geometric character of the sum in τ_P, the condition (9) can be reformulated as follows:

$$\delta > \frac{\xi}{\sigma\eta},$$ (10)

where ξ depends on ε according to

$$\xi = -\frac{\ln\left(1 + \frac{2}{\varepsilon(1+\varepsilon)}\right)}{\ln \varepsilon} - 1.$$ (11)
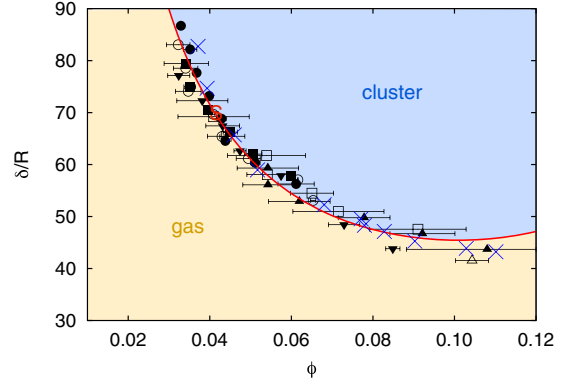
Fig. 7: (Color online) Transitions points detected by the KS test using the symbols according to table 1 in black and $f(\phi)$ in gray (red).

However, the estimation of τ_P neither takes into account the size of the grains nor their deviation at impact. Since the interaction between particles depends on a surface-to-surface distance, a corrective term nr_0, with $0 < r_0 \leqslant 2R$ has to be subtracted from the typical length δ. This value r_0 is linked to the impact angle θ and can be determined by considering the repartition of the velocities. Indeed, after each binary collision assuring the energy transmission, both grains continue their movement with different velocities. The transmitted speed corresponds to $v\cos\theta$, where v is the velocity of the incident grain before impact. By following after each collision the fastest grain, the deviation in the energy transmission is limited by a critical angle of $\pi/3$ that leads to the estimation

$$\frac{r_0}{R} = \frac{3}{\pi} \int_0^{\frac{\pi}{3}} 2\cos(\theta)\mathrm{d}\theta = 1.654.$$ (12)

By reorganizing condition (10) in order to use the packing fraction $\phi = \sigma\eta R/3$, a dimensionless expression can be obtained and the parameters ϕ and δ/R assure the collapse of the gas-cluster transition points presented in fig. 5 along a unique curve of equation

$$f(\phi) = \frac{\xi}{3\phi} \left(\frac{1}{1 - 3(r_0/R)\phi} \right).$$ (13)

Figure 7 is a $(\delta/R, \phi)$-phase diagram presenting these transition points by using the symbols of table 1 in black and $f(\phi)$ in light gray (red). Equation (13) captures the transition for all sets of data investigated herein.

In order to confirm the reliability of the presented law, $f(\phi)$ is compared to the empirical frontier between gas and cluster regime of earlier Mini-Texus simulations [12] represented by the gray (blue) crosses in fig. 7. The agreement is excellent. Nevertheless, f departs from the set of points for large values of ϕ. Indeed, the limits of the model are reached, the hypothesis of strong dilution is not respected and Haff's law [19] is no longer valid.

Conclusion. – In summary, we characterized and numerically confirmed the transition between a granular gas and a dynamical cluster at the scale of the grains and at the scale of the entire system. Both approaches concord and lead to an efficient cluster detection. A model based on the energy propagation in the system provides a scaling law for the edge between both dynamical regimes. The only fitting parameter r_0/R of this law is constant for systems of different dimensions and oscillation types.

Our work opens new perspectives. Indeed, our results could help to fix the parameters of the VIPGRAN experiment. Moreover, a model taking cells with several compartments into account could be imagined in order to manipulate or to direct clusters.

$* * *$

REFERENCES

[1] Aumaître S., Farago J., Fauve S. and Mc Namara S., *Eur. Phys. J. B*, **42** (2004) 255.
[2] Olafsen J. S. and Urbach J. S., *Phys. Rev. E*, **60** (1999) R2468.
[3] Jop P., Forterre Y. and Pouliquen O., *Nature*, **441** (1999) 04801.
[4] Eggers J., *Phys. Rev. Lett.*, **83** (1999) 5322.
[5] Goldhirsch I., *Annu. Rev. Fluid Mech.*, **35** (2003) 267.
[6] Yu P., Staerk E. and Sperl M., in preparation (2012).
[7] Falcon E., Fauve S. and Laroche C., *Eur. Phys. J. B*, **9** (1999) 183.
[8] Brillantov N., Salueña C., Schwager T. and Pöschel T., *Phys. Rev. Lett.*, **93** (2004) 134301.
[9] Goldhirsch I. and Zanetti G., *Phys. Rev. Lett.*, **70** (1993) 1619.
[10] Kudrolli A., Wollpert M. and Gollub J. P., *Phys. Rev. Lett.*, **78** (1997) 1383.
[11] Falcon E., Wunenburger R., Evesque P., Fauve S., Chabot C., Garrabos Y. and Beysens D., *Phys. Rev. Lett.*, **83** (1999) 440.
[12] Opsomer E., Ludewig F. and Vandewalle N., *Phys. Rev. E*, **84** (2011) 051306.
[13] ESA VIPGRAN project, URL: `http://www.esa.int/`.
[14] Opsomer E., Ludewig F. and Vandewalle N., *J. Phys.: Conf. Ser.*, **327** (2005) 012035.
[15] Pöschel T. and Schwager T., *Computational Granular Dynamics* (Springer-Verlag, Berlin, Heidelberg) 2005.
[16] Luding S., *Granular Matter*, **10** (2007) 235.
[17] Taberlet N., PhD Thesis (Université de Rennes I) 2005.
[18] Eadie W. T., Drijard D., James F. E., Roos M. and Sadoulet B., *Statistical Methods in Experimental Physics* (North-Holland, Amsterdam) 1971, pp. 269–271.
[19] Maaß C. C., Insert N., Maret G. and Aegerter C. M., *Phys. Rev. Lett*, **100** (2008) 248001.

Part III

Handling of granular materials in microgravity

Chapter 5

Clustering and Maxwell's demon

In the scientific literature, the notion of clustering is often associated to a granular trapping. In general, this trapping corresponds to a localization of the majority of the granular material in a particular region of the container. For instance, by dividing a driven system into several sub cells, it is possible to observe the granular pendant of Maxwell's demon [65–67]. Let us imagine a rectangular system in which a vertical wall divides the container in two (see figure 5.1). The latter wall is however not as high as the entire container so that the enclosed particles can travel from one side to another. In this case the granular trapping is easy to understand since the collisions between
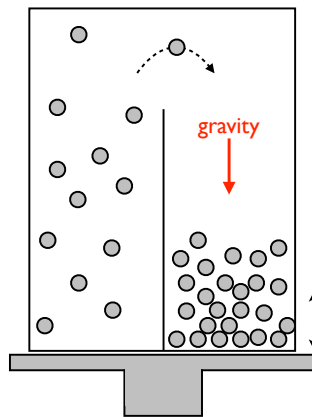
Figure 5.1: Sketch of the a compartmentalized container contain granular material. The system is driven and a gathering of the grains can be expected in one side of the cell

the particles are dissipative. Once enough grains have found themselves (randomly) in the same compartment, too much of the injected energy is dissipated by the particle's interactions. The grains can't overcome anymore the potential barrier represented by the wall and remain trapped on this side. But what happens if the same experiment is realized under microgravity conditions? Has the cell to be adapted? Is the gathering even possible? Answers to these questions can be found considering our clustering theory.

5.1   Motivations

The dimensions of the cell are important parameters that can trigger the clustering in the same way than the number of particles. Accordingly, creating smaller sub cells in a container encourages locally the formation of a dynamical cluster. A trapping of the grain can thus be achieved without any potential barrier induced by gravity. However, if one considers the up-down symmetry induced by the weightlessness, the cell should be adapted.

In the following article, we studied the feasibility of granular trapping in the SpaceGrains instrument. We realized simulations in order to reproduce the phenomenon and to analyze the formation of the traps. Depending on the global filling of the system, different clustering regimes are observed and a corresponding bifurcation diagram is presented. Finally, we proposed two models predicting the steady states of the system.

5.2   Setup for SpaceGrains

The first step consisted in the design of the container and its subcells that is compatible with the SpaceGrains instrument. Inspired by the setup of Dorbolo and coworkers [65], we decided to divide our cell according to a lattice. We placed two perpendicular walls in the center of the simulated cell in order to create four smaller compartments. The height of this additional structure is 30 mm which is small enough to allow the exchange of particles between the cells for any piston position. A sketch of the simulated setup is given in figure 5.2. Once again, the pistons oscillate sinusoidally in anti-phase with an amplitude A and a frequency f. Note that for this study the mean distance L has been fixed to 50 mm.
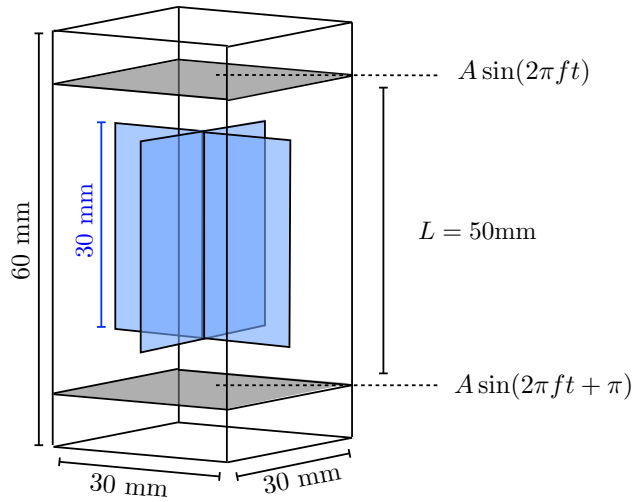
Figure 5.2: Sketch of the modified SpaceGrains cell. The addition of two perpendicular walls in the center of the cell lowers locally the clustering threshold and allow thus the trapping of the grains. Both pistons oscillate in phase opposition with amplitude A and frequency f. For this study the mean distance L is fixed to 50 mm.

5.3   Main results

We realized simulations for fixed driving parameters and for an increasing number of grains N. The trapping of particles in one or more compartments is observed and can be linked to a dynamical clustering in particular subcells. Indeed, the formation of a single trap in the system can be predicted by our clustering theory presented in [92]. The dynamics of the particles and the granular exchange between the compartments are captured by two complementary models. A first iterative model allows us to reproduce efficiently the evolution of the system. A second theoretical model, based on the particle fluxes in the system, gives us the asymptotic stable states. Note that despite the resemblance to many similar experiments (granular fountains and ratchets) on earth, the microgravity conditions leads to residual particle fluxes from one compartment to another even for high fillings. Figure 5.3 shows snapshots of the simulated system for different values of N.
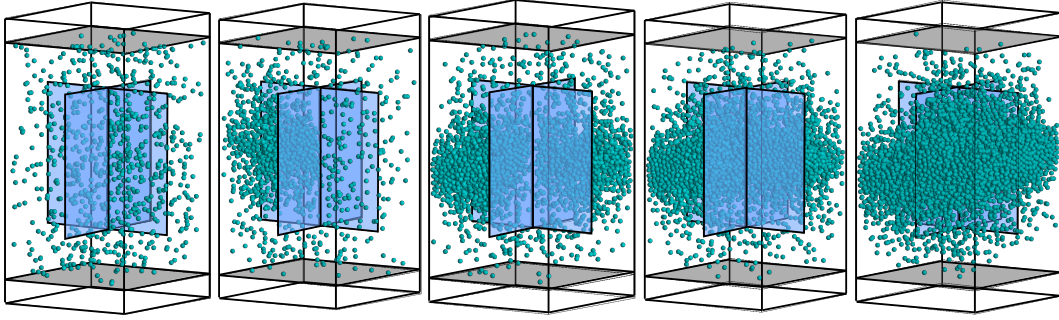
Figure 5.3: (Taken from [93]) Snapshots of the simulated cells for an increasing number of particles N (from left to right: 500, 1400, 3100, 5900, 7500). For low values of N, granular gas is observed. For higher fillings, one can assist to the formation of several trapping regimes.

5.4 Conclusion

We showed that a granular version of Maxwell's demon can be realized in microgravity environment. The presented design could easily be implemented in the SpaceGrains instrument which would allow an experimental study of the relevant trapping mechanisms. Moreover, this study corroborates our theoretical model concerning the transition from a granular gas toward a dynamical cluster. Indeed, the one trap regime could be predicted by applying our cluster criterion to a cell whose dimensions correspond to those of the subcells.

How dynamical clustering triggers Maxwell's demon in microgravity

E. Opsomer, M. Noirhomme, N. Vandewalle, and F. Ludewig

GRASP, Physics Department B5a, University of Liège, B-4000-Liège, Belgium

In microgravity, the gathering of granular material can be achieved by a dynamical clustering whose existence depends on the geometry of the cell that contains the particles and the energy that is injected into the system. By compartmentalizing the cell in several subcells of smaller volume, local clustering is triggered and the so formed dense regions act as stable traps. In this paper, molecular dynamics simulations were performed in order to reproduce the phenomenon and to analyze the formation and the stability of such traps. Depending on the total number N of particles present in the whole system, several clustering modes are encountered and a corresponding bifurcation diagram is presented. Moreover, an iterative model based on the measured particle flux F as well as a theoretical model giving the asymptotical steady states are used to validate our results. The obtained results are promising and can provide ways to manipulate grains in microgravity.

PACS number(s): 45.70.Qj, 05.45.−a, 02.60.Cb, 05.70.Fh

I. INTRODUCTION

When granular material is vertically driven, the system rapidly reaches a steady-state for which the injected energy and the dissipated energy perfectly outbalance over one period of oscillation [1]. Each collision between particles causes an energy loss that can be quantified via the coefficient of restitution ε. Nevertheless, for strong external forcing, high isotropic velocities are observed and the media behaves like a macroscopic dissipative gas. When such a granular gas is generated in a cell that is compartmentalized by a vertical wall allowing exchange through a slit, a symmetry breaking can appear under certain conditions [2,3]. Indeed, the grains spontaneously start to gather in the same compartment, which can naïvely be related to a sudden drop of the system's entropy. By analogy, this phenomenon is referred to as the granular pendant of Maxwell's demon. Different cell geometries such as cylindric systems [4] and grids [5] can be used, but the relevant physical mechanism remains the same.

In microgravity, granular materials can be gathered by a clustering [6–8]. Clustering is the tendency of a granular material to form dense and slow regions that can trap new incoming grains. While dissipative nature of the collisions are the main motor of the phenomenon, one can make a differentiation between the *classical clustering*, referring to the cooling of granular media [9], and the *dynamical clustering*, which is a condensed steady-state in a driven granular system [10]. Indeed, the first one is obtained through a long process of successive collisions that dissipate the energy and slows down the grains so that nearly immobile stripe-like regions are formed. On the other hand, the second type relies on a permanent energy injection (at the walls) that counterbalances the dissipation. This assures the equilibrium between the dense cluster phase in the center of the system and the gas phase surrounding it. If the energy supply is stopped, the dynamical cluster evaporates and the particles spread in the entire system until a cooling begins. Figure 1 describes these different clustering dynamics via a Kolmogorov-Smirnov (KS) test that confronts the particle distribution with a uniform law. If the test's value is above the threshold, the hypothesis of uniformity is refuted and clustering is observed. Data is obtained by prolonging earlier simulations of granular

gases [11] and stopping the driving in the system after 10 seconds. The gray (red) KS curve indicates that dynamical clustering is detected until $t = 10$ s, when the energy injection is stopped. As the cluster evaporates, the KS curve sharply drops under the threshold (black line), and the system evolves into a gas state that rapidly starts to cool down. The KS curve increases and crosses the threshold again at about $t = 15$ s, which corresponds to the very beginning of a classical clustering.

Dynamical clustering has been observed in horizontal 2D cells [12], parabolic flights, and rocket missions [10] that have been reproduced and completed numerically using molecular dynamics simulations [13]. Moreover, the European Space Agency (ESA) is doing intensive research on the behavior of granular media in microgravity. In particular, the SpaceGrains project [14] focuses on cluster formation and Maxwell's demon. In the main cell of the SpaceGrains device, N spherical particles with a radius R are enclosed in a box of dimensions $60 \times 30 \times 30$ mm³. Two pistons are oscillating in phase opposition with an amplitude A and a frequency f around their respective positions z_1 and z_2. The distance L between z_1 and z_2 can be modified in order to tune the accessible volume of the system. Figure 2 provides a brief description of the systems parameters.

This work aims to investigate the formation of traps and the occurrence of Maxwell's demon in microgravity by numerical simulations. In order to provide predictive results, the simulated system is based on a compartmentation of the main cell of the ESA's SpaceGrains project. We discuss the triggering role of clustering for Maxwell's demon under microgravity conditions and present two theoretical models reproducing the observed phenomena.

II. NUMERICAL APPROACH

The realized simulations are based on a molecular dynamics (MD) approach. This model is widely used in soft-matter physics and especially in the simulation of granular materials [13,15] because of its capacity to handle efficiently multiple collisions that are unavoidable in dissipative systems. Normal forces F_{ij}^n are composed by a repulsive F_{ij}^{rep} and a dissipative F_{ij}^{dis} component. The repulsive component follows
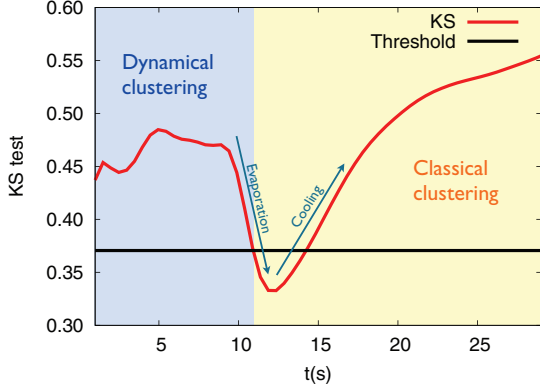
FIG. 1. (Color online) The KS test, represented by a gray (red) curve, indicates the evaporation of a dynamical cluster in microgravity once the driving is stopped (at $t = 10$ s). After a short period of gas phase, a cooling process is observed.

Hooke's law,

$$F_{ij}^{\mathrm{rep}} = -k_n \delta_{ij}, \tag{1}$$

where δ_{ij} is the surface-to-surface distance between two solids, i and j. The constant k_n is the numerical normal stiffness, which is determined by fixing the maximum particle deformation at $R/100$. The dissipative component is taken into account by viscous forces according to the following law:

$$F_{ij}^{\mathrm{dis}} = -\gamma_n(k_n, \varepsilon) \frac{\partial \delta_{ij}}{\partial t}, \tag{2}$$

where the viscous constant γ_n is function of k_n and the restitution coefficient ε. This restitution coefficient is used for both grain-grain and grain-wall collisions. Tangent forces F_{ij}^t are bounded and depend on the relative tangent velocities v_{ij}^t between the colliding solids i and j. One has

$$F_{ij}^t = -k_t v_{ij}^t \quad \text{and} \quad \left\| F_{ij}^t \right\| \leqslant \mu F_{ij}^n, \tag{3}$$

where μ is a friction coefficient and k_t a purely numerical constant. A complete description of this MD approach is given by Taberlet [16].

III. NUMERICAL RESULTS

A. Observations

We realized a large number of numerical simulations reproducing a compartmentalized version of SpaceGrains. Our cell is filled homogeneously with N spherical particles of radius $R = 0.5$ mm. The average distance L between the pistons is fixed at 50 mm. In addition to the basic cell, two orthogonal walls of height $h = 30$ mm are inserted in the center of the cell, as displayed in Fig. 3. This way four subcells are formed. The system is periodically driven with an amplitude $A = 5$ mm and a frequency $f = 10$ Hz. The granular media is shaken up and grains are free to travel from one compartment to another. The observed dynamics depend strongly on N. Indeed, for a small number of grains, the whole system remains in a gas state. The particles travel with high speed and spread homogeneously. For a larger N, a cluster
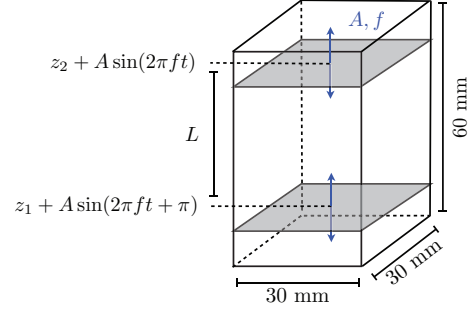

FIG. 2. (Color online) Sketch of ESA's SpaceGrains cell. Spherical particles of radius R are enclosed in a $60 \times 30 \times 30$-mm³ box. Two pistons are oscillating in phase opposition with an amplitude A and a frequency f around their respective positions z_1 and z_2. The distance $L = |z_2 - z_1|$ can be modified in order to tune the accessible volume of the system.

forms and the grains start to gather in the same compartment. This cluster keeps growing and traps the incoming grains until the compartment is filled. When more grains are injected in the system, a second cluster can form and a competition between two traps is observed. Moreover, the second cluster mostly forms in the diagonal neighboring compartment of the first cluster. A further increase of N leads then to the formation of three and, finally, four clusters. This last regime can also be considered as a second homogenous state since all particles are distributed equally in the system. Figure 3 gives a brief overview of the encountered dynamics for an increasing total number of particles. The top row presents the simulated systems while the bottom row shows the top views of the corresponding cells.

B. Filling measures

In addition to its dependency on the total number of grains, the formation of the traps in the system is a dynamical process that evolves continuously. Tracking the filling number n_1, n_2, n_3, and n_4 of the four compartments allows us to evaluate the stability of the observed clusters. This measure implies a temporal discretization that is achieved by using as unit time step the oscillation period T. Figure 4 presents in black lines the evolution of n_i as a function of the number of time steps t. The total number of grains in the system is fixed at $N = 4200$ (two traps are formed). Other colors correspond to complementary simulations explained in Secs. V and VI.

For most simulated systems, a steady-state is reached after 1200 periods. Thanks to the obtained final compartment fillings, a bifurcation diagram describing the different values of n_1, n_2, n_3, and n_4 as a function of N is established and presented in Fig. 5. Until a certain threshold N_c (left dashed line), no trap is observed and all compartment fillings are roughly equal. Then, abruptly, a very neat bifurcation corresponding to the cluster formation occurs. Almost all grains gather in a single compartment leaving three others poorly filled. Recent results [11] allow us to predict the apparition of such dynamical clustering. Indeed, for a given system of maximal volume $v = \ell^2(L + 2A)$, the clustering criterion is given by
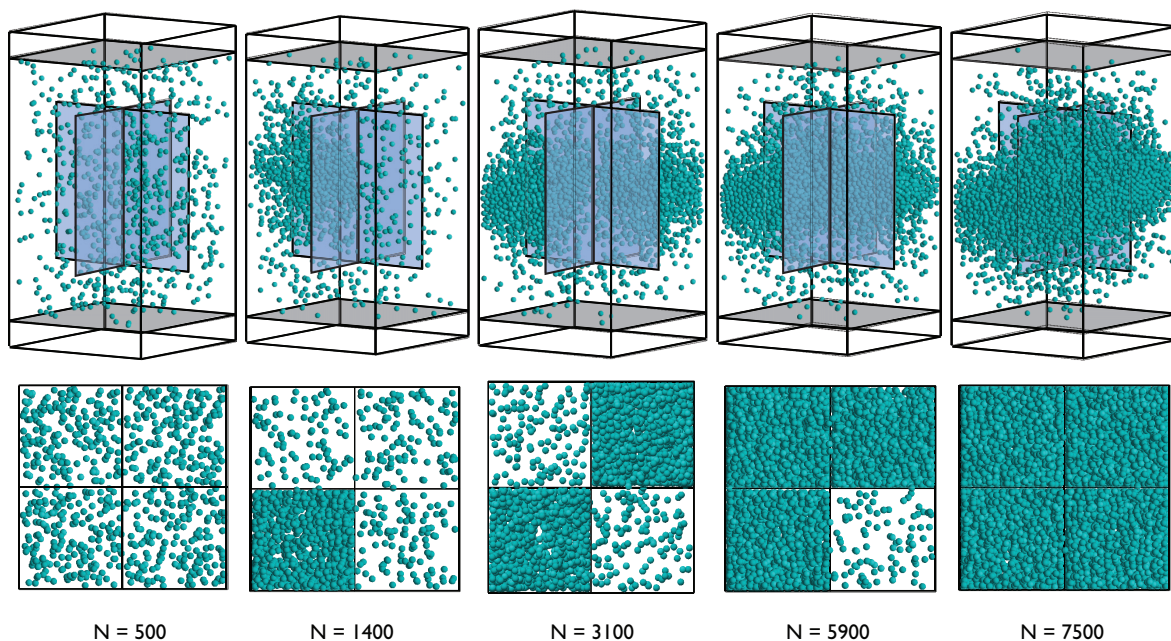
FIG. 3. (Color online) Dynamics of the compartmentalized system for increasing N. The top row displays snapshots of the simulated cells. For high enough filling numbers, clustering is encountered and grains gather in one (or more) compartment(s). The bottom row shows the top view of the corresponding cells.

the following condition:

$$\frac{\delta(L,\ell,A)}{R} > \frac{\xi(\varepsilon)}{3\phi}\left(\frac{1}{1-c\phi}\right), \tag{4}$$

where δ is the characteristic length scale of the cell, c is a constant, and the function ξ depends only on ε. The packing fraction ϕ is defined by

$$\phi = N\frac{4\pi R^3}{3v}. \tag{5}$$

By introducing the geometrical parameters of a compartment into Eq. (4), the local threshold is found to correspond to a filling number $N_c = 808$, denoted by a vertical dashed line in Fig. 5. This single cluster regime persists until a filling number of approximatively 3000 particles, when it is replaced by a regime with two traps. This region is far more noisy, so that the relative compartment fillings n_i/N spread around the value of 0.5. Systems with three clusters are recorded for $N > 4200$;

FIG. 4. Evolution of the filling number of the different compartments over 1200 periods in a system of 4200 grains. Molecular dynamics simulations are represented in black, the iterative model in light gray, and the asymptotic results are displayed as two dark-gray horizontal lines.
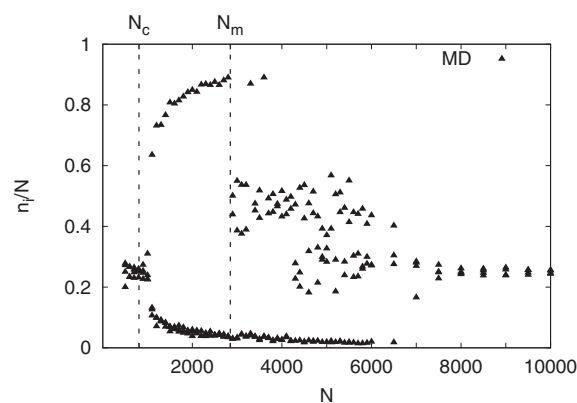
FIG. 5. Bifurcation diagram of the encountered final states of the system. After 1200 periods, the filling ration n_i/N is plotted with black triangles against the total number of particles N. The first bifurcation is predicted by Eq. (4) at a value of $N = 808$. The vertical dashed lines correspond to the critical values of N_c and N_m discussed in the main text.

however, they are rarely observed and seem less stable. Finally, above 6000 grains, the system becomes homogenous again, i.e., clustering takes place in all compartments.

C. Analogy with a granular fountain

These first results described in Sec. III present a lot of similarities with what is found for a granular fountain [17]. In a granular fountain, granular material is driven in a compartmented cell under gravity. Each compartment can communicate with its neighbors either through a slit at a certain height h or by the means of another slit at the bottom of the cell. Like our system, a granular fountain exhibits several trapping modes and multistable regimes. Moreover, the same discontinuous transition is observed on their respective bifurcation diagrams when the first trap occurs. Despite these intriguing analogies, several differences due to the experimental conditions are noted. Indeed, gravity has an impact on the symmetry of the system. The granular fountain as well as our system present two openings per compartment. However, the fluxes present in the fountain are influenced by gravity and have unequal intensities while they are perfectly symmetric in our cell. One can also note that fixed driving parameters were used in the microgravity simulations and that phase transitions are induced by the variation of the number of particles N. Since higher filling fractions can be obtained this way, additional features such as dynamical clustering, crystallization, and overflowing compartments can be generated.

IV. GRANULAR FLUXES

A. Mean flux function

The formation mechanisms of the traps and the complex dynamics of the system are linked to the number of grains that the different compartments exchange. In order to quantify this particle flux, each time a compartment filled with n grains is encountered, the number X_n of grains leaving it for a neighboring compartment is recorded. For a fixed n, the obtained distribution of outgoing grains follows roughly a binomial law

$$X_n \sim \mathcal{B}(n, p_n), \tag{6}$$

where p_n denotes the probability that a grain leaves a compartment filled with n particles. Indeed, this binomial behavior can be interpreted as following: At each time step, the binary-experience *leave* versus *stay* is repeated for each of the n grains. Since the event *leave* has a probability p_n, the random variable X_n follows a binomial distribution. Accordingly, the escape probability is given by the following relation:

$$p_n = \frac{\langle X_n \rangle}{n}, \tag{7}$$

where the mean flux $\langle X_n \rangle$ is the average value of X_n. Figure 6 represents with black dots the evolution of $\langle X_n \rangle$ for an increasing number of grains. For low n, the agitation is strong in the cell and the flux raises up to a maximum value. After that peak, a cluster tends to form; accordingly, the flux drops and becomes nearly constant once the critical value N_c is reached. At that point, the trap becomes stable. The flux
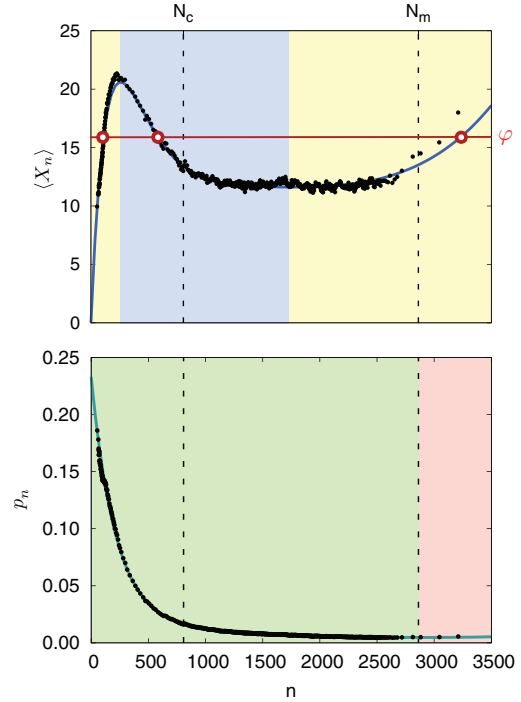
FIG. 6. (Color online) Top figure describes $\langle X_n \rangle$ in black dots and its fit, the mean flux function $F(n)$, in medium gray (blue) for an increasing number of grains. F can be subdivided into three invertible functions in each shaded zone. Moreover, a fixed flux φ can correspond to three fillings as presented by the light gray (red) horizontal line. Bottom figure shows the corresponding evolution of the measured escape probability in black dots and the fitted p_n with a solid gray (green) line.

remains low until the compartment is abundantly filled. The distance between cluster and borders of the compartment gets then smaller and grains can more easily escape. Moreover, the increase of the flux can also be linked to the natural evaporation that is part of the formation mechanism of dynamical clusters. Note that qualitatively similar fluxes are observed in analog systems such as ratchets [18] and granular fountains [17]. However, the observed plateau is a particular feature of our system. An analytical function approaching this mean flux can be found using statistical arguments. For a low n, the escape probability can be approached by the linear combination of two exponential laws of base $0 < p < 1$.

$$p_n = C_1 p^{\gamma_g n(\sigma/\ell^2)} + C_2 p^{\gamma_c n(\sigma/\ell^2)}, \tag{8}$$

where σ/ℓ^2 is the dimensionless cross section of a particle and the coefficients C_1 and C_2 are free fitting parameters. The constants $\gamma_c = 0.14$ and $\gamma_g = 0.86$ model the density increase in the central part of the system under the hypothesis of normal distribution along the oscillation axis.

However, each compartment has a critical capacity, noted N_m, above which the escape probability is expected to increase. This can be modeled by a symmetrization of p_n about N_m that

is noted p_n^*. The mean flux function F is finally defined by

$$F(n) = np_n^*. \tag{9}$$

Fitting F on the average $\langle X_n \rangle$ leads then to a critical filling $N_m = 2849$ that corresponds to a packing fraction of 19%. This critical value is represented by the right dashed line in Fig. 5 and corresponds to a threshold beyond which a second trap can form. The obtained function F is plotted in gray (blue) in the top of Fig. 6 and is in good agreement with the data. The bottom of Fig. 6 shows the corresponding evolution of the measured escape probability in black dots and p_n^* in gray (green).

B. Geometrical coefficients

The relative positions of the compartments also have an impact on the grain exchanges. In order to determine the direction of the outgoing flux, the flux coefficients c_{ij} have to be introduced. They measure the fraction of the flux going from the compartment i to j when $i \neq j$ and have the value $c_{ij} = \{-1\}$ for $i = j$. These coefficients are evaluated on each simulation and then summarized in the following flux matrix:

$$\mathbf{C} = \begin{bmatrix} -1 & 0.46 & 0.46 & 0.08 \\ 0.46 & -1 & 0.08 & 0.46 \\ 0.46 & 0.08 & -1 & 0.46 \\ 0.08 & 0.046 & 0.46 & -1 \end{bmatrix}. \tag{10}$$

The conservation of the total number of grains implies that summing on a row of $\mathbf{C}$ yields 0. Moreover, one can note that the exchange of particles is strong with direct neighbors and weak with the diagonal neighbors. This asymmetry explains why, in the case of a two-cluster system, both traps form in diagonal neighboring compartments. Indeed, this particular configuration minimizes the granular exchange between the clusters and allows, thus, an higher stability of the regime.

V. ITERATIVE MODEL

In order to realize efficiently a great number of simulations, a statistical model based on the mean particle flux has been elaborated. Using F and the flux coefficients c_{ij}, the evolution of the filling n_i of each of the i compartments can be determined according to the following equations:

$$\frac{\partial n_i}{\partial t} = \sum_{j=1}^{4} c_{ji} F(n_j), \tag{11}$$

with $1 \leqslant i \leqslant 4$ and t being the number of time steps. To take into account the statistical fluctuations and to avoid unstable stationary solutions, a stochastic noise term must be injected into Eq. (11). The fluctuations are represented through random variables ζ following a standard normal distribution. According to the Moivre-Laplace theorem, a global flux function can be described by

$$F_\zeta(n) = F(n) + \zeta\sqrt{F(n)(1 - F(n)/n)}. \tag{12}$$

The evolution of the number of grains in the different compartments is then given by Eq. (11), where $F(n_j)$ is replaced by $F_\zeta(n_j)$. For identical initial conditions, the results of this model are in good agreement with of our MD simulations. Indeed,
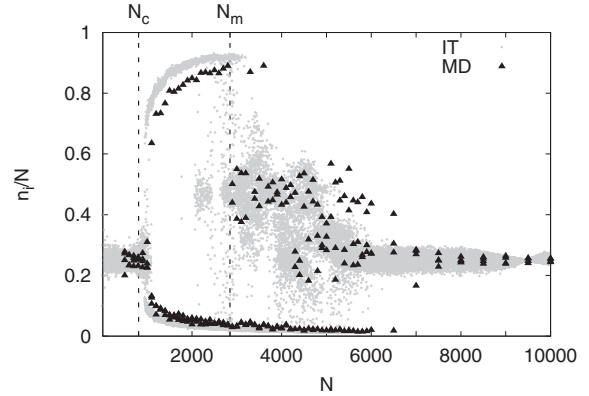
FIG. 7. Comparison between MD simulations described by black triangles and iterative model in light gray based on a limit normal assumption. Critical values N_c and N_m are represented by two dashed vertical lines.

Fig. 4 shows a similar evolution of the iterative approach in light gray and the MD data in black. Moreover, Fig. 7 displays the ratio n_i/N of grains present in each compartment i as a function of N after 1200 iterations. The molecular dynamics simulations are represented by black triangles while the iterative model is colored in light gray. Main branches of the bifurcation diagram are obtained.

VI. THEORETICAL MODEL

A. Stationary solutions

In analogy to earlier works [4,19,20], an asymptotic bifurcation diagram for a granular system in microgravity can be realized. Obviously, the final values of n_1, n_2, n_3, and n_4 are reached once the filling number of all compartments remains constant in time. By writing Eq. (11) in its matrix form, this condition becomes equivalent to

$$\mathbf{M}(\vec{F}) = \mathbf{C} \cdot \vec{F} = \vec{0}, \tag{13}$$

where $\vec{F} = [F(n_1), \ldots, F(n_4)]$. Since each row of the flux matrix sums up to zero, the kernel of $\mathbf{M}$ is the linear hull of the vector $\vec{1} = (1,1,1,1)$. Accordingly, stationary solutions are characterized by $\vec{F} = \varphi\vec{1}$, $\varphi \in \mathbb{R}$, and the fixed-point conditions become

$$\begin{cases} F(n_i) = \varphi & \forall i \in \{1, \cdots, 4\} \\ \sum_{i=1}^{4} n_i = N, \end{cases} \tag{14}$$

with φ being a constant particle flux. These conditions imply the conservation of the total number of particles coupled with an identical flux for all compartments.

B. Sum functions

Since the mean flux $F(n)$ presents both a minimum and a maximum, a same fixed value of φ can be obtain for up to three different fillings as presented in light gray (red) in Fig. 6. Indeed, $F(n)$ can only be inverted piecewise around the different extrema and for each section $l \in \{1,2,3\}$ the

respective inverse function is noted F_l^{-1}. In order to find the asymptotical compartment fillings for a fixed N, all possible combinations implying the three inverse functions and the four boxes have to be considered. For that purpose, the sum functions S_{ij} are introduced and defined by the following relations:

$$S_{ij}(\varphi) = i F_1^{-1}(\varphi) + j F_2^{-1}(\varphi) + k F_3^{-1}(\varphi), \qquad (15)$$

where $k = (4 - i - j)$ with $0 \leqslant i,j \leqslant 4$. The coefficients i,j,k give the effective of the corresponding filling number. Indeed, let φ_0 be a solution of $S_{ij}(\varphi) = N$. If one defines $z_l = F_l^{-1}(\varphi_0)$ for $l \in \{1,2,3\}$, the system is composed by i compartments of z_1 grains, j compartments of z_2 grains, and k compartments of z_3 grains.

C. Stability

The stability of the obtained solutions can be determined via the Jacobi matrix **J** relative to Eq. (11), which can be calculated from

$$\mathbf{J} = \mathbf{C} \cdot \mathbf{diag} \left[\left. \frac{\partial F}{\partial n} \right|_{n=n_1}, \dots, \left. \frac{\partial F}{\partial n} \right|_{n=n_4} \right]. \qquad (16)$$

A solution $(n_1, \dots, n_4)$ is stable if all the corresponding eigenvalues of the Jacobi matrix are negative or equivalently if

$$\max_\lambda \{\lambda | \det(\mathbf{J} - \mathbf{I}\lambda) = 0\} < 0. \qquad (17)$$

Figure 8 presents the stationary solutions of the system using the theoretical approach. Stable branches are described by thick dark gray and unstable by thin black lines. The MD simulations are represented by black triangles. Moreover, the stable solutions for a system of 4200 particles are also represented by two dark gray lines in Fig. 4.

Nevertheless, some differences are noted between the iterative and the theoretical model. This is due to the fact that the theoretical model represents the asymptotic steady state. By computing the iterative diagram for a large number of time
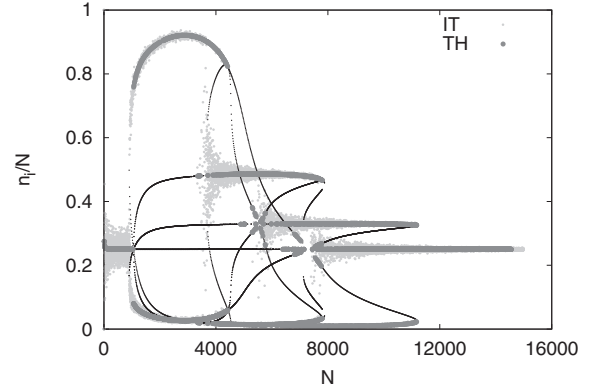
FIG. 9. Comparison between the iterative model in light gray and the theoretical model in dark gray. For a large enough number of iterations, both models converge to the same final states.

steps (12 000) and all different initial conditions, both models converge as shown in Fig. 9.

Moreover, in the multistable region ($N > 6500$), the measured data seemed to prefer the four-cluster state. This repartition is obviously triggered by the homogenous initial conditions that were used in the MD simulations. Indeed, the completed simulations presented in Fig. 9 recover the other branches.

VII. CONCLUSION AND PERSPECTIVES

In this paper, we proposed a particular cell geometry that allows us to produce Maxwell's demon in ESA's SpaceGrains project. Molecular dynamics simulations showed trapping in the different compartments that is triggered by dynamical clustering. Moreover, the presence of clustering and trapping could be predicted thanks to earlier theoretical results [11]. Many analogies with classical systems, such as granular fountains, granular clocks, and ratchets, have been observed and qualitatively similar flux functions were obtained. However, a nonnegligible, almost constant, residual flux was observed for intermediate filling fraction, so that usual models could not properly reproduce the dynamics. A bifurcation diagram recovering the totality of our simulations was presented.

An iterative stochastic model reproducing the systems evolution has been proposed and allowed a more efficient way to simulate the dynamics present in Maxwell's demon. Finally, we describe a theoretical model that gives the asymptotic stable states of the system. Mutlistable regions were expected, but given our initial conditions, a homogenous repartition of the particles is preferred. Note that for a high number of iterations the stochastic model converges to the asymptotic solutions.

Our results are promising because ratchets and others' transport mechanisms, providing ways to manipulate grains in microgravity, can be envisaged in the SpaceGrains experiment.

In the future, larger lattices of 9 or 16 compartments on could be realized. The major difference would be the presence of different fluxes depending on the compartment of interest. Indeed, the central compartments lose grains more easily than the ones in the corners. This could be modeled by either several
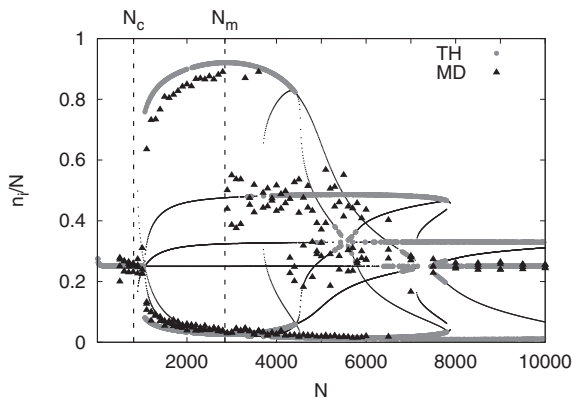

FIG. 8. Comparison between MD simulations (black triangles) and theoretical model. Stable branches are represented with thick dark gray and unstable with thin black curves.

flux functions or by an adapted flux matrix. Other types of compartment arrangements (linear or cylindric) could easily be implemented and compared to our results. Moreover, the effect of the shape of the compartment itself on the flux dynamics could be studied. By using more complex aspherical particles, the influence of the interlocking [21] on Maxwell's demon could be investigated.

[1] S. Aumaître, J. Farago, S. Fauve, and S. Mc Namara, Eur. Phys. J. B. **42**, 255 (2004).

[2] J. Eggers, Phys. Rev. Lett. **83**, 5322 (1999).

[3] A. Barrat and E. Trizac, Molecular Physics **101**, 11 (2003).

[4] K. van der Weele, Contemp. Phys. **49**, 157 (2008).

[5] S. Dorbolo *et al.*, Eur. J. Phys. **32**, 1465 (2011).

[6] Y. Li, M. Hou, and P. Evesque, J. Phys. Conf. Ser. **327**, 012034 (2011).

[7] N. Isert, C. C. Maaß, and C. M. Aegerter, Eur. Phys. J. E **28**, 205 (2009).

[8] J. J. Brey, F. Moreno, R. García-Rojo, and M. J. Ruiz-Montero, Phys. Rev. E **65**, 011305 (2001).

[9] I. Goldhirsch and G. Zanetti, Phys. Rev. Lett. **70**, 1619 (1993).

[10] E. Falcon, R. Wunenburger, P. Evesque, S. Fauve, C. Chabot, Y. Garrabos, and D. Beysens, Phys. Rev. Lett. **83**, 440 (1999).

[11] E. Opsomer, F. Ludewig, and N. Vandewalle, Europhys. Lett. **99**, 40001 (2012).

[12] A. Kudrolli, M. Wolpert, and J. P. Gollub, Phys. Rev. Lett. **78**, 1383 (1997).

[13] E. Opsomer, F. Ludewig, and N. Vandewalle, Phys. Rev. E **84**, 051306 (2011).

[14] ESA SpaceGrains project: http://www.spacegrains.org/

[15] S. Miller and S. Luding, Phys. Rev. E **69**, 031305 (2004).

[16] N. Taberlet, Ph.D. thesis, Université de Rennes I, 2005.

[17] D. van der Meer, K. van der Weele, and P. Reimann, Phys. Rev. E **73**, 061304 (2006).

[18] D. van der Meer, P. Reimann, K. van der Weele, and D. Lohse, Phys. Rev. Lett. **92**, 184301 (2004).

[19] D. van der Meer, K. van der Weele, and D. Lohse, Phys. Rev. E **63**, 061304 (2001).

[20] D. van der Meer, K. van der Weele, P. Reimann, and D. Lohse, J. Stat. Mech. (2007) P07021.

[21] F. Ludewig and N. Vandewalle, Phys. Rev. E **85**, 051307 (2012).

Chapter 6

Clustering and granular transport

In several industrial processes granular materials have to be transported from one fabrication step to another. In general, this transport can be achieved by conveyor belts (see figure 6.1), or vibrating screens. Obviously, in microgravity these techniques can't be used. A granular pumping seems to fit the need but the various security constraints linked to space experimentation render this method quite complicated. Another efficient method has to be developed in order to transport granular materials in microgravity.

Figure 6.1: (From XSM mining and construction) Photography of a gravel sand production line. The granular material is transported by conveyor belts and vibrating screens through the different production stages.

First of all, the grains have to be gathered which can be realized by a dynamical clustering whose conditions of existence are controlled via our theory [92]. Given the driving parameters in our previous studies, the granular agglomerate stabilizes always in the center (along the z axis) of the system. However, by using different amplitudes and frequencies of oscillations for the top and the bottom pistons, the position of the cluster may be modified. Accordingly, tuning these parameters during a simulation or an experiment would lead to a displacement of the grains and thus to a granular transport.

6.1   Motivations

In our two last studies we realized fundamental steps towards the handling of granular materials. Indeed, the formation of a dynamical cluster could be understood and its localization via a trapping mechanism has been realized. In the following article we propose an original way to

transport granular materials in microgravity using the clustering effect. We investigate numerically the dynamics of an asymmetrically driven granular gas and show that the vertical position of a dynamical cluster can be fully controlled via the amplitude ratio a. Moreover, we study the natural oscillations of a cluster around its equilibrium position and propose a theoretical model that captures the observed dynamics.

6.2   Numerical setup

The numerical setup is inspired by the cells of the SpaceGrains instruments. The container is rectangular and two pistons, separated by a distance L, stir up the enclosed granular material. The driving amplitudes of both pistons can by controlled separately and are noted A_h and A_c, referring to a hot and a cold boundary condition. The side length l of the container is chosen smaller than in previous studies in order to decrease the duration of the simulations. Indeed, in a thinner geometry, less grains are required in order to form a dynamical cluster. A sketch of the cell is given in figure 6.2. The positions of the top and the bottom pistons are noted $z_c(t)$ and $z_h(t)$ and their respective distances to the cluster are noted Δz_c and Δz_h. The thickness of the cluster is noted e.
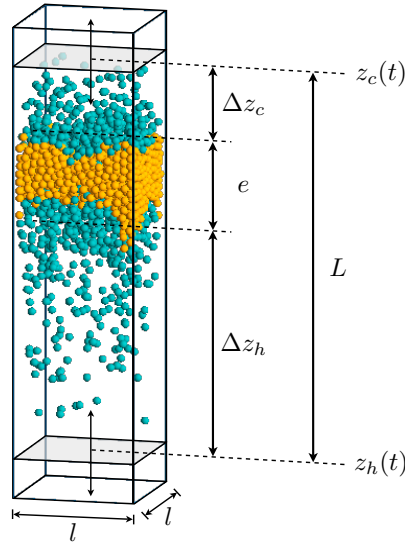
Figure 6.2: (Taken from [94]) Sketch of the simulated cell dedicated to the study of dynamical clustering under asymmetrical driving conditions. The positions of the top and the bottom piston are noted $z_c(t)$ and $z_h(t)$ in analogy to cold and hot boundary conditions. The length e denotes the thickness of the cluster.

6.3   Main results

We realized various simulations for different values of A_c and A_h and a constant number of particles. In each simulation a cluster is observed but its position depends on the amplitude ratio $a = A_c/A_h$. This behavior can be explain through a simple model. We suppose the cluster to be stabilized at a vertical position z_{cl}. In order to stay at this height, the momentums coming from the top and bottom pistons have to be equal and must reach the cluster simultaneously. If one considers that the gas surrounding the cluster is very dilute, no collision occurs between the

pistons and the cluster and the temporal criterion becomes

$$\Delta t_c = \frac{\Delta z_c}{A_c \omega} = \frac{\Delta z_h}{A_h \omega} = \Delta t_h. \tag{6.1}$$

Taking into account the size of the cluster in regards to the size of the entire system, the position of stabilization can be determined by following relation,

$$z_{cl} = \frac{L_g}{2} \left(\frac{1-a}{1+a} \right), \tag{6.2}$$

where $L_g = L - e$ is the clearance of the system as define in [83]. However, the cluster doesn't remain static at this position. Its center of mass oscillates around z_{cl} at a particular frequency noted ω_{cl}. In order to model these fluctuations we derive the total force that is applied to the cluster from the momentum rates that it receives. If the system is out of equilibrium, the obtained retraction force can be reduced to an harmonic oscillator with typical pulsation

$$\omega_{cl} = \left(\frac{A_c + A_h}{L_g} \right)^{3/2} \left(2 \frac{N - N_{cl}}{N_{cl}} \right)^{1/2} \omega. \tag{6.3}$$

where N_{cl} is the number of grains in the cluster. This pulsation depends only on the controllable driving parameters A_c, A_h and ω and on the cluster's dimension. Measuring ω_{cl} provides thus an interesting way to probe the size of a cluster.

6.4   Conclusion

Controlling the amplitude ratio of the piston's movements in a SpaceGrains like cell allows to modify the clustering position and thus the transport of granular material in this kind of geometry. This method is certainly not the most efficient but represents a potential application of our study. From a more theoretical point of view, our study allows us to determinate the natural pulsation of a dynamical cluster and to link it to its mass mN_{cl} and its size e. Reciprocally, the size of a cluster can be estimated via the measurement of w_{cl} without any manipulation of the granular material that would put a stop to the phenomenon.

Granular transport in driven granular gas

M. Noirhomme[1a], E. Opsomer[1], N. Vandewalle[1] and F. Ludewig[1]

GRASP, Physics Department B5a, University of Liège, B-4000 Liège, Belgium.

Abstract We numerically and theoretically investigate the behavior of a granular gas driven by asymmetric plates. The injection of energy in the dissipative system differs from one side to the opposite one. We prove that the dynamical clustering which is expected for such a system is affected by the asymmetry. As a consequence, the cluster position can be fully controlled. This property could lead to various applications in the handling of granular materials in low gravity environment. Moreover, the dynamical cluster is characterized by natural oscillations which are also captured by a model. These oscillations are mainly related to the cluster size, thus providing an original way to probe the clustering behavior.

PACS. 45.70.-n Granular systems – 05.45.-a Nonlinear dynamics and nonlinear dynamical systems – 05.45.Pq Numerical simulations

1 Introduction

Driven granular materials exhibit an intriguing collective behavior commonly known as dynamical clustering. Particles collide and loose energy which leads to the formation of slow and dense regions in the system [1, 2]. This particular behavior was studied experimentally in microgravity [3–7] and rationalized theorically and numerically [8–14].

Dynamical clustering is due to the competition between a characteristic dissipation time, called Haff time, and a characteristic time of energy propagation through the system [14–16]. Gravity would induce another characteristic time in the system and therefore affect dynamical clustering [17]. Low gravity condition is needed for the study of this phenomenon. This motivates the European Space Agency's (ESA) VIPGRAN project [18] in which granular gas will be experimentally investigated under various conditions on the International Space Station (ISS). Numerical work is essential to prepare the VIPGRAN project and to fix the experimental parameters.

The behavior and the stability of a granular cluster is poorly understood when the excitation parameters are changed. The main motivation of this article is to address the question of variable injection of energy in the system. The first step is to study the case of an asymmetric driving and to study the position of the cluster in the system. In the second step, the possible motion of the cluster will be analyzed. We will see in this paper that it is possible to control both position and motion of dynamical cluster, opening ways to achieved a granular transport in microgravity.

---

[a] *Present address:* mnoirhomme@ulg.ac.be
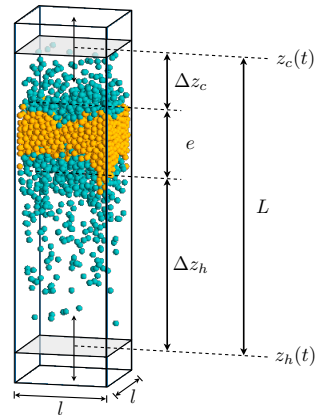
Figure 1: Sketch of the VIPGRAN cell used in simulations. Dimensions of this one are $L = 50$ mm and $l = 15$ mm. The oscillating plates have the following parameters: a common frequency fixed at $f = 5$ Hz and tunable amplitudes, A_c and A_h. The length L is measured between plate equilibrium positions. The relevant parameter is the amplitude ratio $a = A_c/A_h$.

2 Numerical approach

Numerical simulations are performed using a Molecular Dynamic (MD) algorithm, adapted to soft-matter physics [19]. The model is based on Newtonian mechanics [14, 20, 21]. At each collision, normal and tangent forces are evaluated respectively through particle deformations and tangential velocities. Moreover, the dissipation coefficient ε modeling the velocity loss is taken into account. A com-

plete description of MD simulation is given by Taberlet in [22] and was already used by the authors in [13, 14, 20, 21, 23].

Based on the VIPGRAN concept, we designed a box of width and depth equal to $l = 15$ mm. The length $L(t) = z_h(t) - z_c(t)$ is variable with the positions of the oscillating plates given by the following equations of motion

$$\begin{cases} z_h(t) = z_h^* + A_h sin(2\pi f t) \\ z_c(t) = z_c^* + A_c sin(2\pi f t + \varphi). \end{cases} \quad (1)$$

Opposite walls are oscillating with a fixed frequency $f = 5$ Hz and a phase shift $\varphi = \pi$ as proposed in the VIPGRAN project. The average distance between the plates at rest is $L = 50$ mm. The number of particles in the cell is fixed at $N = 2000$ to ensure clustering in the system [14]. The grains have a restitution coefficient and a radius fixed at $\varepsilon = 0.9$ and $r = 0.5$ mm respectively. The amplitudes A_h and A_c, with which the amplitude ratio $a = A_c/A_h$ is defined, and the phase shift φ have been modified. We choose to keep the frequency fixed at 5 Hz for both plates in order to change the intensity of the injected energies while keeping a constant time scale in the system from one simulation to another. In addition, the residual vibration of the instrument is minimized if the frequencies are the same for both walls. This fact is important in order to reproduce the simulated experiment in the VIPGRAN project. A sketch of the described cell is shown on fig. 1. Four campaigns of simulations have been realized. In the first three, we investigated the impact of the amplitude shift when the fourth was devoted to the phase's shift influence. We choose to fix the amplitude of the hot plate (the bottom ones on fig. 1) at $A_h = 5$ mm, 7.5 mm and 10 mm in the first, second and third campaign, respectively. The tunable parameter of the experiment was the amplitude ratio a and was firstly varied in the interval $\{0; \frac{1}{10}; \frac{1}{9}; \dots; 1\}$ and in the interval $\{0.2; \dots; 0.8\}$ in second and third runs. In the last ones, the amplitudes of both vibrating plates were set to $A_h = A_c = 5$ mm while the phase shift φ was varied in the interval $\{0; \frac{\pi}{4}; \dots; \frac{7\pi}{4}\}$. Table 1 gives a simplified view of the parameters used in the four campaigns. Each run corresponds to 300 periods of plates oscillation, requiring about 10^8 iterations of the algorithm.

Table 1: View of the variable parameters of the four runs of simulations.

Run	A_h (mm)	a	φ	Symbol
1	5	[0; 1]	π	🔴
2	7.5	[0.2; 0.8]	π	🟩
3	10	[0.2; 0.8]	π	🔺
4	5	1	$[0; 2\pi]$	▼

3 Results

Figure 2 presents the granular system in the cell for different amplitude ratios a. We first observe, as expected, the
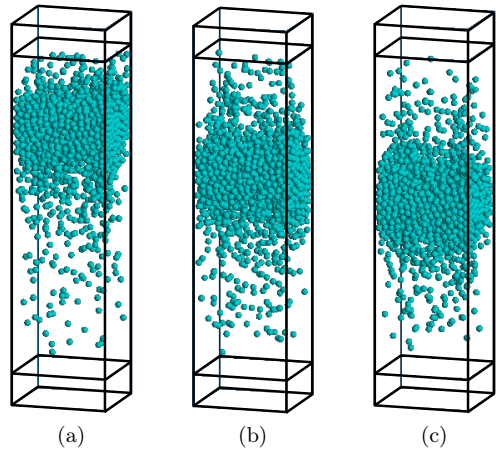

Figure 2: Three snapshots of the simulated experience for amplitude ratios $a = 0.25$ (a), $a = 0.5$ (b) and $a = 1$ (c). The cluster's position is directed by the value of a. The "hot" plate is always the bottom one.

formation of a dense region in the box where approximatively 95% of the grains are close together [13]. This low energetic region is separated from the plates by two dilute gases of particles which seem to transmit energy between the plates and the cluster. On fig. 2, one observes that the position of the cluster is a function of the amplitude ratio. Note that the more the amplitude ratio is small, the more the cluster is situated near the "cold" plate (i.e. the one with the smallest oscillation amplitude). A second observation we made is the oscillation of the cluster in the box. The position of the agglomerated grains is indeed not stable but makes a periodic motion with a pulsation very different from the plate's ones. These oscillations are shown on fig. 3 for three different amplitude ratios, corresponding to the cases (a), (b) and (c) of fig. 2.

The condensation behavior of the grains was already studied [14] and the new feature of driven granular gas investigated in this paper is the control of the cluster's position by amplitude tuning. This position, noted by z_{cl}, corresponds to the median of the particle's vertical positions. We observed that this quantity corresponds in good approximation to the densest region encountered in the cluster. For convenience, the z-axis is calculated from the center of the cell ($z = 0$) towards the cold plate.

Our simulations give evidence for an original behavior of driven granular media submitted to asymmetrically constraints in microgravity: a cluster is formed and is able to move in the cell and oscillates about its equilibrium position. Although the cluster is oscillating during long simulations, an average position, noted z_{cl}^*, can be calculated and linked to the amplitude ratio. Figure 4 gives this normalized average position for the first three campaigns. Note that the phase shift between both plates have no influence on the equilibrium position of the cluster and note again that the smaller is the amplitude ratio and the closer
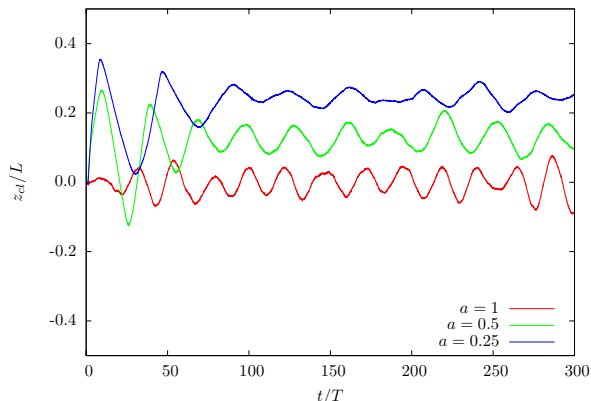
Figure 3: Dimensionless time evolution of the median of the distribution of the vertical position for amplitude ratios $a = 1$ (red), $a = 0.5$ (green) and $a = 0.25$ (blue). The median represents the cluster's position and is noted z_{cl}. The cluster is oscillating around an equilibrium position z_{cl}^* with a pulsation ω_{cl}. Both z_{cl}^* and ω_{cl} depend on the amplitude ratio a.

the grains condense to the cold plate, as already seen on fig. 2.

4 Cluster equilibrium position

To model the equilibrium position process in a simple way, we consider the cluster like a dense and stable pile of condensed grains receiving two momentum waves coming from both hot and cold plates. The model is based on two fundamental hypotheses: (i) the cluster has reached equilibrium and does not move anymore and (ii) the momentums coming from both hot and cold plates are sent after each period to the cluster, with the help of gaseous grains. Two conditions coming out of these hypotheses are also found. The momentums sent by the vibrating walls have to be equal and the time needed for each momentum wave to cross the cell have to be the same. Assuming that the number of particles contained in the cluster is constant (i. e. that the cluster captures as many grains as it loses through evaporation after a period of oscillation), we can model the cluster's equilibrium position. Our model considers that each grain coming from the plate $i = \{h, c\}$ has the typical velocity of the wall

$$v_i = A_i \omega. \qquad (2)$$

As discussed above, the equilibrium is reached when the time needed to attain the cluster is equal for both plates. Considering a straight and uniform movement of the grains, the time to cross the cell and to reach the cluster is directly linked to the plate-cluster distance by $\Delta t_i = \Delta z_i / v_i$. Equaling Δt_h and Δt_c, we find the following equilibrium condition

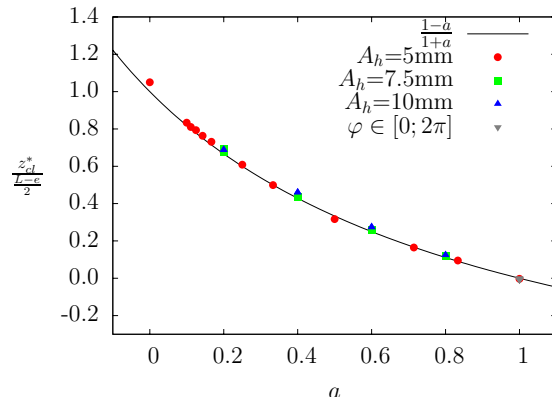$$\frac{\Delta z_c}{\Delta z_h} = \frac{A_c}{A_h}. \qquad (3)$$

Figure 4: Averaged and normalized equilibrium position z_{cl}^* of the cluster as a function of the amplitude ratio a. The equilibrium position is always measured from the center of the box to the coldest plate. Different symbols correspond to the four runs of simulations. The model developed in the main text is plotted using eq. (4) and is in excellent agreement with numerical results.

Taking into account the cluster thickness e along the z-axis, we can develop Δz_i in (3) in order to link it to the cluster's position z_{cl}. These distances are illustrated on the sketch of fig. 1. Using eq. (3) we find the cluster's equilibrium position

$$z_{cl}^* = \frac{L - e}{2} \left(\frac{1 - a}{1 + a} \right), \qquad (4)$$

where the dependence of the amplitude ratio a is obtained. The next step consists in finding the cluster's thickness e. For this purpose, we used an algorithm that measures the local density η around each sphere in the cell. Previous work [14] has shown that the cluster have approximatively local density larger than 0.285. Using this criterion, we defined the cluster's thickness by the maximal vertical distance that separates two particles with a local density $\eta \geq 0.285$. Measures were made on the entire simulation and averaged to finally find $e \approx 10$ mm, whatever the value of a. This result is not surprising since the excitation given by the oscillating plates is so intense that the cluster cannot be more compressed, even for the first campaign, making its size fairly constant. In fig. 4, we have plotted eq. (4) with this fixed value of e. The model is in excellent agreement with the results over the numerical campaigns.

5 Cluster oscillations

As discussed before and illustrated in fig. 3, clusters submitted to asymmetrical constraints are able to oscillate in the box around their equilibrium position z_{cl}^*. Note that the amplitude of these oscillations are significative in regards to the value of the cluster thickness e. Cluster inertia
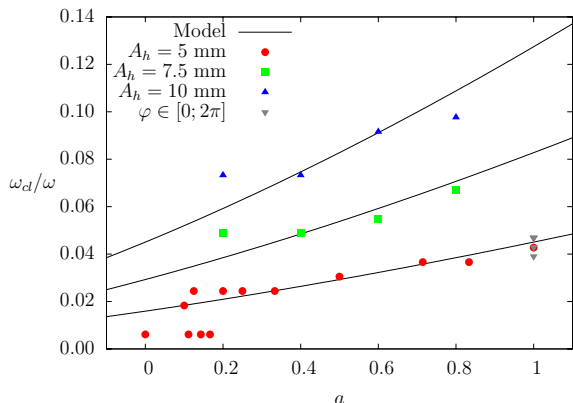
Figure 5: Normalized pulsation ω_{cl} of the cluster's oscillation as a function of the amplitude ratio a. The measures were performed with a Fast Fourier Transform (FFT) algorithm. The model described in the main text given by eq. (10) is in good agreement with the simulations. For small amplitude ratios, the algorithm was not always able to give relevant results because the oscillations of the cluster were too weak.

is given by the total mass $M_{cl} = N_{cl}m$, where N_{cl} is the number of grains of mass m contained in the cluster. According to our observations, this number of particles is roughly constant. In addition, we consider that the cluster interacts with moving planes with the help of both hot and cold gases that contain respectively N_h and N_c particles with N_h not necessary equal to N_c. These numbers of particles are together linked by the total number of grains injected in the box $N = N_{cl} + N_c + N_h$. However, within the granular gas, only a part of the particles $n_h < N_h$ and $n_c < N_c$ are colliding with the vibrating walls. They carry momentum towards the cluster. One has

$$\begin{cases} \Delta p_h = n_h m A_h \omega \\ \Delta p_c = n_c m A_c \omega. \end{cases} \quad (5)$$

Considering that the cluster's position is perturbed by δ, we can find an equation giving the momentum rate received by the cluster as a function of δ. momentum rates out of equilibrium can be decomposed into two parts corresponding to the oscillating plates:

$$\begin{cases} \dfrac{\Delta p_h}{\Delta t_h} = \dfrac{n_h(z_{cl}^* + \delta)m(A_h\omega)^2}{(L-e)/(1+a) + \delta} \\ \dfrac{\Delta p_c}{\Delta t_c} = -\dfrac{n_c(z_{cl}^* + \delta)m(A_c\omega)^2}{(L-e)a/(1+a) - \delta}. \end{cases} \quad (6)$$

In order to solve eq. (6), one has to evaluate the number of grains carrying momentums from the hot and the cold plates. Assuming that both hot and cold gases are uniformly distributed along the z-axis, $n_h(z_{cl}^* + \delta)$ and

$n_c(z_{cl}^* + \delta)$ are given by

$$\begin{cases} n_h(z_{cl}^* + \delta) = \dfrac{N_h A_h}{(L-e)/(1+a) + \delta} \\ n_c(z_{cl}^* + \delta) = \dfrac{N_c a A_h}{(L-e)a/(1+a) - \delta}. \end{cases} \quad (7)$$

From eqs. (6) and (7), the total force that acts on the cluster as a function of the perturbation δ is defined as

$$\begin{aligned} F(z_{cl}^* + \delta) =& \frac{N_h A_h^3 m \omega^2}{((L-e)/(1+a) + \delta)^2} \\ & - \frac{N_c A_c^3 m \omega^2}{((L-e)a/(1+a) - \delta)^2}. \end{aligned} \quad (8)$$

In order to find a theoretical value for the cluster's oscillation frequency, we linearized the force $F(z_{cl}^* + \delta)$ around the point z_{cl}^*. This linearization leads finally to

$$F(z_{cl}^* + \delta) \approx -\frac{2(1+a)^3 A_h^3 m(N_h + N_c)\omega^2}{(L-e)^3}\delta. \quad (9)$$

The equation giving the evolution of the perturbation δ is then reduced to a harmonic oscillator with a typical pulsation

$$\omega_{cl} = \left(\frac{A_c + A_h}{L - e}\right)^{3/2} \left(2\frac{N - N_{cl}}{N_{cl}}\right)^{1/2} \omega. \quad (10)$$

This pulsation is only function of a single free parameter which is the number of grains contained in the cluster. As a consequence, eq. (10) gives the natural frequency of the cluster even for symmetric energy injection. Moreover, the mass of the cluster could be evaluated by measuring this pulsation. Measures of ω_{cl} for different amplitude ratios were performed with a Fast Fourier Transform (FFT) algorithm and plotted on fig. 5. The data are fitted with the free fitting parameter N_{cl} using eq. (10) and are in good agreement with the model except for small values of a for which the oscillations of the cluster are too weak to be detected by the algorithm. A remarkable feature is that the fitting number of particles in the cluster was found to be equal to $N_{cl} \approx 1860$ for all campaigns. This result means that the dilute gases are composed of approximatively 140 grains, as observed in many simulations.

As seen from eqs. (4) and (10), the phase shift between the hot and cold plates should have neither influence on the equilibrium position nor on the pulsation of the cluster. These results are expected because the models are both based on a momentum balance over one period of oscillation. If the amplitudes and the frequencies of the walls are unchanged, momentums coming from these ones have do not differ with another phase shift. The fourth campaign that was devoted to the phase shift influence has confirmed this fact.

Finally, notice that such oscillations of granular materials have been recently reproduced numerically under gravity by Rivas *et al.* [24]. The authors have performed simulations of a vibrated granular media composed of particles confined in a quasi-one-dimensional system. In this

case, low frequency oscillations of the media have been observed. If the behaviors are similar, some differences have to be highlighted. First, Rivas *et al.* have been able to describe theoretically their observations with a continuum model. In our work, the granular gases observed are so dilute that this way is not relevant. Secondly, the authors have seen that when more energy is injected, the frequency of cluster oscillations becomes smaller. We observed exactly the inverse. The simplest explication is found in the nature of the movements observed. In the gravitational open environment of the authors, the energy given to the cluster determines its parabolic flight, which increases with initial energy of the body. The time of flight of the cluster increases also with the initial energy injected. It is not the case in our closed system under microgravity where the cluster adopts a straight and uniform motion. The time to cross a determined distance is then so small that the kinetic energy of the moving cluster is intense. Surprisingly, the existence of a periodic collective motion is not only observed under gravity field but also in microgravity environment, although the nature of these motions are different.

6 Application to granular transport

The above results suggest that it is possible to create and control grain displacements in microgravity. In order to prove this concept, we propose a system inspired by Maxwell's demon [23, 25] and granular ratchets [26–29] for generating granular transport in low gravity environment. Several cells with independent pistons are placed in a row. Specific apertures at different heights allow a granular exchange between neighboring cells. By controlling the amplitude ratio of the independent pistons it is possible to drive the cluster in a selected cell. Figure 6 shows a simulation of a directed grains experiment. Three boxes are placed together and connected with two slits placed at different heights. The simulation starts with all the grains in the central cell (fig. 6 a). The amplitude condition in the central cell drives the cluster in front of the first slit, while in the first cell the amplitude ratio is inverted in order to drive the incoming cluster at the bottom of the cell. After a while, most of the grains are trapped at the bottom of the first cell (fig. 6 b). Then, the amplitude ratios are adjusted in all cells in order to drive the cluster from the left to the right cell. Note that no intermediate cluster is observed in the central cell (fig. 6 c) but that the grains directly gather in the right cell (fig. 6 d). We performed different simulations with different numbers of cells and similar behaviors have been found. By inverting the amplitude ratios, the granular transport is reversible.

7 Conclusion

In this paper, a study of the behavior of a dynamical cluster of grains excited by an asymmetrically constraint was performed with the help of Molecular Dynamics. A model

(a) $t = 3.2$ s (b) $t = 48$ s

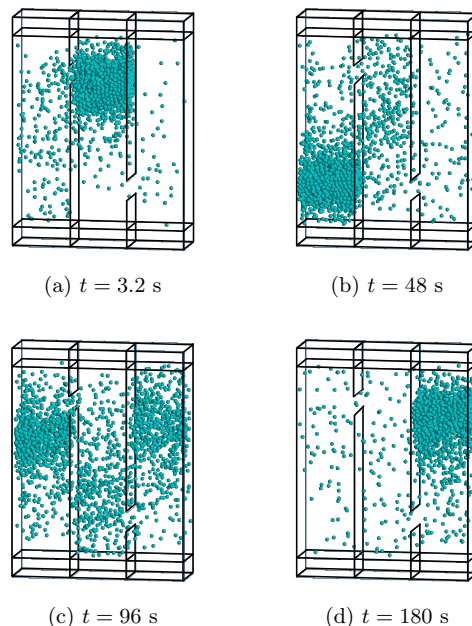(c) $t = 96$ s (d) $t = 180$ s

Figure 6: Snapshots of a directed grains simulation. The simulation starts with all the grains in the central cell (a). The amplitude condition in this one drives the cluster in front of the first slit, while in the first cell the amplitude ratio is inverted in order to drive the incoming cluster at the bottom of the cell. After a while, most of the grains are trapped at the bottom of the first cell (b). Then, the amplitude ratios are inverted in all cells in order to drive the cluster from the left to the right box. No intermediate cluster is observed in the central cell (c) but the grains directly gather in the right one (d).

was developed in order to link both cluster's position and cluster's oscillations to the amplitude ratio. The natural frequency of a dynamical cluster has been emphasized and could be used to estimate the mass of the cluster. The model provides a way to produce granular transport as checked in our simulations.

References

1. Goldhirsch I. *and* Zanetti G., Phys. Rev. Lett. **70**, (1993) 1619.
2. Kudrolli A., Wolpert M. *and* Gollub J. P., Phys. Rev. Lett. **78**, (1997) 1383.
3. Maaß C. C., Isert N., Maret G., *and* Aegerter C. M., Phys. Rev. Lett. **100**, (2008) 248001.

4. Hou M., Liu R., Zhai G., Sun Z., Lu K., Garrabos Y, *and* Evesque P., Microgravity Sci. Technol. **20** (2008) 73.

5. Falcon E., Wunenburger R., Evesque P., Fauve S., Chabot C., Garrabos Y. *and* Beysens D., Phys. Rev. Lett. **83** (1999) 440.

6. Falcon E., Aumaître S., Evesque P., Palencia F., Lecoutre-Chabot C., Fauve S., Beysens D. *and* Garrabos Y., Europhys. Lett. **74** (2006) 830.

7. Falcon E., Bacri J.-C. *and* Laroche C., Europhys. Lett. **103** (2013) 64004.

8. Olafsen J. S. *and* Urbach J. S., Phys. Rev. E **60** (1999) R2468.

9. Brilliantov N. V. *and* Poschel T., Europhys. Lett. **74** (2006) 424.

10. Javier Brey J., Moreno F., Garcia-Rojo R. *and* Ruiz-Montero M. J., Phys. Rev. E **65** (2001) 011305.

11. Zhou T., Phys. Rev. Lett. **80** (1998) 3755.

12. Li Y., Hou M. *and* Evesque P., J. Phys. Conf. Ser. **327** (2011) 012034.

13. Opsomer E., Ludewig F. *and* Vandewalle N., Phys. Rev. E **84** (2011) 051306.

14. Opsomer E., Ludewig F. *and* Vandewalle N., Europhys. Lett. **99** (2012) 40001.

15. Grasselli Y., Bossis G. *and* Goutallier G., Europhys. Lett. **86** (2009) 60007.

16. Aumaître S., Farago J., Fauve S. *and* Mc Namara S., Eur. Phys. J. B **42** (2004) 255.

17. Mc Namara S. *and* Falcon E., *Lecture Notes in Physics* (Springer, 2003) 341.

18. European Space Agency's VIPGRAN project. URL: http://www.spacegrains.org/.

19. Cundall P.A. *and* Strack O.D.L., Geotechnique **29** (1979) 47.

20. Ludewig F. *and* Vandewalle N., Phys. Rev. E **85** (2012) 051307.

21. Ludewig F., Dorbolo S., Gilet T. *and* Vandewalle N., Europhys. Lett. **84** (2008) 44001.

22. Taberlet N., PhD Thesis, University of Rennes, 2005.

23. Opsomer E., Noirhomme M., Vandewalle N. *and* Ludewig F., Phys. Rev. E **88** (2013) 012202.

24. N. Rivas, S. Luding *and* A. R. Thornton, New J. Phys. **15** (2013) 113043

25. Eggers J., Phys. Rev. Lett. **83** (1999) 5322.

26. van der Meer D., van der Weele K. *and* Reimann P., Phys. Rev. E **73** (2006) 061304.

27. Liu R., Li Y. *and* Hou M., Phys. Rev. E **79** (2009) 052301.

28. Hou M., Li Y., Liu R., Zhang Y. *and* Lu K., Phys. Status Solidi A **207** (2010) 2739.

29. van der Meer D., Reimann P., van der Weele K. *and* Lohse D., Phys. Rev. Lett. **92** (2004) 184301.

Chapter 7

Clustering and segregation

The handling and manipulation of granular materials can provoke the segregation of its different components. Depending on the size, the mass or the form of the particles an organization takes place within the granular media. A typical example of this behavior is the Brazil Nut Effect (BNE) presented in the introduction. When a heterogeneous mixture of grains is vertically vibrated, the large particle rise upward to the surface of the granular fluid. The latter phenomenon is linked to several processes taking place in the granular pile. When a large grain takes off, because of the driving acceleration, the hole that is left behind is filled by smaller grains which is not possible the other way around. Moreover, the driving induces convection rolls in the system. An important upward stream appears in the center of the cell and drags the large particles to the top of the pile. If these particles are larger than the thin downward streams at the borders of the cell, they remain at the surface. Recent studies [57] have shown that gravity has a great impact on the BNE and on segregation phenomena in general. However, the subject is still relatively unexplored and only few experimental data is available. Figure 7.1 presents a sketch of a driven mono disperse granular system (gray particles) in which an intruder (red particle) has been placed. Convection rolls are described by blue an red arrows.
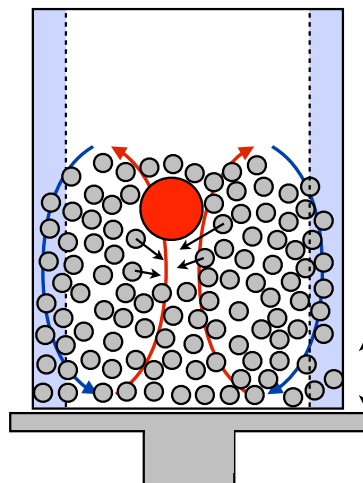

Figure 7.1: Sketch summarizing the different processes that lead to the Brazil Nut Effect (BNE). Differences between the sizes of the particles and convection rolls, lead to the rise of larger grains to the surface of the system.

7.1   Motivations

Given the lack of information concerning the segregation in granular media under microgravity conditions, the study of poly-disperse granular gases in the SpaceGrains project seems of great interest. In order to explore these kind of phenomena two different sizes of particles can be used in the instrument. However, since both particle types are made of the same material (bronze), changing the sizes of the particles will also change their masses. In the following article, two series of simulations were performed. In a first one, we studied numerically the impact of both mass and size of the particles separately. In a second one, we realized a deeper investigation of a SpaceGrains like system using bronze particles.

7.2   Setup for SpaceGrains

The realization of an experiment concerning the segregation of bi-disperse granular material doesn't require any specific modification of the traditional granular gas cell. The latter is filled with a number N_S of small and N_L of large particles. For this study the driving parameters as well as the distance L can be fixed in a first attempt so that only the couple (N_S, N_L) can be tuned in order to observe the phenomenon. Figure 7.2, taken from [95], represents a sketch of the cell filled with both types of grains (large ones in blue and small ones in green).
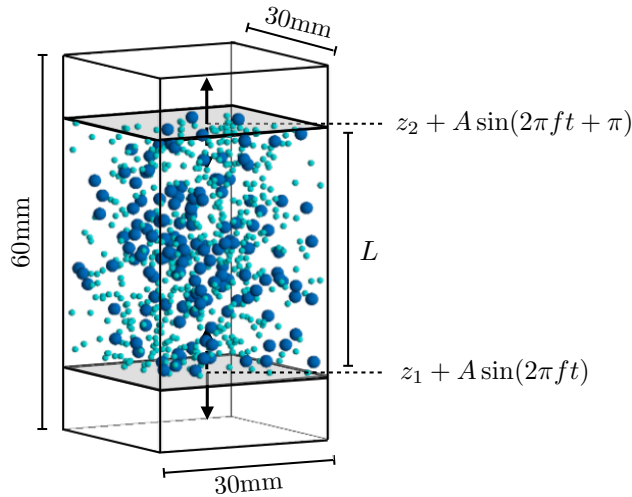

Figure 7.2: (Taken from [95]) Sketch describing the cell dedicated to granular gases in the Space-Grains instrument filled with two different particles species.

7.3   Main results

In a first preliminary study, the impact of mass and size differences between both granular species on the system's dynamics has been investigated. For this purpose three typical setups were simulated. For each setup the granular mixture was driven until a steady-state was reached and the segregation was evaluated via the PDF of the particles' positions. In setup A, where the grains are of same size but of different mass, one observes a concentration of heavy particles in the center of the cell. A cluster forms and is surrounded by a gas of light grains. In setup B, where the grains have the same mass but different sizes, it is the small particles that gather in the center of the cell while the large ones form the gaseous phase. Setup C corresponds to particles from the SpaceGrains project, accordingly they differ in both, mass and size. This results in a combination of the phenomena observed in A and B. Indeed, the heavy particles cluster rapidly in the center of the cell. However, for high fillings, the size effects seem to become more important than the

mass effects and the small particles migrate also toward the center of the system. At this point it is important to note that clustering and segregation always appear together.

In a second series of simulations, the setup C has been deeply investigated in order to prepare a possible experiment for SpaceGrains. An entire phase diagram (see figure 7.3) is obtained by varying N_S and N_L. The transitions between the different cluster regimes are obtained via a statistical test. One can note that the clustering of a pure system of large grains can never be achieved. However, adding small grains to the mixture leads to a gathering of the large ones and thus to segregation. Moreover, we adapted the theoretical model that predicted the apparition of clusters in a mono-disperse system [92] to a bi-disperse one. Theory and collected data are in excellent agreement.
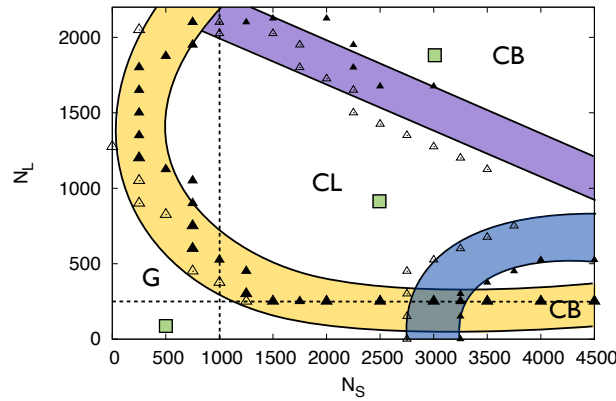
Figure 7.3: (Taken from [95]) Phase diagram summarizing the different observed clustering regimes in the system: granular gas (G), cluster of large particles (CL), cluster of both particle species (CB). Triangle symbols correspond to the measured transition points. Colored shadings are visual guidelines.

7.4 Conclusion

We investigated numerically the possibility of segregation in bi-disperse granular materials within the frame of the SpaceGrains instrument. The impact of the sizes and the masses of the particles has been studied and different cluster-segregation regimes have been observed. We realized a complex phase diagram depending on the filling numbers of both granular species. The corresponding data can be used to fix parameters for the future experiment. Finally, our study proposes an ingenious way to sort out particles in microgravity which is not only of scientific but also of industrial interest [96, 97].

Clustering and Segregation in Driven Granular Fluids

E. Opsomer[1], N. Vandewalle[1], M. Noirhomme[1], and F. Ludewig[1]

GRASP, Physics Department B5a, University of Liège, B-4000-Liège, Belgium.

Abstract In microgravity, the successive inelastic collisions in a granular gas can lead to a dynamical clustering of the particles. This transition depends on the filling fraction of the system, the restitution of the used materials and on the size of the particles. We report simulations of driven bi-disperse gas made of small and large spheres. The size as well as the mass difference implies a strong modification in the kinematic chain of collisions and therefore alters significantly the formation of a cluster. Moreover, the different dynamical behaviors can also lead to a demixing of the system, adding a few small particles in a gas of large ones can lead to a partial clustering of the taller type. We realized a detailed phase diagram recovering the encountered regimes and developed a theoretical model predicting the possibility of dynamical clustering in binary systems.

PACS. 45.70.-n Granular systems – 05.45.-a Nonlinear dynamics and nonlinear dynamical systems – 05.45.Pq Numerical simulations

1 Introduction

Granular materials present a large diversity of spectacular phenomena [1, 2]. Compaction [3–5], arch formation [6–8] and non-Newtonian behaviors [9,10] are only a few examples. When energy is continuously injected into the system containing granular material, the latter is fluidized and presents a gas like behavior that has been studied intensively during the last decades [11–13] as well in two- [14–17] as in three dimensional systems [18–20]. However, the granular gas is different from a classical gas: velocities do not follow a Maxwell-Boltzmann distribution [21–25] and the usual thermodynamical gas models cannot be applied directly [26,27]. Being a paradigm of dissipative systems, driven granular media tends to dissipate the mechanically injected energy through multiple inelastic collisions. Eventually, the system "cools down" locally and dense regions of low mobility appear. These regions are the result of the energetic equilibrium in the system and are the signature of a stationary regime known as dynamical clustering [28, 29]. The formation of such dynamical clusters can be linked to three essential factors: the restitution coefficient ε, the packing fraction ϕ and the particle radius R in regards to the typical length scale δ of the system. Our previous work [30] presented a theoretical model, based on these parameters, that gives an accurate criterion for the upcoming of the phenomenon.

Since the size of the driven particles has a fundamental impact on the dynamics of the system, it is of wide interest to study the behavior of driven polydisperse granular materials. Indeed, the chains of collisions that typically occur when the pistons inject energy into the system are dramat-

ically modified. A large grain could collide simultaneously several smaller ones and so be slowed down considerably. Moreover, the difference of mass between particles leads to a more complex transfer of momentum than in the monodisperse case. The geometric characteristics of the particles could also lead to segregation phenomena. For instance, shaking vertically a container filled with grains of different sizes generates an uprise of the large bodies. This demixing, commonly called the Brazil Nut Effect, has been studied intensively [31–33] and recent research [34] has investigated the impact of gravity on the phenomenon. Note that mass differences can also create similar effects [35]. In order to study this wide field of behaviors presented by driven granular materials, the European Space Agency (ESA) has programmed a series of experiments in complete weightlessness, called SpaceGrains [36] that will take place in a near future.

Given the fundamental interest and the need of predictive results, we decided to explore numerically the complex dynamics of driven bidisperse granular media in the frame of a particular experimental cell. We analyze, the impact of size and mass variations between particles on the dynamics of the system. Dynamical clustering is observed and the theoretical gas-cluster transition curve for a monodisperse media [30] could be adapted. Finally, complex segregation phenomena appear for divers sets of parameters. Our results are promising and contribute to a deeper comprehension of the clustering. Moreover they provide ways to manipulate the granular media and to sort out particles within the frame of SpaceGrains or other later space missions.

2 Numerical approach

We choose to simulate an experimental setup of ESA's future SpaceGrains experiment that is dedicated to the study of convection and segregation. For this purpose, a binary mixture of spherical particles is enclosed in a cell of dimensions $60 \times 30 \times 30$ mm^3, as represented in figure 1. To ensure the driving of the granular material, two pistons
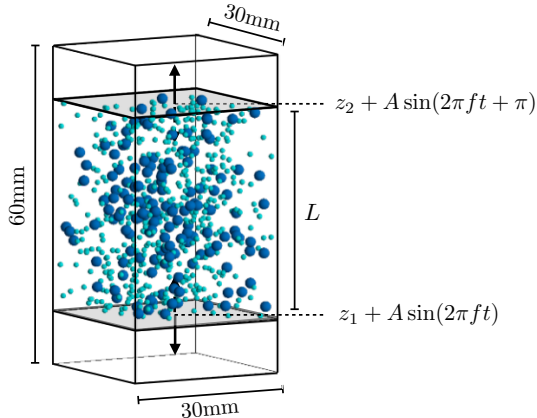

Figure 1. (colors online) Sketch of ESA's SpaceGrains cell. Particles are enclosed in a $60 \times 30 \times 30$ mm^3 box. Two pistons are oscillating in phase opposition with an amplitude $A = 5$ mm and a frequency $f = 10$ Hz around their respective positions z_1 and z_2. The average distance between the pistons $L = |z_2 - z_1|$ is fixed to 40 mm.

are oscillating in phase opposition with an amplitude A and a frequency f around their positions of equilibrium z_1 and z_2. We define the origin of the z-axis at the center of the cell, in the middel of $|z_1 z_2|$. The distance L between z_1 and z_2 can be tuned in order to modify the accessible volume of the system but will be fixed to 40 mm in our case. The width of the cell is noted l and is 30 mm.

Our simulations rely on a Molecular Dynamics (MD) algorithm. This numerical model is broadly used in the simulation of granular materials [37,38] and has been validate through the two last decades. The normal forces are evaluated via a linear spring-dashpot model. Dissipation is taken into account by viscous forces that are function of the normal velocity of the contact point and the restitution coefficient ε. It is to note that we use the same value of ε for both, grain-grain and grain-wall collisions. The tangent forces are bounded according to Coulomb's law and depend on the relative tangent velocities as well as the coefficient of friction μ between the colliding solids. Further details are given in previous works [19,30] and a complete description of this MD approach is given by Taberlet [39].

3 Mass and size effects

In the SpaceGrains experiment, the granular media is composed by two types of bronze spheres with respective radii

of 0.5 and 1 mm. It is important to note that this difference in size between the particles also induces a difference in mass. Accordingly, the observed effects while driving the mixture cannot be linked properly to either one of those parameters. In order to study their individual influence we work with three particular setups (A,B,C) involving four different types of grains. Each type is described in table 1 and will be referred in the latter by its corresponding symbol or number. In order to observe and to detail first phenomena, we investigated the system for fillings N ranging in between 500 and 4000 grains. In each simulation, the granular material is composed by two particle types of equal concentration and is driven during 10 seconds. Note that for all runs, we fixed the values of $\varepsilon = 0.9$ and $\mu = 0.7$.

type	r (mm)	ρ (kg/dm^3)	Setup	Symbol
1	0.5	2.5	A	○
2	0.5	8	A,B,C	●
3	1.0	1	B	◯
4	1.0	8	C	⬤

Table 1. Parameters for the different simulated particle types. Symbols are given according to the results presented in following figures. The forth column describes in which study the concerned species is implied.

The presence of dynamical clustering and segregation in the system can be highlighted by the Probability Density Function (PDF) of the positions of the grains. On the one hand, gas-like systems present distributions close to uniform laws since the granular material is spread evenly through the entire cell. On the other hand, the distributions of each particle type can be compared one to another in order to detect a demixing of the system. A summary of the encountered behaviors is given in figure 2 that presents the results for the setups A, B and C for $N \in [1000, 4000]$ according to the symbols in table 1. Depending on the components of the granular mixture and the number of particles, different dynamical behaviors are reported:

3.1 Setup A: Grains of same sizes but different masses

When a mixture of granular types 1 and 2 is driven, several dynamics can be encountered depending on the filling of the system. Indeed, by analyzing the distributions of both species, severe differences appear as one can note in the top row of figure 2. For a diluted case, both distributions are typical for a system in a gas regime since particles can be found everywhere in the system with roughly the same probability. In denser cases, one can assist to a migration of the heavy grains towards the center of the cell. Accordingly, their distribution is much more peaked about 0 than for the light particles. A similar phenomenon is encountered in rotating drums where the denser particles travel to the core of the system [35]. This behavior simply corresponds to a minimization of the kinematic energy in the systems. Please note that the segregation goes hand in
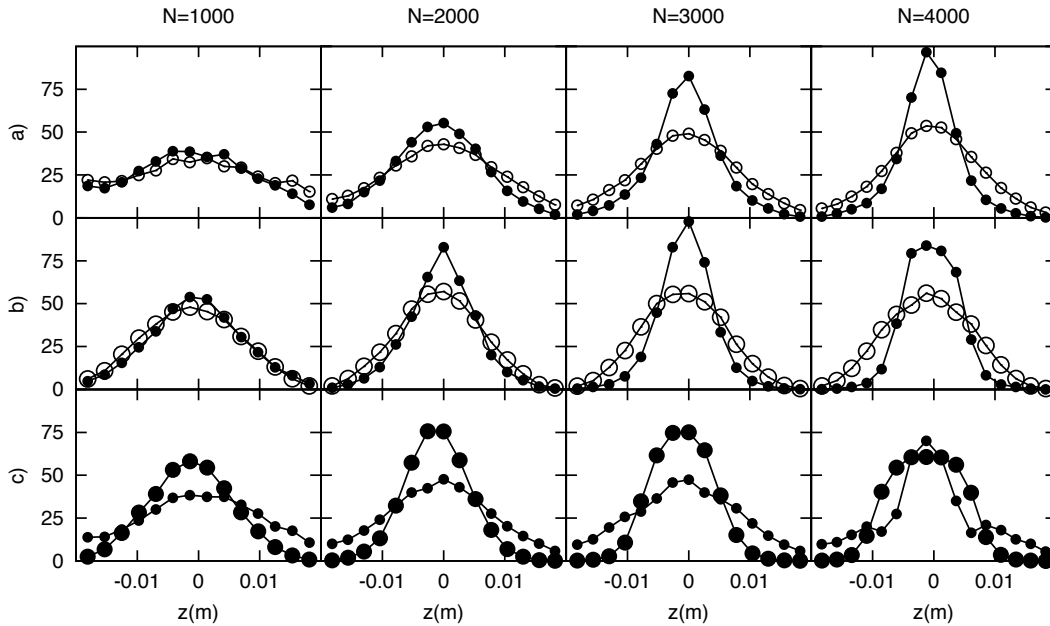
Figure 2. Particle Density Function for the three presented driven mixture of granular material. Large dots stand for large particles and filled dots for heavy ones. *a*) For grains of identical size, heavy particles gather in the central part of the cell and form a cluster once the filling is high enough. *b*) If both particles types are of identical mass, increasing N leads to a cluster of small grains. *c*) If mass and size are different, one can observe the gathering of the large particles as well as a particular clustering of both species for large N.

hand with the formation of a dynamical cluster of heavy particles that coexists with a granular gas of light ones.

3.2 Setup B: Grains of same masses but different sizes

By considering the difference of density between the particles of type 2 and 3, mass will play no more role in the grain-grain interactions and only geometric parameters as cross section and volume will influence the dynamics of the system. Like in case A, the distribution of both particle types depend on N as presented in the central row of figure 2. For low fillings, both curves are close one to another. However, they are not as horizontal as expected for a gas. This tendency to concentrate in the center of the system is the signature of the dynamical clustering effect. Indeed, since the granular type 3 has a radius that is twice as large than the radius of type 2, the global packing fraction of the system increases dramatically. Accordingly, for the same total number of grains this setup corresponds to a denser system than the first one. For larger fillings, the distribution of the small grains presents a wide peak in the central region while the large grains spread like in the gaseous case. Both particle types have segregated and one observes a dynamical cluster of small grains surrounded by a gas of large one. Once again, this is the most favorable configuration in terms of kinematic energy. Indeed,

given their important cross section, the large particles are slowed down more efficiently than small ones.

3.3 Setup C: Grains of different sizes and masses

Since the particles are made of the same material, both, the mass and size effects can lead to segregation. It is interesting to note that the effects presented in the setups A and B will counteract in this third version since the largest spheres are also the heaviest. We realized simulations with a mixture of particles of type 2 and 4 and the corresponding distributions are represented in the bottom row of figure 2. In opposite to both previous cases, the dilute system presents already a slight difference in the distributions of the small and the large grains. At this state one cannot speak properly of segregation. Nevertheless, it seems that the heavy particles are more likely to be found in the central region of the cell. This behavior can be explained with regards to the setup A. Indeed, in a dilute system, the interaction between particles is low and thus the mass effects overtake the size effects. Increasing the number of particles leads to a more stressed difference between both distributions. Segregation and clustering are observed simultaneously. However, above some critical packing fraction, small particles are also likely to be found in the center of the system. Indeed, in this region,

the local density is high and accordingly the size effects become important compared to the mass effects. As in setup B, this configuration leads to a gathering of the small grains in a central region. The system is finally composed by a dense cluster of small and large grains surrounded by a gas of small particles. Consequently, the system is no longer segregated.

4 Phase diagram

From now on, we will focus on the setup designed for the SpaceGrains project. The parameters of the system correspond to what has been presented in the subsection C. However, the number of small and large spheres, noted respectively N_S and N_L can be tuned independently. We realized 150 predictive simulations for couples (N_S, N_L) ranging in the interval $[0, 4500] \times [0, 2100]$ in order to establish a phase diagram recovering the encountered dynamics. Each simulation starts with independent initial conditions. Figure 3 gives an overview of the three typical regimes that are observed. From left to right, one can see a gas phase (G), a cluster of only large particles (CL) and a cluster composed by both particle types (CB).

Figure 3. (Colors online) Overview of three typical regimes that are observed. From left to right on can see a gas phase (G), a cluster of only large partic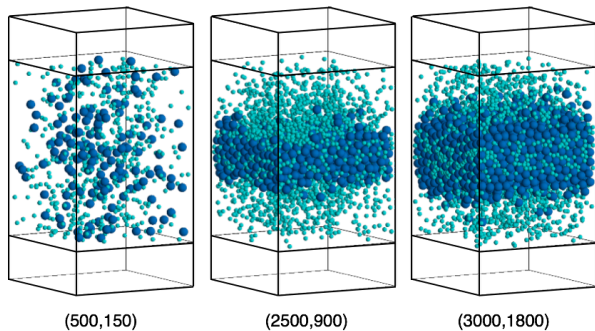les (CL) and a cluster composed by both particle types (CB). Couples of numbers correspond respectively to N_S and N_L.

The detection of each regime can be realized via two Kolmogorov-Smirnov (KS) tests [19], evaluating the uniformity of the distributions of small and large grains along the z axis of the system. Both granular types are tested separately starting with a null hypothesis H_0 of uniformity that correspond to the gas regime. If H_0 is rejected, what we note H_1, the system can no longer be considered to be homogeneously distributed and is qualified as clustered. In addition to this statistical criterion, we also impose a minimum size of one granular layer to a cluster. This last condition verified, the following table summarizes any possible outcome of the tests:

Applying the above detection method to all our simulations, allows us to define the frontiers between the encountered dynamical regimes and to place them on a (N_S, N_L)

Dynamical regime	Small	Large
(G) gas phase	H_0	H_0
(CL) cluster of only large particles	H_0	H_1
(CS) cluster of only small particles	H_1	H_0
(CB) cluster of both particle types	H_1	H_1

Table 2. Possible outcomes of the Kolmogorv-Smirnov test comparing the particle distributions against a uniform law. H_0: the null hypothesis can't be refuted, the corresponding distribution is accepted as uniform. H_1: the null hypothesis is not valid, the concerned granular type presents a spatial inhomogeneity (*i.e.* clustering).

phase diagram. Figure 4 describes with small (resp. large) triangles the detected transition points relative to the clustering of the small (resp. large) particles. Dashed lines give the minimum cluster sizes, hollow triangles correspond to a KS test with a level of significance $\alpha = 0.05$ and filled to $\alpha = 0.01$. Taking account of the dispersion of these points, three transition zones can be obtained. Consequently, the diagram is divided into four subsections corresponding to the different regimes of the system. G is found in the lower left corner of the diagram. CL is present for wide ranges in the centre of the diagram. However, in our configuration, it cannot exist in a pure system so that the presence of small particles is necessary. On the contrary, CS is only present in a pure small grains system for $N_S > 3250$. Finally, CB comes up even twice. The upper part corresponds to a cluster of large particles surrounding a cluster of small ones whereas the lower part consists in a cluster of mainly small grains containing locally some large ones. The grey (green) squares correspond to the simulations presented in figure 3. A closer look on this diagram highlights two intriguing transitions. Starting with a small number of large particles and adding more and more small ones into the cell will lead to a dynamical clustering of the large grains. Accordingly, injecting gaseous, hot, granular material into the system will cool it down. Starting with a pure cluster of small particles and adding large ones has the opposite effect. First, both granular types contribute to the cluster but once enough large grains are present, most of the small ones are forced into the surrounding gas phase. In this configuration, adding cold granular material in the system will warm it up.

As mentioned in the previous section, the formation of CL leads to a demixing of the system. In order to validate this assumption we measured the segregation intensity I_s proposed by Windows-Yule *et al.* [40] in the constrain free zone of our system. As expected, the highest values are obtained in the region corresponding to a cluster of large particles. Considering the latest interest of international space agencies and private companies in a possible mining of asteroid and other near-Earth objects [41, 42], the understanding as well as the control of segregation in microgravity is of broad interest. Note that, in opposite to traditional methods as sieving or sedimentation, we achieve to separate different grain species without the help of gravity or buoyancy.
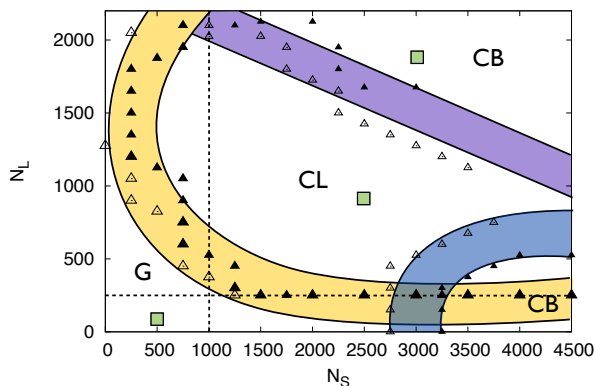
Figure 4. (Colors online) Phase diagram describing the different dynamical regimes of the system. Shaded frontiers zones recover the transition points that are detected according to our statistical and geometrical criteria. Dashed lines give the minimum cluster sizes. Simulations corresponding to figure 3 are represented by grey (green) squares.

All the transition lines presented in figure 4 are guidelines for the eyes. Nevertheless, in the following section we develop an integrative model allowing us to describe the gas-cluster transition.

5 Modeling the transition

According to our previous work [30], the formation of a dynamical cluster is strongly linked to the balance between the energy propagation and the energy dissipation during a period of excitation. The energy injected by the pistons, stirs up the granular material and therefore fluidizes the system. On the contrary, the successive collisions between particles lead to a loss of energy and a collapse of the granular gas. Depending on which behavior is dominant, the system is rather in a gas or a cluster regime. In order to determine the impact of these different mechanics, we compared the two typical timescales of the system *i.e.* the Haff time τ_H, which characterizes the cooling of the system [43] and the energy propagation time τ_P. Given the poly-dispersity of the granular media, it was not possible for us to obtain an analytical expression for τ_P. Nevertheless, we could evaluate the edge between the gas and the cluster regime by numerical integration.

A grain that travels from one side of the cell to the other realizes on average a displacement δ. The number of collisions n that this grain will encounter can be derived from the filling of the system,

$$n = \frac{N_S}{N}\left(\gamma_{SS}\eta_S + \gamma_{SL}\eta_L\right) + \frac{N_L}{N}\left(\gamma_{LS}\eta_S + \gamma_{LL}\eta_L\right), \quad (1)$$

where η_S (reps. η_L) is the number density of the small (reps. large) particles and $\gamma_{ij} = \pi\delta(R_i + R_j)^2$ is the effective collisional volume for a grain i colliding with a grain j. The energetic transfer through the system can then be

seen as a dissipative chain reaction between $n + 1$ grains and the Haff time can be defined by

$$\tau_H = \frac{2\delta}{v_0(1 - \varepsilon^2)n}, \quad (2)$$

where $v_0 = 2\pi Af$ is the typical velocity of the grains. Mechanical energy coming from the pistons is also injected into the granular material via those collisions. If the energetic impulses have enough time to travel across the granular whole media and to fluidize it, the system remains in a gas like state. In order to estimate this propagation time, we generate a random chain of $n + 1$ particles in which the proportion N_S/N_L is roughly the same as in the entire system. The first particle of the chain takes off with a starting velocity v_0. Then, each collision will modify the velocity of the carried impulse by taking into account the coefficient of dissipation ε and the masses m_i and m_{i-1} of the two successive impacting grains. The following relation is obtained,

$$\tau_P = \sum_{i=0}^{n} \frac{\ell_i - cr_i}{v_i}, \quad (3)$$

where

$$v_i = v_0\frac{m_0}{m_i}\varepsilon^i. \quad (4)$$

The corrective term cr_i, with $c = 1.654$, takes account of the finite size of the system in regards to the radius r_i of the particles [30]. The distance ℓ_i is the mean free path between the ith and the $(i + 1)$th collisions and can be defined as following,

$$\ell_i = r_i\delta\left(\sum_{j=0}^{n} r_j\right)^{-1}. \quad (5)$$

Note that for a mono-disperse case $\ell_i = \delta/n$ for all i.

Using the latter method a thousand times for each couple (N_S, N_L), the average timescales $\bar{\tau}_P$ and $\bar{\tau}_H$ are obtained and the transition is possible once their ratio $\tau = \bar{\tau}_P/\bar{\tau}_H > 1$. Indeed, in this configuration the systems cools down faster than the granular media is fluidized and consequently a cluster is formed. The transition curve can be visualized on figure 5 by plotting iso-τ curves on the (N_S, N_L) phase diagram. The red region corresponding to $\tau \in [1, 3]$ is in good agreement with our previous measures concerning the gas-cluster transition. Indeed, the transition points between the G regime and any cluster state, which represented by square symbols, lay all in the predicted region. Once again hollow symbols ($\square$) correspond to a KS test with a level of significance $\alpha = 0.05$ and filled ($\blacksquare$) to $\alpha = 0.01$. The small differences and the width of the transition zone can be explained by the fact that $\tau = 1$ is a minimum criterion based on a mean field theory meanwhile only one MD simulation was realized per (N_S, N_L) couple. Nevertheless, one can note that the model recovers the fact that CL cannot be observed in a pure system of large particles.
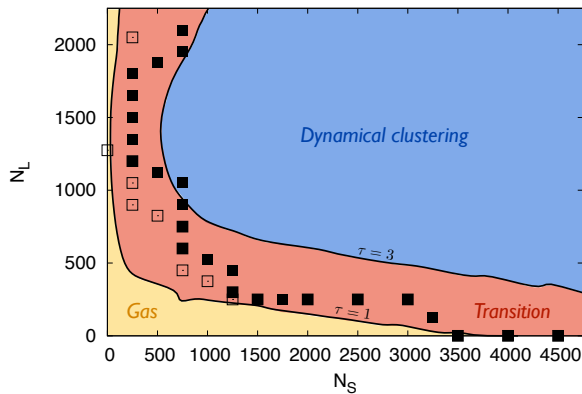
Figure 5. (Colors online) Theoretical phase diagram describing the evolution of the ratio τ using a linear color scale. The curve corresponding to $\tau = 1 - 3$ is in good agreement with our measures concerning the G-CL transition.

6 Conclusion

We investigated numerically the dynamics of a driven binary granular gas within the frame of ESA's SpaceGrains experiment. The respective effects of mass and size differences between both granular species' have been highlighted through molecular dynamics simulations and could be explained by simple energetic arguments. In the case of a mixture of bronze particles, for which both effects are present, a gaseous regime as well as two different clustered states can be encountered. We realized a complex phase diagram as a function of the filling numbers N_S and N_L in which the transitions are detected via statistical uniformity tests of the particle distributions along the vertical axis. For filling parameters corresponding to the central zone, a clustering of mainly large particles can be triggered. This phenomenon leads to a demixing of the granular media and could be used in order to sort out particles in microgravity. Finally, an iterative model based on the balance between the typical times of energy propagation τ_P and energy dissipation τ_H provides a theoretical frontier between gaseous and clustered systems of any kind.

References

1. P. G. de Gennes, Rev. Mod. Phys. **71**, 374 (1999).
2. I. S. Aranson and L. S. Tsmiring, Rev. Mod. Phys. **78**, 641 (2006).
3. J. B. Knight, C. G. Fandrich, Chun Ning Lau, H. M. Jaeger and S. R. Nagel, Phys. Rev. E **51**, 3957 (1995).
4. G. Lumay and N. Vandewalle, Phys. Rev. Lett. **95**, 028002 (2005).
5. F. Ludewig, N. Vandewalle and S. Dorbolo, Gran.Mat. **8**, 87 (2006)
6. F. Vivanco, S. Rica and F. Melo, Gran. Matt. **14** 563 (2012).
7. A. Garcimartín, I. Zuriguel, L. A. Pugnaloni and A. Janda, Phys. Rev. E. **82** 031306 (2010).
8. C. Lozano, G. Lumay, I. Zuriguel, R. C. Hidalgo and A. Garcimartín, Phys. Rev. Lett. **109** 68001 (2012).
9. K. Hutter, K. R. Rajagopal, Continuum Mech. Thermodyn. **6**81 (1994).
10. F. Boyer, E. Guazzelli and O. Pouliquen, Phys. Rev. Lett. **107**, 188301 (2011).
11. I. Goldhirsch, Annu. Rev.Fluid Mech. **35**, 267 (2003).
12. T. Pöschel and N. V. Brilliantov, *Granular gas dynamics*, **624** Springer, (2003).
13. F. Spahn, J. Schmidt and M. Sremcevic, Lect. Notes in Phys. **557**, pp 507-516 (2000).
14. I. Goldhirsch and G. Zanetti, Phys. Rev. Lett. **70**, 1619 (1993).
15. J. S. Olafsen and J. S. Urbach, Phys. Rev. Lett. **81**, 4369 (1998).
16. J. Schockmal, E. Mersch, N. Vandewalle and G. Lumay, Phys. Rev. E. **87**, 062201 (2013).
17. S. Merminod, M. Berhanu and E. Falcon, Europhys. Lett. **106**, 44005 (2014).
18. E. Falcon, S. Fauve and C. Laroche, Eur. Phys. J. B. **9**, 183 (1999).
19. E. Opsomer, F.Ludewig and N. Vandewalle, Phys. Rev. E **84**, 051306 (2011).
20. K. Harth, U. Kornek, T. Trittel, U. Strachauer, S. Höme, K. Will, and R. Stannarius, Phys. Rev. Lett. **110**, 144102 (2013).
21. S. E. Episov and T. Pöschel, J. Stat. Phys. **86**, 1385 (1997).
22. T. P. C. Van Noije and M. H. Ernst, Gran. Matt. **1**, 2 (1998).
23. E. L. Grossman, T. Zhou and E. BenNaim, Phys. Rev. Lett. **55**, 4200 (1997).
24. J. S. Olafsen and J. S. Urbach, Phys. Rev. E. **60**, R2468 (1999).
25. A. Kudrolli and J. Henry, Phys. Rev. E **62**, R1489 (2000).
26. P. Jop, Y. Forterre and O. Pouliquen, Nature **441**, 04801 (1999).
27. J. Eggers, Phys. Rev. Lett. **83**, 5322 (1999).
28. E. Falcon, R. Wunenburger, P. Evesque, S. Fauve, C. Chabot, Y. Garrabos and D. Beysens, Phys. Rev. Lett. **83**, 2, 440 (1999).
29. S. Aumaître, J. Farago, S. Fauve and S. Mc Namara, Eur. Phys. J. B. **42**, 255 (2004).
30. E. Opsomer, F. Ludewig and N. Vandewalle, Europhys. Lett. **99** 40001 (2012).
31. M. E. Möbius, B. E. Lauderdale, S. R. Nagel, and H. M. Jaeger, Nature **414**, 6861 (2001).
32. F. Ludewig, and N. Vandewalle, Eur. Phys. J. E **18**, 4 (2005).
33. A. Kudrolli, Rep. Prog. Phys. **67** 209 (2004).
34. C. Güttler, I. von Borstel, R. Schräpler and J. Blum Phys. Rev. E **87**, 044201 (2013).
35. J. M. Ottino and D. V. Khakhar, Annual Review of Fluid Mechanics **32**, 55 (2000).
36. European Space Agency's SpaceGrains project URL: http://www.spacegrains.org/
37. T. Pöschel and T. Schwager, Computational Granular Dynamics, Springer-Verlag Berlin Heidelberg (2005).

38. S. Luding, Gran. Matt. **10**, 235 (2008).
39. N. Taberlet, PhD Thesis, Université de Rennes I (2005).
40. C. R. K. Windows-Yule, T. Weinhart, D. J. Parker and A. R. Thornton, Phys. Rev. Lett. **112**, 098001 (2014).
41. http://www.planetaryresources.com.
42. National Aeronautics and Space Administration (NASA) mission OSIRIS-REx could help to prepare mining of asteroids, http://www.nasa.gov/content/goddard/new-nasa-mission-to-help-us-learn-how-to-mine-asteroids.
43. C. C. Maaß, N. Insert, G. Maret and C. M. Aegerter, Phys. Rev. Lett. **100**, 248001 (2008).

7.5 Parabolic flight campaign in Bordeaux

First experiments concerning the presented segregation have been realized by Garrabos and coworkers during a parabolic flight campaign of the Centre National d'Études Spatiales (CNES). In their study, particles of two different sizes were enclosed in a rectangular cell as presented in figure 7.4. Another quasi-2d cell was filled with some disks in order to control the g-jitter during the parabola. When the system is driven the large beads gather in the center of the cell exactly as in our simulations [95].
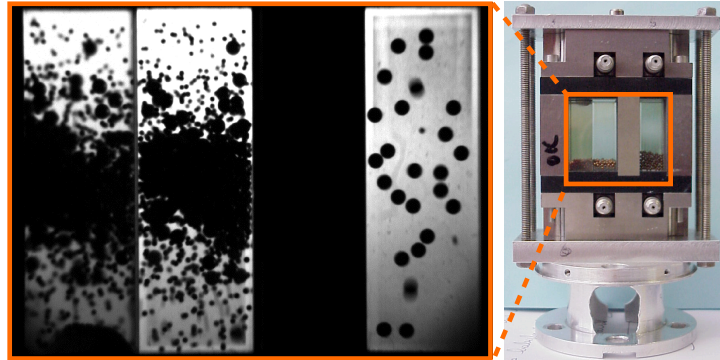

Figure 7.4: (Taken from CNES report by P. Evesque) Snapshots of the experimental cell used for the parabolic flights. Segregation occurs in the bi-disperse system. The right cell is used in order to control the g-jitter.

After a topical team meeting concerning the SpaceGrains project in Noordwijk, we started a collaboration with the group of Garrabos in Bordeaux. A project concerning an experimental adaptation of the setup presented in our article is in preparation and will probably take place in a future parabolic flight campaign of the CNES or ESA.

Chapter 8

Conclusion and perspectives

In this work we studied numerically and theoretically the gathering and the handling of granular materials in microgravity. Our simulations were realized with a home made software based on a molecular dynamics (MD) algorithm and will be used in order to prepare a series of experiments programmed for the SpaceGrains (SG) project of the European Space Agency (ESA).

Our first study concerned the validation of our numerical model. We reproduced the pioneer experiment of Falcon and his coworkers in which a three dimensional dynamical cluster was observed for the first time in microgravity [52]. Excellent qualitative agreement was found between the snapshots of their experiment and the output of our simulations. We then realized additional simulations, based on the same cell geometry but for different filling numbers and grain sizes. In addition to the granular gas and the cluster, two new dynamical regimes were observed. One of them is the partial cluster regime, which corresponds to a phase coexistence of a cluster and a gas. The other one is the bouncing aggregate regime, also called the collect-and-collide regime, which can be seen as a solid phase of the granular media. A granular phase diagram could be realized and a theoretical frontier between the gas and the bouncing aggregate has been proposed. Following the publication of our study [79], the solid regime has been investigated experimentally during parabolic flights [81–83]. The results confirm all of our numerical and theoretical predictions.

The numerical model being validated, we proceeded to predictive simulations concerning the clustering phenomenon in SpaceGrains [92]. We investigated numerically the formation of a cluster within the frame of the SpaceGrains instrument and analyzed the impact of parameters such as the packing fraction, the accessible volume, and the driving amplitude on the phenomenon. We showed that the energy transfer from the pistons towards the center of the cell is the controlling process for the apparition of clustering in the system and developed a theory predicting the transition from a granular gas to a dynamical cluster. The presented model is valid for any rectangular cell geometry since it also successfully predicts the transitions of our first study based on Falcon's experimental cell. From a practical point of view, our study is of great interest for the SpaceGrains project since the acquired theoretical knowledge simplifies the creation of an experimental protocol. Moreover, our theory suggests that the oscillation frequency plays no role in the clustering phenomenon. An intense driving that could transmit vibrations to the space station will thus not be mandatory.

Once the clustering mechanism was rationalized we started to investigate the handling of granular aggregates. A first manipulation consisted in the local trapping of a cluster [93]. Inspired by the work of Dorbolo and his coworkers [65], we designed a particular cell geometry which allows the apparition of Maxwell's demon in microgravity. Our numerical simulations showed that, five different trapping regimes can be encountered depending on the filling fraction of the system. The transition from a granular gas to a single trapped cluster is captured by our theoretical model. An overview of all the different dynamical regimes was given by a bifurcation diagram. Moreover, we proposed an iterative stochastic model reproducing the evolution of the system in a more efficient way than our MD simulations. Finally, we described a theoretical model that gives the asymptotic stable states of the system. Mutli-stable regions were expected but could not be observed given our homogenous initial conditions.

In parallel to the work concerning Maxwell's demon, we investigated the behavior of a cluster which is exposed to an asymmetrical driving [94]. We showed that the cluster's position of equilibrium along the driving axis is fully controlled via the ratio of both driving amplitudes. By placing several cells one to another and connecting them with small apertures it is possible to create ratchet effects in the system and thus to transport granular materials. Moreover, we discussed the natural oscillation of the cluster around its position of equilibrium and could link it to the driving frequency and the cluster's mass. Accordingly, the latter relation provides a non invasive method in order to measure the amount of particles composing the aggregate.

In our last study [95], we investigated the behavior of driven bi-disperse granular gas. The impact of the sizes and the masses of both granular types has been studied independently via numerical simulations. We showed that for mixtures with identical sizes, heavy grains tend to gather in the center of the system while the light ones remain in a gaseous regime near the pistons. For mixtures with identical masses, small particles are more likely to be found in the center of the cell then large ones. Both phenomena seem to correspond to a minimization of the energy. It is interesting to note that in the case of SpaceGrains, where both size and mass are coupled through the density of the particles, size and mass effects are in competition. Indeed, for low fillings the mass effects seem to be dominant and the heavy grains gather the first. However, for higher fillings, contacts between the particles become more frequent and the size effects overtake the mass effects. Accordingly small grains start also to gather and both granular species can be found in the cluster. We realized a phase diagram recovering all the encounters dynamics and proposed an extension of our previous cluster theory to a bi-disperse system. Once again, our simulations were in excellent agreement with the theory.

Table 8.1 gives a brief overview of the different studies that have been realized during my thesis. For each investigated phenomenon, a snapshot of the corresponding cell, a list of the relevant parameters and the main results are given.

<p style="text-align:center">***</p>

In a near future, the breadboard tests of SpaceGrains' prototype will be realized during an ESA parabolic flights campaign. Although these tests are mainly realized in order to check the kinematic chain of the device, some small experiments will be run. Our work can help to prepare this campaign and to set up a list of important parameters to test. Microgravity experiments concerning the segregation will be realized in collaboration with the ICMCB, University of Bordeaux I during a parabolic flight campaign. This study will provide a good way to evaluate the validity of our segregation model and also help to prepare SG. In order to study the impact of the form of the particles on the systems dynamics, the reproduction of drop tower experiments will be realized in collaboration with the group of nonlinear physics from the Otto-von-Guericke University in Magdeburg. In a further future, the SpaceGrains instrument will be sent onto the International SpaceStation (in 2018). In combination with the results from the breadboard testings, our simulation and theoretical predictions will help to prepare the experimental protocol for the project.
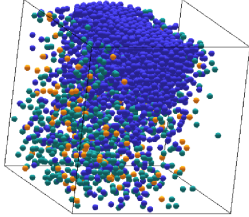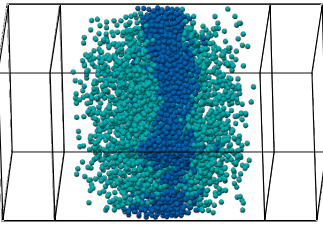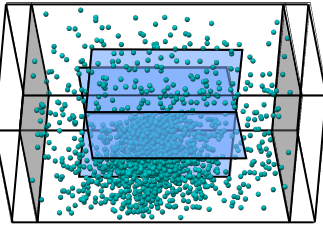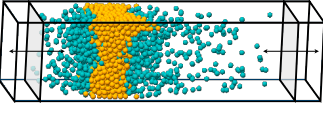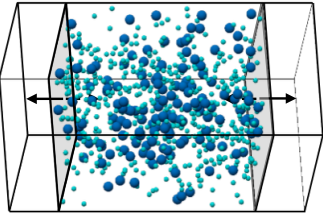
Chapter	3	4	5	6	7
Phenomenon	Clustering	Clustering	Maxwell's demon	Granular transport	Segregation
Cell					
Investigated parameters	ϕ, R, L, A	ϕ, R, L, A	N	A_h, A_c, f	R, ρ, N_L, N_S
Achievements	Transitions from a granular gas up to a bouncing aggregate	Clustering criterion for granular gases	Theoretical and numerical predictions of the asymptotic stationary states	Position and natural oscillations of a cluster	Numerical adaptation of the clustering criterion to bi-disperse systems
Model	$\phi^* = \phi_{rlp}\left(1 - \pi\frac{A}{L}\right)$	$\frac{\delta}{R} > \frac{\xi}{3\phi}\left(\frac{1}{1-3(r_0/R)\phi}\right)$	$\times$	$z_{cl} = \frac{L_g}{2}\left(\frac{1-a}{1+a}\right)$ $\omega_{cl} = \left(\frac{A_c+A_h}{L_g}\right)^{3/2}\left(2\frac{N-N_{cl}}{N_{cl}}\right)$	$\times$

Table 8.1: Summary of the realized studies. For each simulation, the corresponding cell, the relevant parameters for the apparition of the phenomena and the main results are displayed.

Bibliography

[1] J. Duran, *Sables, poudres et grains* Eyrolles Sciences (1999).

[2] P. Coussot, *Rheometry of Pastes, Suspensions, and Granular Materials: Applications in Industry and Environment* John Wiley & Sons (2005).

[3] N. Vandewalle, G. Lumay, F. Ludewig and J. E. Fiscina, Phys. Rev. E. **85**, 031309 (2012).

[4] P. deGennes, Rev. Mod. Phys. **71**, 374 (1999).

[5] H. M. Jaeger and S. R. Nagel, Rev. Mod. Phys. **68**, 4 (1996).

[6] H. M. Jaeger, C. Liu and S. R. Nagel, Phys. Rev. Lett. **62**, 1 (1988).

[7] O. Reynolds, Phil. Mag. Ser. **50**, 20 (1885).

[8] K. Sakaie, D. Fenstein, T. J. Carroll, M. van Hecke and P. Umbanhowar, Europhys. Lett. **84** 38001 (2008)

[9] H. A. Janssen, Z. Vereins Deutsch. Ing. **39**, 1045 (1895).

[10] M. Ammi, D. Bideau and J. P. Troadec, J. Phys. D **20**, 424 (1998).

[11] G. W. Baxter, in *Powders and Grains 97*, edited by R. P. Behringer and J. T. Jenkins (Balkema, Rotterdam, 1997), 345-348.

[12] P. Dantu, in *Proceedings of the 4th International Conference On Soil Mechanics and Foundation Engineering* London, 1957 (Butterworths, London, 1958), Vol. 1, 144-148.

[13] P. Dantu, Ann. Ponts Chauss. **IV**, 193 (1967).

[14] T. Wakabayashi, in *Proceedings of the 9th Japan National Congress for Applied Mechanics*, Tokyo, 1959 (Science Coun- cil of Japan, Tokyo, 1960), 133-140.

[15] T. Travers, M. Ammi, D. Bideau, A. Gervois, J.-C. Messager and J.-P. Troadec, J. Phys. (France) **49**, 939 (1988).

[16] C. Liu, S. R. Nagel, D. A. Schecter, S. N. Coppersmith, S. Majumdar, O. Narayan, and T. A. Witten, Science **269**, 513 (1995).

[17] D. M. Mueth, H. M. Jaeger and S. R. Nagel, Phys. Rev. E. **57**, 3164 (1998).

[18] F. Delyon, D. Dufresne, and Y.-E. Lévy, Ann. Ponts Chauss. **53-54**, 22 (1990).

[19] D. Dufresne, F. Delyon, and Y.-E. Lévy, J. Sci. LPC **2**, 209 (1994).

[20] Y. Zhou, R. D. Wildman and J. M. Huntley, Proc. R. Soc. A. **466**, 2115 (2010).

[21] B. Andreotti, Y. Forterre and O. Pouliquen, *Granular Media: Between Fluid and Solid*, (Cambridge University Press, 2013).

[22] D. Barthès-Biesel, *Microhydrodynamique et fluides complexes*, (Ecole Polytechnique, 2011).

[23] R. G. Larson, *The structure and Rheology of Complex Fluids*, (OUP USA, 1999).

[24] N. Taberlet, P. Richard and E. John Hinch, Phys. Rev. E. **73**, 050301 (R) (2006).

[25] J. B. Knight, H. M. Jaeger and Sidney R. Nagel, Phys. Rev. Lett. **70**, 3728 (1993).

[26] P. Eshuis1, K. van der Weele, D. van der Meer, R. Bos and D. Lohse, Phys. Fluids **19**, 123301 (2007).

[27] F. Rietz and R. Stannarius New J. Phys. **14**, 015001 (2012).

[28] M. G. Clerc, P. Cordero, J. Dunstan. K. Huff. N. Mujica, D. Risso and G. Varas, Nature physics **4** , 3 (2008).

[29] J. Schockmel, E. Mersch, N. Vandewalle and G. Lumay, Phys. Rev. E. **87**, 062201 (2013).

[30] S. Merminod, M. Berhanu and E. Falcon, Europhys. Lett. **106**, 44005 (2014).

[31] I. Goldhirsch, Annu. Rev. Fluid Mech. **35**, 267 (2003).

[32] T. Pöschel and N. V. Brilliantov, *Granular gas dynamics*, **624** (Springer, 2003).

[33] F. Spahn, J. Schmidt and M. Sremcevic, Lect. Notes in Phys. **557**, 507 (2000).

[34] S. Aumaître, J. Farago, S. Fauve and S. Mc Namara, Eur. Phys. J. B. **42**, 255 (2004).

[35] E. Falcon, S. Fauve and C. Laroche, Eur. Phys. J. B **9**, 183 (1999).

[36] S. E. Episov and T. Pöschel, J. Stat. Phys. **86**, 1385 (1997).

[37] T. P. C. Van Noije and M. H. Ernst, Gran. Matt. **1**, 2 (1998).

[38] E. L. Grossman, T. Zhou and E. BenNaim, Phys. Rev. Lett. **55**, 4200 (1997).

[39] J. S. Olafsen and J. S. Urbach, Phys. Rev. E. **60**, R2468 (1999).

[40] A. Kudrolli and J. Henry, Phys. Rev. E **62**, R1489 (2000).

[41] F. Rouyer and N. Menon, Phys. Rev. Lett. **85**, 3676 (2000).

[42] K. Harth, U. Kornek, T. Trittel, U. Strachauer, S. Höme, K. Will, and R. Stannarius, Phys. Rev. Lett. **110**, 144102 (2013).

[43] I. Goldhirsch and G. Zanetti, Phys. Rev. Lett. **70**, 1619 (1993).

[44] S. McNamara and W.R. Young, Phys. Rev. E. **50**, 1 (1994).

[45] N. Brillantov, C. Salueña, T. Schwager and T. Pöschel, Phys. Rev. Lett. **93**, 134301 (2004).

[46] C. C. Maaß, N. Insert, G. Maret and C. M. Aegerter, Phys. Rev. Lett. **100**, 248001 (2008).

[47] P. K. Haff, J. Fluid Mech. **134**, 401 (1983.)

[48] D. Heißelmann, J. Blum, H. J. Fraser, K. Wolling, Icarus **206**, 424 (2010).

[49] R. Brito and M. H. Ernst, Euroohys. Lett. **43**, 497 (1998).

[50] A. Kudrolli, M. Wollpert, J.P. Gollub, Phys. Rev. Lett. **78**, 1383 (1997).

[51] Y. Du, H. Li and L. P. Kadanoff, Phys. Rev. Lett. **74**, 8 (1994).

[52] E. Falcon, R. Wunenburger, P. Evesque, S. Fauve, C. Chabot, Y. Garrabos and D. Beysens, Phys. Rev. Lett. **83**, 440 (1999).

[53] E. Falcon, S. Fauve, C. Laroche, Lecture Notes in Physics, Granular Gases, (Springer, 2000), 182 - 191.

[54] A. Kudrolli, Rep. Prog. Phys. **67**, 209 (2004).

[55] F. Ludewig and N. Vandewalle, Eur. Phys. J. E **18**, 367-372 (2005).

[56] M. E. Möbius, B. E. Lauderdale, S. R. Nagel, and H. M. Jaeger, Nature **414**, 6861 (2001).

[57] C. Güttler, I. von Borstel, R. Schräpler and J. Blum, Phys. Rev. E **87**, 044201 (2013).

[58] J. M. Ottino and D. V. Khakhar, Annu. Rev. Fluid Mech. **32**, 55 (2000).

[59] Y. Oyama, Bull. Inst. Phys. Chem. Res. Rep. **18**, 6001 (1939).

[60] H. Caps, R. Michel, N. Lecocq and N. Vandewalle, Physica A. **326**, 313 (2003).

[61] T. Finger, A.Voigt, J. Stadler, H. G. Niessen, L. Naji and R. Stannarius, Phys. Rev. E. **74**, 031312 (2006).

[62] K.M. Hill, A. Caprihan and J. Kakalios, Phys. Rev. Lett. **78**, 50 (1997).

[63] J. Eggers, Phys. Rev. Lett. **83**, 5322 (1999).

[64] K. van der Weele, Contemporary Physics **49**, 157 (2008).

[65] S. Dorbolo, M. Brandenbourger, F. Damanet, H. Dister, F. Ludewig, D. Terwagne, G. Lumay and N. Vandewalle, Eur. J. Phys. **32**, 1465 (2011).

[66] D. van der Meer, K. van der Weele and D. Lohse, Phys. Rev. E. **63**, 061304 (2001).

[67] D. van der Meer, K. van der Weele, P. Reimann and D. Lohse, J. Stat. Mech. (2007) P07021.

[68] D. van der Meer, K. van der Weele and P. Reimann, Phys. Rev. E. **73**, 061304 (2006).

[69] D. van der Meer, P. Reimann, K. van der Weele and D. Lohse, Phys. Rev. Lett. **92**, 184301 (2004).

[70] N. Insert, C. C. Maaß and C. M. Aegerter, Eur. Phys. J. E **28**, 205 (2009)

[71] P. A. Cundall and O. D. L. Stark, Geotechnique **29**, 47 (1979)

[72] T. Pöschel and T. Schwager, Computational Granular Dynamics, (Springer,Berlin-Heidelberg, 2005).

[73] S. Luding, Gran. Matt. **10**, 235 (2008)

[74] N. Taberlet, PhD Thesis, Université de Rennes I (2005).

[75] H. Hertz, *Gesammelte Werke* Vol. 1, Leipzig, Germany (1895).

[76] C. A. Coulomb, Acam. R. Sci. Mem. Math. Phys. par Divers Savants **7**, 343 (1773).

[77] M. Faraday, Philos. Trans. R. Soc. London **52**, 299 (1831).

[78] M. Jean, Comput. Methods Appl. Mech. Engrg. **177**, 235-257 (1999).

[79] E. Opsomer, F. Ludewig and N. Vandewalle, Phys. Rev. E. **84**, 051306 (2011).

[80] T. Gilet, N. Vandewalle and S. Dorbolo, Phys. Rev. E. **79**, 055201(R) (2009).

[81] M. N. Bannerman, J. E. Kollmer, A. Sack, M. Heckel, P. Mueller and T. Pöschel, Phys. Rev. E. **84**, 011301 (2011).

[82] J. E. Kollmer, A. Sack, M. Heckel and T. Pöschel, New J. of Phys. **15**, 093023 (2013).

[83] A. Sack, M. Heckel, J. E. Kollmer, F. Zimber and T. Pöschel, Phys. Rev. Lett. **111**, 018001 (2013).

[84] W. T. Eadie, D. Drijard, F. E. James, M. Roos and B. Sadoulet, *Statistical Methods in Experimental Physics*, (Amsterdam, 1971), 269-271.

[85] P. Evesque, Poudres et grains **13**, 4 (2002).

[86] E. Opsomer, F. Ludewig and N. Vandewalle, J. Phys.: Conf. Ser. **327**, 012035 (2011).

[87] X. Wang and H. Ma 2010 Chin. J. Chem. Phys. **23**, 675 (2010).

[88] S. F. Edwards, *Granular Matter: An Interdisciplinary Approach*, (Springer, New York, 1994), 121-140.

[89] S. F. Edwards, *Disorder in Condensed Matter Physics* (Oxford Univ. Press, Oxford, 1991), 147-154.

[90] A. Mehta and S. F. Edwards, Physica A **157**, 1091-1097 (1989).

[91] P. Jop, Y. Forterre and O. Pouliquen, Nature **441**, 04801 (1999).

[92] E. Opsomer, F. Ludewig and N. Vandewalle, Europhys. Lett. **99** 40001 (2012).

[93] E. Opsomer, M.Noirhomme, N. Vandewalle and F. Ludewig, Phys. Rev. E. **88**, 012202 (2013).

[94] M. Noirhomme, E. Opsomer, N. Vandewalle and F. Ludewig, Eur. Phys. J. E., submitted (2014).

[95] E. Opsomer, N. Vandewalle, M. Noirhomme and F. Ludewig, Eur. Phys. J. E., accepted (2014).

[96] Planetary Ressources is a start-up company aiming a profit-making mining of near earth asteroids. Available via the URL http://www.planetaryresources.com.

[97] National Aeronautics and Space Administration (NASA) mission OSIRIS-REx . Available via the URL http://www.nasa.gov/content/goddard/new-nasa-mission-to-help-us-learn-how-to-mine-asteroids.